Indian Institute of Technology Guwahati

Optical Imaging Laboratory
Department of Physics
Indian Institute of Technology Guwahati

Development of Optical Sectioning Microscope using Binary Diffraction Hologram

Abhijit Das

Thesis submitted in partial fulfilment of the requirements for the degree of Doctor of Philosophy of the Indian Institute of Technology Guwahati, Guwahati, India.

May 2014

Dedicated To My Beloved Parents

Declaration

Abhijit Das
Roll No. 09612103
Department of Physics
Indian Institute of Technology Guwahati
Guwahati, India

I hereby declare that the results embodied in this thesis is the result of experiments carried out by me at the Department of Physics, Indian Institute of Technology Guwahati, Guwahati, India under the supervision of **Dr. Bosanta R. Boruah**. This thesis has not been submitted to any university/ institute or elsewhere for the award of any degree, diploma or associateship.

Abhijit Das

Date

Certificate

Dr. Bosanta R. Boruah
Associate Professor
Department of Physics
Indian Institute of Technology Guwahati
Guwahati, India
email:brboruah@iitg.ernet.in

This is to certify that the work contained in the thesis entitled **'Development of Optical Sectioning Microscope using Binary Diffraction Hologram'** by **Mr. Abhijit Das** (Roll No. 09612103), a student of Department of Physics, Indian Institute of Technology Guwahati, for the award of degree of Doctor of Philosophy, has been carried out under my supervision.

The present thesis or any part thereof has not been submitted elsewhere for award of any other degree, diploma or associateship.

Bosanta R. Boruah

Date

Acknowledgements

Foremost, I would like to express my sincere gratitude to my thesis supervisor Dr. Bosanta R. Boruah for his continuous support throughout my Ph.D. work and research. Under his guidance I successfully overcame many difficulties and learned a lot. This work would not have been possible without his guidance, support and encouragement. I could not have imagined having a better supervisor and mentor for my Ph.D. work.

Besides my advisor, I would like to thank the rest of my thesis committee: Prof. Alika Khare, Dr. Amarendra Kumar Sarma, Dr. Ranjan Tamuli for their encouragement, insightful comments, and suggestions. I take this opportunity to thank Prof. Alike Khare for providing me the facilities to carry out a part of my research experiments in her laboratory.

My sincere thanks also goes to the former and present HoDs of Physics, Prof. Seenipandian Ravi and Prof. Saurabh Basu for giving me the opportunity to utilize different resources of the department for my Ph.D. work.

Thanks to entire staff of the department of Physics IIT Guwahati, staff of central workshop of IIT Guwahati without whose help my Ph.D. work would have been incomplete.

I thank my friends in the optics group: Abu Mostako, Satchi Kumari, Indrajeet Kumar, Partha Pratim Dey, Poulomi Ghosh, Md. Gaffar, Prahlad Baruah, Rahul Kesarwani, Gyan Prakash Bharti for the stimulating discussions and for the fun that we have during the Ph.D. work. I like to offer sincere thank Biswajit Pathak, Ranjan Kalita for proof-reading many of my thesis chapters. I also like to thank my hostel mates Ruhit Konwar, Himanshu Sonowal, Kuntal Deka for making the moments joyful in the hostel.

I take this opportunity to sincerely acknowledge the financial support from Ministry of Human Resource and Development (MHRD), Government of India during my Ph.D. I express my sincere gratitude to the authorities of Gauhati University for allowing me to carry out my Ph.D. work after my joining in the University. I also like to thank the former and present HoDs of department of Physics, Gauhati University, Prof. Ngangkham Nimai Singh and Prof. Anurup Gohain Barua for the support towards my thesis work. I would like to thank the chairman Hostel Affairs Board, IIT Guwahati for providing me accommodation in the hostel during the final

year of my Ph.D. work.

Last but not the least, I would like to thank my family: my parents Ajit Das and Karuna Das for their support and inspiration throughout my research work. Their infallible love and support has always been my strength. Their patience and sacrifice will remain my inspiration throughout my life. A special thanks to my sister Karabi Das and younger brother Arijit Das for their love and affection. I would like to express my gratitude to my parents-in-law Nikhil Ch. Das and Alaka Das for kind support. Finally, I thank with love to my wife Bonita Das for her understanding, all the support and proof-reading of my thesis chapters.

Abstract

An optical microscope is an imaging instrument that is used to view the features of an object, which can not be seen with an unaided eye, by illuminating the object with visible light. Based on the illumination type, optical microscopes are divided into two broad categories, namely, the widefield microscope and the point scanning microscope. In a widefield microscope the entire target area is illuminated and imaged simultaneously, while, in a point scanning microscope only one object point is illuminated and imaged, and the image of the target area is formed by imaging each object point in a sequential manner. An important member of the point scanning microscopes is the laser scanning confocal microscope (LSCM). Here a laser is focused onto the sample plane using an objective lens to illuminate the object point and the same lens is normally used to collect the light from the sample plane. The light from the sample point is eventually focused on a point photodetector. The point photodetector is kept optically conjugate to the illumination spot on the sample plane. Consequently the photodetector receives light primarily from a volume very close to the centre of the illumination spot. Owing to the unique position of the point detector, the LSCM provides very large axial resolution and moderately large lateral resolution in images, compared to the widefield microscopes. The large axial resolution is also indicated by the capability of the microscope, to separate signals coming from two close by planes in the sample volume which are perpendicular to the optic axis, known as the optical sectioning capability. The LSCM, due to its ability to form optically sectioned images in a non-invasive way, has become an extremely important and essential imaging tool in a large number of application areas.

Realising the importance of the microscope, there have been constant efforts to come up with newer and improved versions of the confocal microscope. However there still exists a number of issues with the conventional LSCM. One such issue is the use of galvo scanner mirror in the LSCM to scan the illumination beam. Such scanners suffer from limited accuracy and frame to frame beam repeatability. Further there is a need to use an additional 4f relay system between the two scanner mirrors. Not only that aligning a 4f relay system is a tedious task, it also adds extra sources of aberrations into the illumination beam. The other issue with a conventional LSCM is the illumination beam whose intensity is kept constant for an entire

image frame. With such a beam, if one images a sample that has both low and high reflectivity/emissivity regions, for an LSCM working in the reflection/fluorescence mode, the image will not have uniform signal to noise ratio (SNR) all over. The portion in the image corresponding to a low reflectivity/emissivity region of the sample will have relatively poor SNR. The third important issue is the phase profile of the illumination beam that remains constant for an entire image frame. With such an illumination beam it may be possible to correct the illumination beam from a fixed set of aberrations that is effective over the entire sample plane. However there are examples, where different positions of the beam over the sample plane may correspond to different sets of aberrations. In such cases to form a perfect image there is a need to estimate and correct the aberrations present in the illumination beam on a pixel to pixel basis.

Thus there are several important, nevertheless, unsolved issues with the LSCM, as far as the imaging performance is concerned. In this thesis work, we attempt to address the above mentioned issues, by developing an optical sectioning microscope. The proposed microscope provides optically sectioned images using a principle similar to that of the confocal microscope. Further it uses an illumination beam whose properties such as amplitude and phase can be controlled dynamically using a computer generated holography technique. In this thesis we present both theoretical/simulation work and experimental results to demonstrate how the above mentioned three issues are addressed in our proposed microscope.

Acronyms

AO	-	Acousto Optics
AOD	-	Acousto Optics Deflector
APSF	-	Amplitude Point Spread Function
BFP	-	Back Focal Plane
BS	-	Beam Splitter
CCD	-	Charged Coupled Device
CGH	-	Computer Generated Holography
CSTM	-	Confocal Scanning Transmission Microscope
DFT	-	Discrete Fourier Transform
FFT	-	Fast Fourier Transform
FLC	-	Ferro-electric Liquid Crystal
ID	-	Iris Diaphragm
IPSF	-	Intensity Point Spread Function
LC	-	Liquid Crystal
LCSLM	-	Liquid Crystal Spatial Light Modulator
LSCM	-	Laser Scanning Confocal Microscope
MO	-	Microscope Objective
NA	-	Numerical Aperture
PBS	-	Polarizing Beam Splitter
PMT	-	Photo Multiplier Tube
PSF	-	Point Spread Function
RI	-	Refractive Index
SLM	-	Spatial Light Modulator
SNR	-	Signal to Noise Ratio

Contents

Declaration **5**

Certificate **7**

Acknowledgements **9**

Abstract **11**

Acronyms **13**

Contents **15**

List of figures **19**

List of tables **25**

1 General introduction **27**

1.1 Introduction 27

1.2 Wide field microscope 28

1.3 Laser scanning confocal microscope 30

1.4 Image formation in a confocal scanning microscope 34

1.5 Components of a confocal microscope 39

1.5.1 The illumination source 39

1.5.2 The objective lens 40

1.5.3 The scanning unit 41

1.5.4 The intermediate optics: the beam splitter 41

1.5.5 The pinhole 41

1.5.6 The detector 42

1.6 Issues with conventional confocal microscopes 42

1.7 Objectives of the thesis work 45
1.8 Conclusion 46

2 Computer generated holography and liquid crystal spatial light modulator 47
2.1 Introduction 47
2.2 Classical holography 48
2.3 Computer generated holography 50
2.3.1 Generation of wavefront with constant amplitude 51
2.3.2 Generation of wavefront with variable intensity in the beam . 53
2.4 Liquid crystal spatial light modulators 56
2.4.1 Nematic liquid crystal spatial light modulators 58
2.4.2 Ferroelectric liquid crystal spatial light modulator 61
2.5 Implementation of binary amplitude or phase hologram using LCSLM 64
2.6 Aliasing effect in binary holograms and minimization of aliasing effect using random binarisation technique 65
2.7 Conclusion 68

3 Beam scanning using binary diffraction holograms 71
3.1 Introduction 71
3.2 A review of the beam scanning mechanisms 71
3.3 Binary hologram based beam scanning using LCSLM 72
3.4 Theoretical considerations 73
3.5 Experimental arrangement 77
3.6 Experimental results 78
3.6.1 Theoretical and experimental beam locations 79
3.6.2 Generation of a regular grid of beam locations 79
3.6.3 Test for beam repeatability 83
3.7 Conclusion 84

4 Optical sectioning microscope with a binary hologram based beam scanning 85
4.1 Introduction 85
4.2 Advantages of the binary hologram based beam scanning microscopes 85
4.3 Optical sectioning microscope using a nematic LCSLM 87
4.3.1 Experimental arrangement 87

4.3.2 Detection mechanism in the microscope . . . 88
4.3.3 Resolution of the microscope . . . 90
4.4 Experimental results and discussion . . . 91
4.4.1 Active aberration correction . . . 91
4.4.2 Optical sectioning performance . . . 91
4.4.3 Imaging performance using reflected light . . . 92
4.5 Optical sectioning microscope with an FLCSLM . . . 94
4.5.1 Synchronization of the detector and the FLCSLM display . . . 94
4.5.2 The experimental arrangement . . . 96
4.5.3 Results and discussion . . . 98
4.6 Conclusion . . . 98

5 Scanning optical microscope with dynamic illumination beam intensity 101
5.1 Introduction . . . 101
5.2 Control over the intensity of the illumination beam using LCSLM . . . 102
5.3 Numerical simulation results . . . 104
5.4 The experimental implementation . . . 105
5.5 Experimental results and discussion . . . 106
5.6 Conclusion . . . 108

6 Scanning optical microscope with dynamic control over the illumination beam phase profile 109
6.1 Introduction . . . 109
6.2 Theoretical considerations . . . 110
6.3 Estimation of aberrations in the illumination beam . . . 112
6.4 The experimental arrangement . . . 113
6.5 Experimental results and discussion . . . 114
6.6 Position dependent aberration correction with a variable intensity illumination beam . . . 115
6.7 Conclusion . . . 117

7 Conclusion and future prospects 119
7.1 Conclusion . . . 119
7.2 Future prospects . . . 122

References **125**

Publications **135**

List of Figures

1.1 A schematic diagram of a conventional wide field microscope. 29
1.2 Two illumination systems of a conventional microscope, (a) critical illumination, and (b) Kohler illumination. 30
1.3 Optical arrangement of various forms of scanning optical microscope. (a) type 1a scanning microscope, (b) type 1b scanning microscope, and (c) the confocal or type 2 scanning microscope. 31
1.4 Schematic diagram of a point scanning microscope. 32
1.5 Working and detection principle of a confocal microscope. 33
1.6 Schematic diagram of a confocal scanning transmission microscope. . 34
1.7 Optical arrangement for image formation with a lens. 35
1.8 Optical arrangement for image formation in a confocal microscope. . 37
1.9 (a) Lateral resolution, and (b) axial resolution comparisons in conventional and confocal microscopes. 39

2.1 (a) Recording of a hologram, and (b) reconstruction of the object beam wavefront. 49
2.2 The experimental setup for generation of the desired wavefront using binary amplitude hologram. The diffraction orders higher than ± 1 order are not shown in the figure. 52
2.3 (a) A binary hologram without added phase, and (b) a binary hologram with added phase. 54
2.4 Line plots of the transmittance corresponding to (a) a binary transmittance hologram with duty cycle=0.5, and (b) a binary transmittance hologram with duty cycle < 0.5. 55
2.5 Plot of the efficiency of the $+1$ diffracted order as a function of duty cycle. 55

2.6 (a) A binary hologram for a plane wavefront object beam with duty cycle < 0.5, and (b) a binary hologram with added phase and having duty cycle < 0.5. 56

2.7 Orientation of the molecules in (a) nematic liquid crystals, and (b) smectic liquid crystals. 57

2.8 Structure of a liquid crystal cell. 58

2.9 Orientation of the molecules in a twisted nematic liquid crystal cell (a) in the absence of external electric field, and (b) in the presence of external electric field $\vec{E}$. 59

2.10 Orientation of the molecules in a reflective nematic liquid crystal cell (a) in the absence of external electric field, and (b) in the presence of external electric field $\vec{E}$. 60

2.11 Molecular orientation in the (a) smectic A, and (b) smectic C phases. (c) Allowed molecular orientations in a cone in the smectic C* phase. 61

2.12 Molecular orientation in a smectic C* phases for the applied electric field (a) $\vec{E}^{+}$, and (b) $\vec{E}^{-}$. 62

2.13 Optical arrangement for the demonstration of amplitude modulation by an FLC cell. 63

2.14 Binary phase modulation by the FLC cell. 64

2.15 (a) A sinusoidal wave with frequency f_c. (b) Sampling of the sinusoidal wave at the rate $f_s = 2f_c$. 66

2.16 (a) A sinusoidal wave with sampling rate $1.5f_c$, and (b) Reconstructed function after sampling at the rate in (a). 66

2.17 (a) A binary hologram described over 128×128 pixels with X tilt 60π and Y tilt 70π. (b) The corresponding diffraction pattern shows that the +3 order appears as the aliased order near the +1 order. 67

2.18 (a) A probabilistically sinusoidal binary hologram described over 128×128 pixels with X tilt 60π and Y tilt 70π. (b) The corresponding diffraction pattern shows that the aliased order has disappeared. . . . 68

3.1 Binary amplitude holograms comprising 32×32 pixels generated using applied slopes= (a)7π, (b) 8π, and (c) 9π along x-axis of the grating and (d) line plots of the holograms along x axis. 74

3.2 Grating comprising N elements denoted by g(1), g(2), ..., g(N) illuminated by a collimated laser beam. w(1), ..., w(N) are the wavefront at the front focal plane of the lens due to each of the corresponding grating elements g(1), g(2), ..., g(N). 75
3.3 The schematic diagram of the experimental arrangement for the measurement of the beam location of the deflected beam. 77
3.4 The plots of the applied slope to the hologram and the theoretically predicted and experimental beam locations. (a) Slope applied along the x axis, and (b) slope applied along the y axis of the hologram. . . 78
3.5 The plot of the theoretical beam locations for the applied slope values along the x axis, between 47π and 58.1π in 555 equal steps. 79
3.6 The plots of the experimental beam locations deflected along the x axis, when (a) the slope values are applied using the map, and (b) equally spaced slope values are applied. 80
3.7 The plots of the experimental beam locations deflected along the y axis, when (a) the slope values are applied using the map, and (b) equally spaced slope values are applied. 80
3.8 The plots of the X coordinates of the experimental beam locations deflected along the diagonal direction, when (a) the slope values are applied using the map, and (b) equally spaced slope values are applied. 82
3.9 The plots of the Y coordinates of the experimental beam locations deflected along the diagonal direction, when (a) the slope values are applied using the map, and (b) equally spaced slope values are applied. 82
3.10 The bar diagrams show the number of times the peak intensity of the deflected beam is found at a particular camera pixel (represented by the horizontal axis), when (a) the beam is scanned along the x axis, and (b) the beam is scanned along the y axis. 83

4.1 The experimental arrangement for the optical sectioning microscope with a nematic LCSLM. 86
4.2 A snapshot of the front panel of the LABVIEW program. 88
4.3 The ray diagram of detection mechanism in a conventional scanning microscope. 89
4.4 The ray diagram of detection mechanism in the proposed microscope. Only the deflection of the illumination beam by the LCSLM is shown. 89

4.5 Synchronized movement of the detector area in the camera plane. (a) The first position of the beam on the camera surrounded by the detector area, and (b) another position of the beam on the camera again surrounded by the detector area. 90

4.6 The illumination beam PSF (a) before aberration correction, and (b) after aberration correction. The scale bar in Fig. (a) has length equal to 97μm. 92

4.7 Plots of normalized detector signals versus mirror displacement measured relative to the focal plane in a direction away from L_5 for a point detector (theoretical) and for detector dimensions DD= 8, 16, 32, and 64 pixels (experimental). 93

4.8 Images using the scattered light from a Fresnel lens using detector dimensions equal to (a) 64, (b) 32, (c) 16, and (d) 8 pixels. The length scale bar in figure (a) has length equal to 566 μm. 93

4.9 Sequential display of the 24 bit planes in an FLCSLM display panel. . 95

4.10 Snapshot of the oscilloscope panel showing the plot of synchronization signal from the FLCSLM (below) and the plot of camera trigger signal (above). 95

4.11 Experimental arrangement for the microscope with an FLCSLM based beam scanning. 96

4.12 An RGB image (800 pixel×800 pixel) comprising 24 binary holograms sending the diffracted beams to equal number of equally spaced locations. 97

4.13 CCD image of 24 focal spots due to the display of a single RGB image in the display panel (top) and a line plot joining centres of the focal spots (bottom). The light intensity is expressed in arbitrary unit (A.U.). 97

4.14 Beam scanning microscope images (size=96 pixel×96 pixels, MO is a 10× Olympus lens of NA=0.3) of a USAF resolution test target, using detector window of dimension equal to (a) 16 pixels, (b) 12 pixels, (c) 8 pixels, and (d) 6 pixels. The dimension of the scale bar at the top left corner in (a) is 78 μm. 98

5.1 Plot of $w(x, y)$ against $i_1(x, y)$ 103

5.2 (a) Image with constant illumination beam intensity, (b) Image with variable illumination beam intensity, and (c) final image of the sample. Horizontal and vertical directions in the image are denoted as X and Y. 104

5.3 Line plots representing Fourier transforms along Y for the images in Fig. 5.2 (a) and Fig. 5.2 (c), considering only (a) high R/T regions, and (b) only low R/T regions. The horizontal axis corresponds to spatial frequency along Y and the vertical axis corresponds to strengths of the spatial frequency components, in arbitrary unit (A.U.), extracted from a normalized Fourier plane. 105

5.4 The experimental setup for the proposed scanning microscope in transmission mode. 106

5.5 Experimentally obtained images (a) i_1, (b) i_2, and (c) the final image of the sample, i_3. 107

5.6 Line plots of the images (a) i_1, i_2 and i_3 along the line shown in Fig. 5.5 (a), and (b) zoomed line plots corresponding to the encircled area in (a). 107

6.1 Schematic diagram of the adaptive optics system without a wavefront sensor. The incoming wave front is indicated by solid lines while the wavefront after correction using the adaptive elements is indicated by the dotted lines. 111

6.2 (a) Aberration corrected PSF of the illumination beam for a given value of m_x and m_y, and (b) aberrated PSF of the illumination beam and shifted horizontally in the camera plane. 113

6.3 The experimental set up of the microscope with pixel to pixel variation in the illumination beam phase profile. 114

6.4 Recorded images of the USAF test target, (a) using the default constant phase profile of the illumination beam, (b) with an illumination beam having different aberration profiles for different locations, and (c) after incorporating position dependent corrections to the aberrated illumination beam. 115

6.5 (a) The corrected image i_1, (b) the image i_2 recorder with the weighted intensity illumination beam, and (c) the final image i_3. Spatial frequency plots along X for the images i_1 and i_3 extracted from the normalised Fourier planes corresponding to the (d) high reflectivity region, and (e) low reflectivity region. The target in the chosen region does not have any spatial variation along X. 116

List of Tables

2.1 Single index Zernike polynomials with index varying from 4 to 11. . . 53

Chapter 1

General introduction

1.1 Introduction

An optical microscope is an imaging system that uses visible light to produce a magnified image of an object or sample. The image thus formed can provide finer details of the target relative to what can be obtained with an unaided eye. The image formed is projected onto the retina of the eye or into an imaging device. It has found applications in diverse areas such as in physical science, biological science, medical science and so on and is common in the related scientific laboratories. In the last few decades new types of optical microscopes have emerged, which have developed the microscope into a powerful instrument to obtain images of sample with sub-micron resolution.

In an optical microscope, the object can be illuminated in two different ways. Depending upon these illumination types optical microscopes are divided into two broad categories, namely, the wide field microscope and the point scanning microscope. In a wide field microscope the desired area of the object is usually illuminated by an extended source, such as a mercury or a xenon source and the entire area is imaged simultaneously. On the other hand, in the point scanning microscope only a small area in the target is illuminated and imaged at a time, requiring it to image the entire area in a point wise fashion.

In this chapter, it is aimed to introduce the conventional wide field microscope and the laser scanning confocal microscope (LSCM), which is a form of point scanning optical sectioning microscope. Since the thesis work is devoted to develop an optical sectioning microscope, more emphasis is given on the LSCM. This is followed

by the description of essential components required for the construction of an LSCM. The theory of image formation in both the wide field and the confocal microscope are then described under paraxial approximations. This is then followed by a discussion on some of the important issues associated with conventional LSCMs and a highlight on the status of present research in the relevant area. The last section of the chapter describes the objective of the thesis which are the proposed ways to address a few of the important issues with conventional LSCM.

1.2 Wide field microscope

In the simplest form, a wide field microscope can comprise just a single lens, with an object whose entire area to be imaged, is illuminated. However to improve the imaging performance of the microscope often one more lens is used. This modified one is known as the compound microscope [1]. Schematic of a compound microscope is shown in Fig. 1.1. In the microscope, the object AB is illuminated by an extended source and the objective lens collects the light coming from the object. The objective lens forms a real inverted image A′B′ of the object at the intermediate image plane of the microscope. Another lens, eye piece, produces a magnified virtual image A″B″ of the object. The final image of the object is formed on the retina of the eye or is projected onto the sensor plane of a camera having an in-built focusing lens. The magnification and the resolution of the images depend upon the lenses used to image the object. Considering the simple lens version of the wide-field microscope, the magnification along the transverse direction is defined as the ratio of the image distance to the object distance, $M_T = \frac{V}{U}$. The longitudinal magnification i.e., magnification along the axial direction of the lens can be written as $M_L = -M_T^2$. The resolution of a microscope is defined as the minimum distance between two points in the object plane that can be resolved in the image plane. The resolution is determined by the numerical aperture (NA) of the lens. Mathematically, it is expressed as $NA = n \sin\theta$, where n is the refractive index (RI) of the focusing medium and θ is the half angle subtended by the lens at its focus. Thus, in another word NA is the measure of the resolution and the light gathering ability of the lens. Numerical aperture also describes the three dimensional light distribution near the focus of a collimated beam or the image of a point object at infinity. This light distribution near the focus is represented by the point spread function (PSF) of the lens. The PSF provides another way to quantify the resolution and imaging

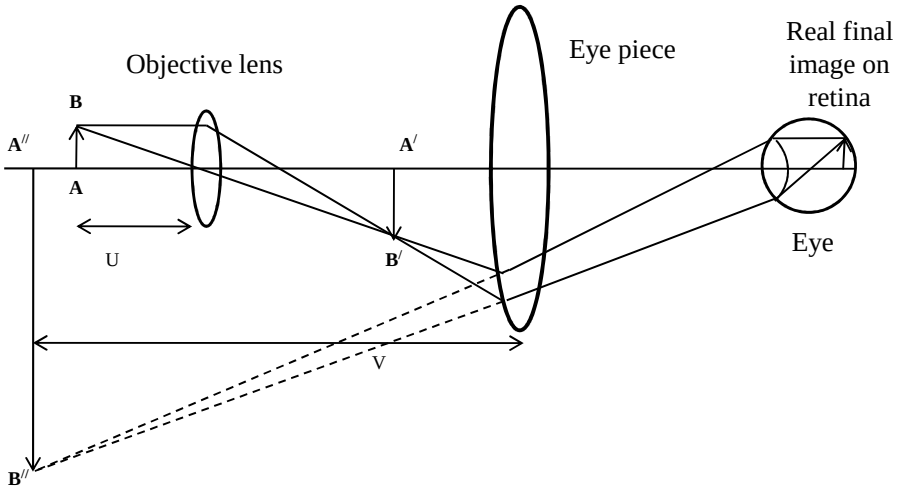

Figure 1.1: A schematic diagram of a conventional wide field microscope.

performance of an optical microscope.

When a point object is placed in the object plane of a lens, it generates a field in the image plane. The spatial variation of the field in the image plane due to the presence of a unit amplitude point object in the object plane is defined as the amplitude point spread function (APSF). While the spatial variation of the intensity in the image plane of the lens due to the same point object in the object plane is termed as the intensity point spread function (IPSF). If the APSF of an imaging system is known then the field in the image plane for the entire object plane can be found by taking the convolution of the APSF with the object plane amplitude. However, the variation of amplitude in the image plane is not observable. The image of an object, which is an observable, is formed by taking the convolution of the object plane intensity with the IPSF of the system.

For illuminating the object in a wide field microscope two different types of illumination systems can be employed, namely, the critical illumination system and the Kohler illumination system. In the critical illumination system, usually light from an incoherent source such as filament lamp is used to illuminate the sample through a condenser lens and its NA is controlled by an aperture stop. The image of the filament lamp is focused on the sample plane using the condenser lens, as seen in Fig. 1.2 (a). However, there is a disadvantage of critical illumination, as the filament lamp is imaged onto the sample plane, the illumination may be highly nonuniform. To overcome this problem of illumination, August Kohler in 1893 designed a new method and this illumination system is most commonly used for illuminating the

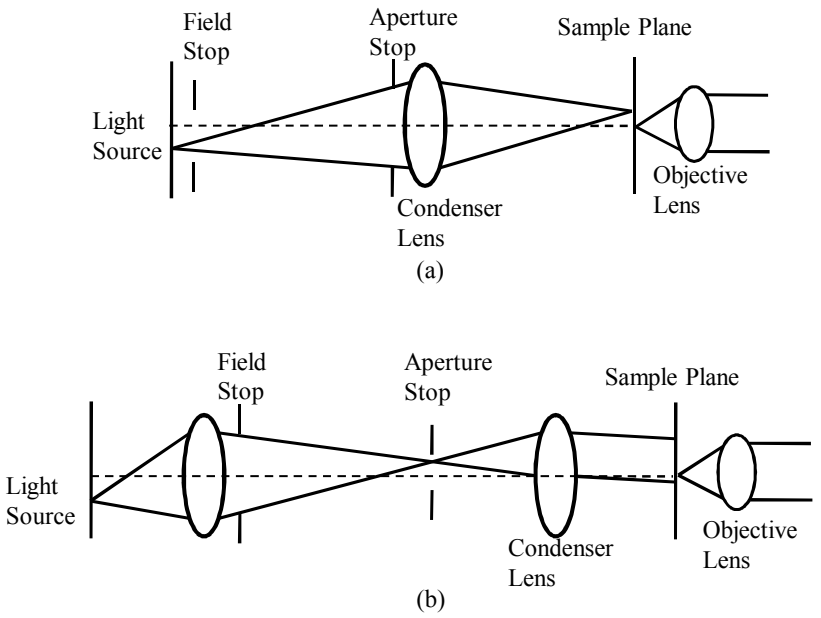

Figure 1.2: Two illumination systems of a conventional microscope, (a) critical illumination, and (b) Kohler illumination.

sample in wide field microscopes. In this illumination system the light source is imaged on the back focal plane of the condenser lens, as shown in Fig. 1.2 (b). The sample is illuminated by the defocused image of the light source and this illuminates the sample more uniformly compared to the critical illumination system. Although wide field microscope can produce image with resolution of the order of half of wavelength, the light coming from the object points away from the sample plane contributes to unwanted background effect, leading to a loss in image contrast. A laser scanning confocal microscope, a form of point scanning microscope can resolve this issue by blocking the light reaching the image plane from planes other than the sample plane.

1.3 Laser scanning confocal microscope

A point scanning microscope can be constructed from a conventional wide field microscope by scanning a point detector through the image plane to measure the image intensity for the entire object as shown in Fig. 1.3 (a). The signal from the point detector is stored in a computer and at the end of the scanning, the final image is constructed using the stored data [2]. T. Wilson named such a scanning microscope as type 1*a* scanning microscope [3]. Another version of the scanning

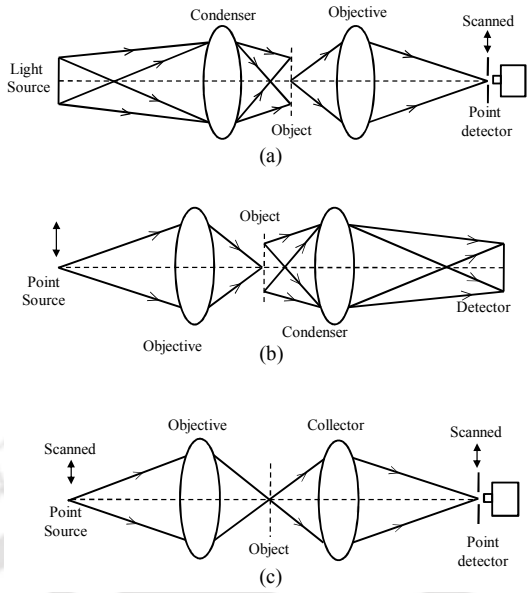

Figure 1.3: Optical arrangement of various forms of scanning optical microscope. (a) type 1*a* scanning microscope, (b) type 1*b* scanning microscope, and (c) the confocal or type 2 scanning microscope.

microscope, called type 1*b*, can be obtained by replacing the extended source with a point source and the point detector with a large area incoherent detector as shown in Fig. 1.3 (b). Here, the first lens acts as the objective lens and the object plane is illuminated by the focused light spot in a point wise fashion. The second lens plays the role of collector and collects the light transmitted through the object. The collector lens is analogous to the condenser lens in a conventional microscope and plays only a minor role in determining the resolution. The role of the second lens can be made significant in determining the resolution of the microscope by making it as the imaging lens instead of collector lens. This can be achieved by replacing the large area detector by a point detector as shown in Fig. 1.3 (c). Here the point source and the point detector are so arranged that only the light from the centre of the illumination spot is detected. This arrangement of the microscope was named as the type 2 or confocal scanning microscope [3]. In this symmetric confocal arrangement it is seen that both the lenses play equal roles in determining the image resolution. Here the two lenses are arranged to image a single object point at a time, leading to an improvement in resolution. To get the image of the complete object, the object can also be scanned with respect to the illumination beam. However, instead of scanning the object, scanning the illumination spot or the illumination beam is found to be advantageous in many applications. This form of the point scanning

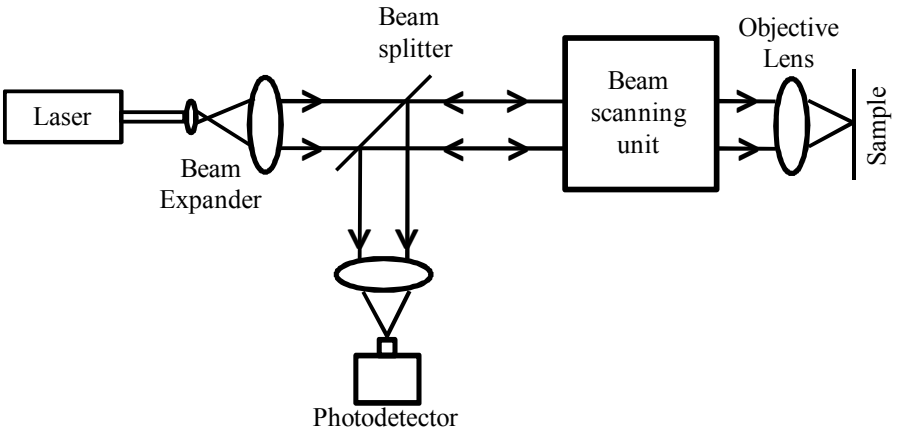

Figure 1.4: Schematic diagram of a point scanning microscope.

microscope is the popular form of a laser scanning confocal microscope (LSCM). It can form images with significantly higher axial resolution relative to a wide field microscope. Consequently, LSCM now has become an essential tool for non-invasive imaging in diverse areas. In the present work, we will consider an equivalent form of such a point scanning microscope.

The confocal system shown in Fig. 1.3 (c) works in transmission mode and such a microscope is also known as confocal scanning transmission microscope (CSTM) [4]. However, confocal microscope can also be arranged in the reflection mode. Figure 1.4 shows a basic set up of a confocal microscope with a beam scanning unit working in the reflection mode. Here, the beam from a laser source is collimated and focused on the sample plane to a diffraction limited spot using a microscope objective [2, 3]. This focal spot acting as the illumination spot, is scanned over the sample plane using a beam scanner unit such that the spot on the sample plane describes a rectangular area. The reflected light from each object point is again collected by the same objective lens and is then descanned by the scanner unit. The light is finally focused on a point detector (which can be finite area detector with a pinhole placed in front of the detector area), using a lens. The point detector is placed optically conjugate to the illumination spot. During the scanning, the detector collects the signal for each position of the beam on the sample plane and are stored in a personal computer (PC). The signal collected by the detector for each position is the representation of the sample surface profile and reflectivity. At the end of the scanning the collected signal is converted into a digital image. Arrangement of the pinhole provides optical sectioning capability to the imaging system. The optical sectioning

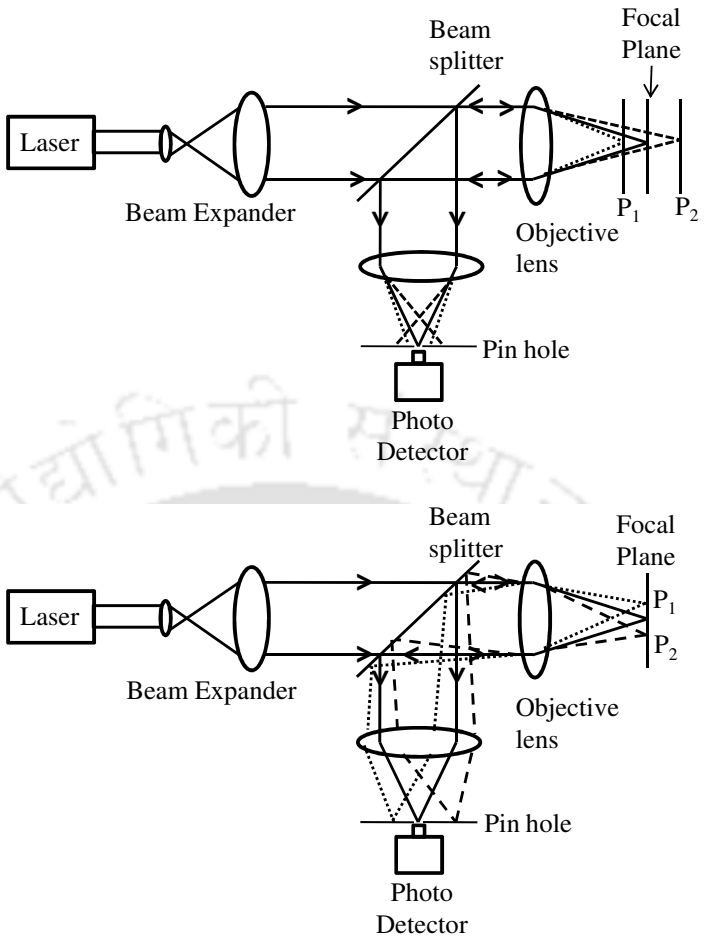

Figure 1.5: Working and detection principle of a confocal microscope.

property of an imaging system is the ability to differentiate between two close by planes which are perpendicular to the optic axis (defined as the axis of cylindrical symmerty of the lens of a given lens or a imaging system). Due to the position of the pinhole, the detector receives light predominantly from the sample plane only. The rejection of the out of focus signals can be understood from Fig. 1.5. Light from the off axis or out of focus points such P_1 or P_2 are mostly blocked by the pinhole, thus allowing light coming from around the illumination spot only, such that the microscope can form optically sectioned images. The optical sectioning ability of a microscope depends upon the NA of the objective lens, detector lens and the size of pinhole in front of the photodetector. As the size of the pinhole gets smaller, the light coming away from the focal spot is mostly blocked and the detector receives the light only from the points very close to the focal spot. The confocal system therefore can improve both the axial as well as the lateral resolution of the image of

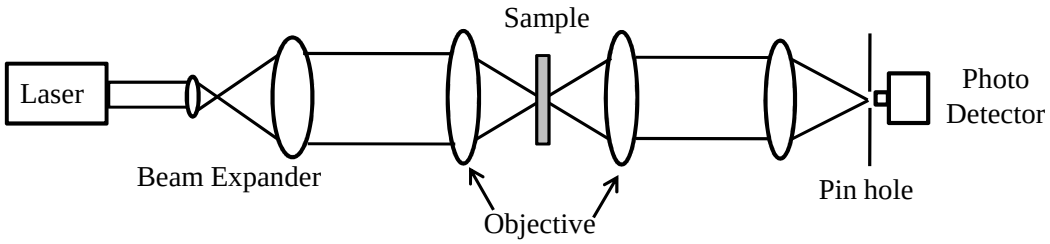

Figure 1.6: Schematic diagram of a confocal scanning transmission microscope.

a specimen beyond what is achievable with a wide field microscope. This provides the much needed facility for obtaining image stacks having depth information of the sample volume.

Schematic of a more practical version of a confocal transmission microscope is shown in Fig. 1.6. It can be constructed by placing two objective lenses on each side of a semi transparent sample. The light after being transmitted through the sample plane is collimated by the second objective lens and is then focused on a detector through a pinhole. The LSCM in transmission mode is particularly suitable for weakly reflecting biological materials. However, due to the use of two two objective lenses, it is difficult to keep the two lenses at optimum distances as the focused beam has to pass through a transparent sample having a refractive index different from the surrounding. Later Sheppard and Wilson attempted to make transmission LSCM (or CSTM) compatible with the reflection LSCM. They developed a CSTM where the transmitted light from the sample is collected by a second lens and then reflected by a plane mirror such that light again passes through the same sample point [5]. As the beam passes through the sample twice, aberration caused by the sample worsens the imaging performance as compared to the single pass system. Due to such limitations, in various applications the confocal microscope in the reflection mode is more preferred relative the same in the transmission mode.

1.4 Image formation in a confocal scanning microscope

The formation of image in a confocal scanning microscope can be understood using the Fourier optics theory. To understand the mechanism behind image formation

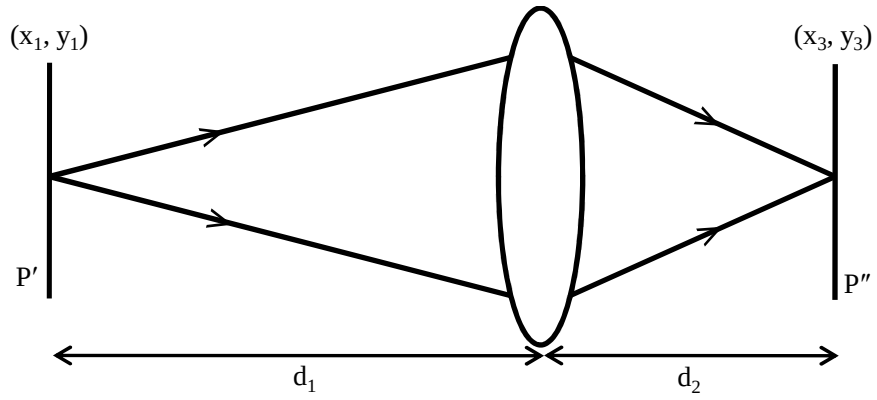

Figure 1.7: Optical arrangement for image formation with a lens.

we consider a simple optical system where the image is formed by a single lens as shown in Fig. 1.7. The theoretical expressions obtained here are valid under paraxial approximation. Here plane P' is the object plane where the field is denoted by $A(x_1, y_1)$, with (x_1, y_1) as the coordinates in the object plane. The field in the image plane P'' [6, 7] due to the field in the object plane can be written as

$$A(x_3, y_3) = \int A(x_1, y_1) h(x_1 + x_3/M, y_1 + y_3/M) dx_1 dy_1 \tag{1.1}$$

where $M = d_2/d_1$ is the magnification, (x_3, y_3) are coordinates of the image plane, and h is the amplitude point spread function which is expressed as [6]

$$h(x, y) = \int \int P(x_2, y_2) \exp\left[\frac{2i\pi}{\lambda d_1}(x_2 x + y_2 y)\right] dx_2 dy_2 \tag{1.2}$$

Here P is the pupil function of the lens describing the field in the entrance pupil of the lens due to a unit amplitude point source kept at infinity and (x_2, y_2) are the co-ordinates in the pupil plane. Now taking the simplest case where the object is just a point source, its amplitude can be represented as

$$A(x_1, y_1) = \delta(x_1, y_1) \tag{1.3}$$

where δ(x,y) represents the Dirac delta function in two dimensions. When the illumination is coherent, the amplitude in the image plane is given by

$$A(x_3, y_3) = \Big[h(x_3/M, y_3/M)\Big] \otimes \Big[A(x_1, y_1)\Big] \tag{1.4}$$

where $\otimes$ is the convolution operator. The intensity in the image plane is given by the modulus square of the amplitude in the image plane and can be expressed as

$$I_c(x_3, y_3) = |A(x_3, y_3)|^2 \tag{1.5}$$

However, when the illumination is incoherent in nature, the intensity in the image plane is found by taking the product of the IPSF and intensity of the object and is given by

$$I_{inc}(x_3, y_3) = \left|h(x_3/M, y_3/M)\right|^2 \otimes \left|A(x_1, y_1)\right|^2 \tag{1.6}$$

In practice the object is not a point but superposition of many such point objects. Therefore, this expression can be extended to find the intensity distribution in the image plane for an extended object. For a lens of radius a, the pupil function P(ρ) is expressed as

$$P(\rho) = \begin{cases} 1 & \text{if } \rho < 1 \\ 0 & \text{if } \rho \geq 1 \end{cases} \tag{1.7}$$

where

$$\rho = \frac{r_2}{a} \tag{1.8}$$

and $r_2 = \sqrt{x_2^2 + y_2^2}$. The intensity distribution of a point object thus can be written as [6, 8]

$$I(v) = |2\int_0^1 P(\rho) J_0(v\rho)\rho d\rho|^2 \tag{1.9}$$

where J_0 is the Bessel function of zero order and first kind and v is the normalized optical coordinate expressed in terms of the radial coordinate of the plane P'' written as

$$v = \frac{2\pi}{\lambda} r_3 \sin\alpha \tag{1.10}$$

where $\sin\alpha$ is the NA of the lens. From equation 1.9 it is clear that the intensity distribution in the image plane depends on the pupil function $P(\rho)$. For a lens as mentioned above (i.e. a circular pupil with unit transmittance amplitude) the intensity in the image plane can be written as

$$I(v) = \left(\frac{2J_1(v)}{v}\right)^2 \tag{1.11}$$

where J_1 is the Bessel function of the first order and first kind.

To find the resolution of the imaging system we employ Rayleigh criterion, which

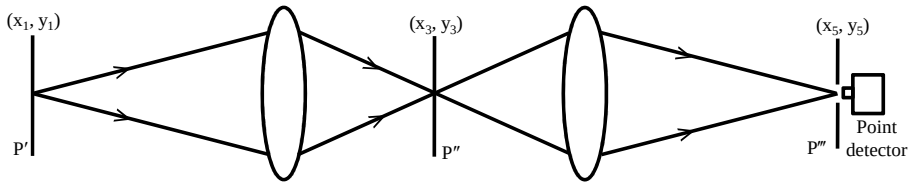

Figure 1.8: Optical arrangement for image formation in a confocal microscope.

states that two closely spaced point objects are just resolved if the maximum response due to one point is located at the zero response due to the other point. Applying this condition in equation 1.11, the resolution limit of an imaging system is found to be [9]

$$r_w = \frac{0.61\lambda}{NA} \tag{1.12}$$

From the expression it can be seen that resolution limit of the order of $\lambda/2$ can be obtained with a wide field microscope.

Along the optic axis the intensity distribution in the image volume is expressed as [10]

$$I(u) = \left(\frac{\sin(u/4)}{u/4}\right)^2 \tag{1.13}$$

where $u = \frac{2\pi(NA)^2 z}{n\lambda}$ is the normalized optical coordinate corresponding to the axial position z, and n is the refractive index of the focusing medium [11]. This expression can be utilized to find the resolution along the optic axis, which under paraxial approximation is found to be [12]

$$z_w = \frac{2n\lambda}{(NA)^2} \tag{1.14}$$

The above expressions can be extended for the case of a scanning confocal microscope where two lenses, namely the objective lens and the collector lens contribute equally in the formation of an image. The image formation optical system for a scanning confocal microscope is shown in Fig. 1.8. It can be shown that the effective PSF is the product of the two PSFs due to the two lenses. Therefore, if h_1 and h_2 are the PSFs for the two lenses, then effective PSF of the confocal system is [3]

$$h_{eff} = h_1 h_2 \tag{1.15}$$

The amplitude in the image plane (x_5, y_5) due to an object with amplitude trans-

mittance t in the object plane (x_1, y_1) can be written using the equations 1.4 and 1.15

$$A(x_5, y_5) = |h_1 h_2 \otimes t| \tag{1.16}$$

Therefore, the intensity distribution at the image plane can be written as

$$I(x_5, y_5) = |h_1 h_2 \otimes t|^2 \tag{1.17}$$

If the two lenses are similar i.e., having equal radius and NA, then $h_1 = h_2 = h$, the intensity distribution in the image plane can be simply written as

$$I(v) = \left(\frac{2J_1(v)}{v}\right)^4 \tag{1.18}$$

The resolution or the minimum resolvable distance r_c between two point objects in the transverse direction is found to be

$$r_c = \frac{0.4\lambda}{NA} \tag{1.19}$$

Similarly the variation of the intensity in the image volume along the optic axis, due to a point object is given by [10]

$$I(u) = \left(\frac{\sin(u/4)}{u/4}\right)^4 \tag{1.20}$$

The resolution along the optic axis for confocal scanning microscope is thus expressed as

$$z_c = \frac{1.44n\lambda}{NA^2} \tag{1.21}$$

The normalized intensity distributions in the image plane due to a point object in the case of a wide field microscope and a scanning confocal microscope are shown in Fig. 1.9 (a). From the plot it is seen that full width at half maxima for scanning confocal microscope is around 30% narrower than that of a wide field microscope. The variations of the intensity in the image volume along the optic axis for the conventional and the confocal case are shown in Fig. 1.9 (b). From the above discussion it is seen that in the case of scanning confocal microscope, the resolutions along the transverse and the optic axis are enhanced relative to a wide field microscope.

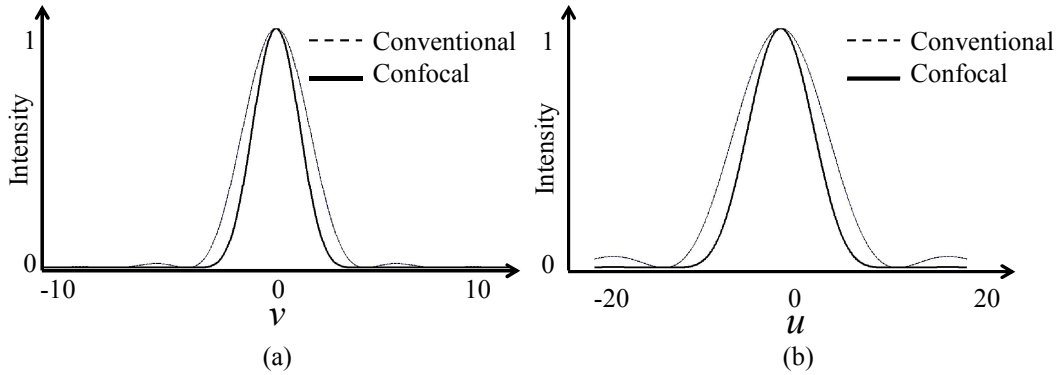

Figure 1.9: (a) Lateral resolution, and (b) axial resolution comparisons in conventional and confocal microscopes.

1.5 Components of a confocal microscope

The basic building blocks of a confocal system comprise the illumination source, the beam delivering optics including the beam expander and the microscope objective, the point detector and the beam scanning unit. In some confocal system instead of a beam scanning unit a sample stage scanning unit is used. Below we provide a brief discussion on these building blocks.

1.5.1 The illumination source

For a confocal microscope, a stable source of spatially coherent light that is capable of forming a tiny illumination spot is required. Lasers, due to their unique properties such as directionality, coherence, monochromaticity and brightness, are the best candidate to serve as the illumination source. For choosing lasers to use in a confocal scanning microscope, its mode structure, power stability, and spectral bandwidth should be evaluated. Generally, TEM_{00} mode output from a laser is preferred [9], as they have a circularly symmetric cross section. Therefore, when they are focused by a lens, a focal spot having circularly symmetric intensity can be found at the focus of the lens. The other criteria of the source to be used is the power stability. Unstable output from the source will eventually lead to wrong detector signals. On the other hand, a spread in spectral bandwidth will contribute to an elongation of the illumination spot, which will effect the optical sectioning ability.

There are various types of lasers that are used in a LSCM. He-Ne gas laser is a good choice as the illumination source since they are inexpensive, available in variety

of wavelengths and have a narrow spectral width. In many applications, diode lasers are used as the illumination source, as they are inexpensive, stable, and available in a number of wavelengths. In some applications instead of a laser, broadband light source like mercury or xenon lamp is preferred as the illumination source. For instance in some material science applications, broadband sources are preferred [13]. Arc lamps are also used in confocal systems as a illumination source because of their advantages like compactness, efficiency and larger bandwidth compared to other light sources. Due to the large spectral bandwidth, the axial chromatic aberration in the optical system will lead to focusing of light in different planes. Thus, it is useful in the inspection applications where areas of the sample at different axial positions are differentiated in terms of different colors [14].

1.5.2 The objective lens

The most important and the essential component of an LSCM is the objective lens. The objective lens is normally used to illuminate as well as to receive light from the sample plane. It is responsible for primary image formation and thus the quality of images formed. Suitable lens selection is the key to achieve optimum performance by an LSCM. Since the light travels twice through the same lens, lens aberration is crucial in confocal imaging system. Therefore, it is important to keep the aberration in the lens system minimum. In LSCM the common aberration that effects the imaging performance is the spherical aberration [15].

Major microscope manufacturers design a wide range of objective lens that can provide various degrees of correction for the primary aberrations. Modern objectives are designed with the assistance of computer aided design system and has reached a high state of quality and performance. With the advanced techniques the manufacturers are able to produce objectives that are corrected for most of the common monochromatic aberrations such as coma, astigmatism, distortion, field curvature, spherical aberration and also for chromatic aberration. In majority of the laboratories the objectives used are achromatic objectives due their low cost. Achromatic objectives are corrected for axial chromatic aberration for two colors blue and red and corrected for spherical aberration for green color. Fluorites or semi-apochromats are the objectives having next higher level corrections for aberration such as additional correction for spherical aberration at another wavelength. Apochromats are the most highly corrected objectives available.

1.5.3 The scanning unit

In most of the commercially available LSCMs, the mechanism of beam scanning is preferred over the mechanism of stage scanning, because of several advantages such as scanning speed of the beam scanner, static state of the sample etc. For scanning the laser beam in an LSCM, commonly galvanometer mirror scanners are used [16, 17]. In few other systems acousto-optics (AO)deflector [18], and a rotating polygon mirror scanner [19] are also used for beam scanning. The beam scanning with galvanometer mirrors is, to a certain extent, independent of the wavelength of light used. This provides the facility to use the scanner even with white light and in fluorescent imaging. On the other, hand the beam scanning with AO is wavelength dependent and the amount of beam deflection is proportional to the optical wavelength and frequency of the driving signal. Nevertheless, AO scanners have the advantage that provide fast scanning facility since the driving frequency is electronically controlled [20, 21].

1.5.4 The intermediate optics: the beam splitter

The light that is emitted or reflected from the sample plane travels back through the objective lens towards the detector plane. This is achieved with the help of a beam splitter that is placed in the path of the beam so that light is reflected normal to the beam path. For imaging using reflected light from the sample a 50/50 non-polarizing beam splitter is used. For the applications in the fluorescence mode, instead of a 50/50 beam splitter a dichroic beam splitter is used. A dichroic beam splitter transmits longer wavelength and reflects shorter wavelength.

1.5.5 The pinhole

The pinhole kept in front of the photodetector in an LSCM plays an important role in determining the resolution in both transverse and axial directions. The required size of the pinhole depends on the reflectivity of the sample and the desired resolution. If the pinhole is large, it will transmit more light to the detector and generate image with large signal to noise ratio (SNR), which is defined as the ratio of the signal to the noise, at the cost of resolution. On the other hand, a small pinhole will give better resolution although the SNR will be low. Therefore, it is very important to optimize the pinhole size depending on the applications. In practice, pinhole size

should be equal to the full width at half maxima of the Airy pattern, produced by the focusing lens in front of the pinhole, which can give the optimum resolution and SNR [22].

1.5.6 The detector

After passing through the pinhole the light hits the detector which converts the light into an electrical signal. The electrical signal thus generated is proportional to the amount of light falling on the detector. The nature of the detector used in a confocal microscope depends on the amount of light reflected or transmitted from the sample. If the number of photons reaching the photodetector are fewer than 10^8 photons/s, a photomultiplier tube (PMT) in photon-counting mode is the suitable [2]. Modern microscopes use PMTs that convert anode current into a voltage and use this voltage as a measure of the incident light. The SNR can be maximized for PMTs by using the optimal setting for the acceleration voltage. A cooled charged coupled devices (CCD) camera can also serve the purpose for detecting the photons. A CCD camera has large dynamic range and an extraordinary high quantum efficiency. However it generates a noise equivalent to the photoelectron signal. The generation of noise is due to thermal generation during integration time. This noise can be reduced for some CCD chips with slow scan readout.

The electrical signal produced by the photodetector is sent to PC that also controls the beam scanner. Thus the detector signal stored in the PC can be linked with the respective X and Y positions of the beam in the sample plane in order to generate an electronic image at the end of the scanning.

1.6 Issues with conventional confocal microscopes

Owing to its capability of providing optically sectioned images in a non-invasive way, the laser scanning confocal microscope has become an essential imaging tool in diverse application areas. Consequently research groups in the relevant area all over the world have been putting a constant effort to come up with new designs that can improve the imaging performance of the confocal system. However there are certain issues with a conventional confocal system which are yet not adequately addressed.

One of the important issues associated with the confocal microscope is the beam scanning mechanism. Galvanometer based two mirror scanners constitute the com-

mon scanning mechanism in a confocal system. The two mirrors are positioned to provide beam deflections in orthogonal directions. To avoid the lateral displacement of the illumination beam on the back focal plane (BFP) of the objective lens during scanning, a 4f relay system is used between the two mirrors and another 4f relay system is placed between the second mirror and the microscope objective. Thus, there is a requirement of an additional 4f relay system between the two mirror scanners. Perfect alignment of a 4f relay system is always a tedious task. There is a possibility of incorporating aberrations into the illumination beam due to imperfect optics and alignment associated with the relay system. Mirror based relay systems have been used instead of lens based relay systems to reduce the amount of aberrations added to the illumination beam by lens based relay system [23, 24]. However, it still needs to be aligned properly. To avoid the use of extra relay system, Zeiss confocal microscope uses two scanner mirrors that are placed very close to one another. In such case there is a small amount of lateral movement of the illumination beam in the BFP of the objective lens [2]. Moreover, the galvanometer based beam scanner has limited accuracy in positioning the beam and has limited repeatability. Due to the limited beam accuracy, the beam has limited frame to frame stability. The short term repeatability of the scanner can be of the order of 10 microradian. This accuracy of the scanner is acceptable for small to medium exposure imaging. On the other hand, the long term thermal drift over few hours can be of the order of 0.5 milliradian and this becomes an important issue for long exposure imaging, such as the collection of the fluorescence light from the sample to observe physical processes for hours [25], detecting Raman signals from the sample [26, 27], monitoring slow chemical processes [28] etc. The beam repeatability and the beam positioning accuracy can become an issue even in the short exposure imaging applications using long working distance objective lenses [29, 30].

In a conventional laser scanning confocal microscope the intensity of the illumination beam is kept fixed during an entire image frame. This works fine as long as the specimen being imaged comprises object points having comparable reflectivity or emissivity. However there are applications where reflectivity or emissivity may not be of comparable magnitude throughout. For example there are biological and material samples where the reflectivity or the transmissivity (referred as R/T) vary from region to region [9]. When such samples are imaged in an LSCM with constant illumination beam intensity working in the reflection/transmission mode, the image formed has low signal to noise ratio in the low R/T region compared to the high

R/T region. According to David R. Sandison only 0.02% of the emitted photons are detected in conventional confocal microscopy [2]. Thus in some cases the signal level detected becomes comparable to the noise level [31]. The low signal to noise ratio wreck the imaging performance of the imaging system and the recorded image may lose the information in the region of low R/T [32]. The signal from the low R/T region can be enhanced by increasing the intensity of the illumination beam. However, as a consequence, the signal from the high R/T region will also rise. Thus in an attempt to increase the signal level from low R/T regions, the signal from higher R/T may saturate the detector leading to loss of information in the corresponding regions. A few techniques have been proposed to improve the signal to noise ratio in a scanning confocal microscope. T. D. Milster et. al designed a scanning optical microscope that incorporates a filter placed in the return path of the optical system, in order to improve signal to noise ratio [33]. A 4Pi-microscope provides not only better axial resolution and enhanced transverse resolution, owing to the polarization effect [34], but also better image contrast [35, 36]. The enhancement in the contrast is mainly due to the increase of the detected signal levels achieved by symmetric arrangement of two objective lenses. However, in all such techniques the signals from all the regions of the sample increase. As a result, signal received from the higher R/T region may still saturate the detector.

The resolution and the contrast of the image formed in an imaging system, depends on the intensity distribution of the illumination spot i.e., on the IPSF. The imaging system can provide the best image of the sample if the IPSF on the sample plane is an Airy pattern (in the low NA case). To achieve such a situation, the illumination beam on the BFP of the objective lens should have a plane wavefront, assuming that the objective lens is more or less aberration free. However, this condition is not always achieved due to the imperfect optics in the beam path and the aberration originated in the source itself. Thus the wavefront may deviate from the desired plane wavefront at the BFP of objective lens. Such a deviation is known as the aberration in the illumination beam. The presence of aberration in the beam broadens the IPSF and reduces the peak intensity. This affects the imaging performance of the system. Some advanced LSCM may have the facility to correct the beam from aberrations which are static for an entire image frame. However, a problem arises when the aberration added to the illumination beam varies from region to region over the sample plane. For example when imaging deep inside a biological tissue, the wavefront deviates from the desired shape and

varies from region to region. This is mainly due to the inhomogeneous nature of the sample, and refractive index (RI) mismatch between the sample and the surroundings [37, 38, 39, 40]. Moreover, the sample may have a spatially varying RI profile, which can introduce a spatially varying aberration into the illumination beam. The spherical aberration is found to be the major aberration present, when the beam is in a RI mismatch region [39]. The amount of aberrations present in the illumination beam can be measured by employing a wavefront sensor [41, 42, 43, 44] and the resulting aberrations can be used to compensate for the said aberrations. Such a technique is called adaptive optics. However, the adaptive optics systems used in confocal microscopy are primarily to correct the beam for an arbitrary aberration profile which is fixed for an entire sample plane. The adaptive optics technique has also been developed to correct the illumination beam without the use of a distinct wavefront sensor [37, 45]. There are attempts to implement scanning microscopes where the illumination beam can be corrected dynamically during the imaging; however, there is still not sufficient work reported in the available literature regarding realisation of an LSCM that has aberration correction mechanism on a pixel to pixel basis.

1.7 Objectives of the thesis work

It has emerged from the previous section that there still exist several issues with laser scanning confocal systems which have not been adequately addressed. Although there may be additional issues associated with the confocal systems, in this thesis, it is decided to focus on the three issues mentioned above. We propose to develop a beam scanning microscope that provides optical sectioning using the principle of the confocal microscope. We employ a computer generated holography (CGH) technique [46, 47] to configure the illumination beam in order to address the three issues.

The objective of the present thesis work is stated below.

- To develop a scanning mechanism that does not require the additional 4f relay system and provides superior beam positioning and beam repeatability.

- To develop an optical sectioning microscope using the above mentioned scanning mechanism.

- To extend the optical sectioning microscope mentioned above to provide images with superior signal to noise ratio for samples having both low and high R/T region.

- To incorporate pixel to pixel aberration correction option in the illumination beam of the above system for samples that introduce spatially varying aberration into the illumination beam.

1.8 Conclusion

In this chapter we have described optical microscopy by dividing microscopes into two broad categories, namely, the widefield and the point scanning microscopes. We have discussed the working principles, various parameters and image formation theory of an important point scanning microscope called confocal microscope. We then described the essential components of a confocal system. This is followed by a discussion on the issues with a laser scanning confocal microscope which are yet to be addressed adequately. The chapter ends with the objective of the thesis work, which is to address some of such issues with the confocal system.

In this thesis work, we make an extensive use of the computer generated holography technique to develop a confocal like system where the above mentioned issues are addressed. Hence, in the next chapter we provide a discussion on the relevent aspects of computer generated holography.

Chapter 2

Computer generated holography and liquid crystal spatial light modulator

2.1 Introduction

As described in chapter 1, the present thesis work is going to implement a laser scanning confocal microscope where the illumination beam is configured using a computer generated holography technique. Dynamic control over the illumination beam is made possible by the use of liquid crystal spatial light modulator devices to write binary holograms in a dynamic fashion. In this chapter, we first describe the principle of holography with an emphasis on reconstruction of the object beam wavefront. This is followed by an introduction to binary diffraction holograms, generated using a computer generated holography technique, which likewise classical holography can reconstruct the corresponding object beam wavefront. The binary holograms can be written and reconfigured in real time using a liquid crystal spatial light modulator device. The chapter then discusses the properties of the liquid crystal spatial light modulator devices and how same can be used to write binary holograms. The chapter ends with a discussion on aliasing effect that arises while implementing binary holograms using pixellated device like the liquid crystal spatial light modulator.

2.2 Classical holography

Holography is a technique that enables to observe the three dimensional perspective in the image of an object. In contrast, a photograph of an object records the intensity variation of the object plane. When viewed, the photograph provides only a two dimensional perspective of the three dimensional object. While in the case of holography, the depth information of the object scene can be extracted, since it facilitates reconstruction of the object beam. Dennis Gabor, in 1949 demonstrated the recording of a hologram and reconstruction of the object wavefront from the recorded hologram. A hologram can be defined as the record of the interference pattern between two beams [48], namely the reference beam and the object beam. The interference pattern can be recorded on a high density photographic plate or film. Since the technique is interference based, a light source of high degree of coherence is required in holography.

The experimental arrangement for the recording of a hologram is shown in Fig. 2.1 (a). As seen in the figure a collimated laser beam is split into two by a beam splitter (BS). The transmitted part, termed as the reference beam is allowed to fall on the interference plane. The reflected part is incident on the object, whose hologram is to be recorded. The beam after reflection or scattered from the object is known as the object beam, is allowed to meet the reference beam in the interference plane. A photographic plate records the interference pattern and the developed plate is known as the hologram. When the recorded hologram is illuminated by the reference beam, kept at the same location and orientation as during its recording, the reference beam gets diffracted by the hologram. Due to the diffraction, three beams appear on the other side of the hologram as shown in Fig. 2.1 (b). Among the three diffracted orders, the undiffracted order is the replica of the reference beam. The +1 order has the same phase profile as the object beam and the -1 order has phase profile which is complex conjugate of the object beam.

The generation of the object beam and the other orders can be understood mathematically as described bellow. The intensity distribution in the interference plane, due to the two fields E_r and E_o, corresponding to the reference beam and the object beam can be written as

$$I = |E_r + E_o|^2 \tag{2.1}$$

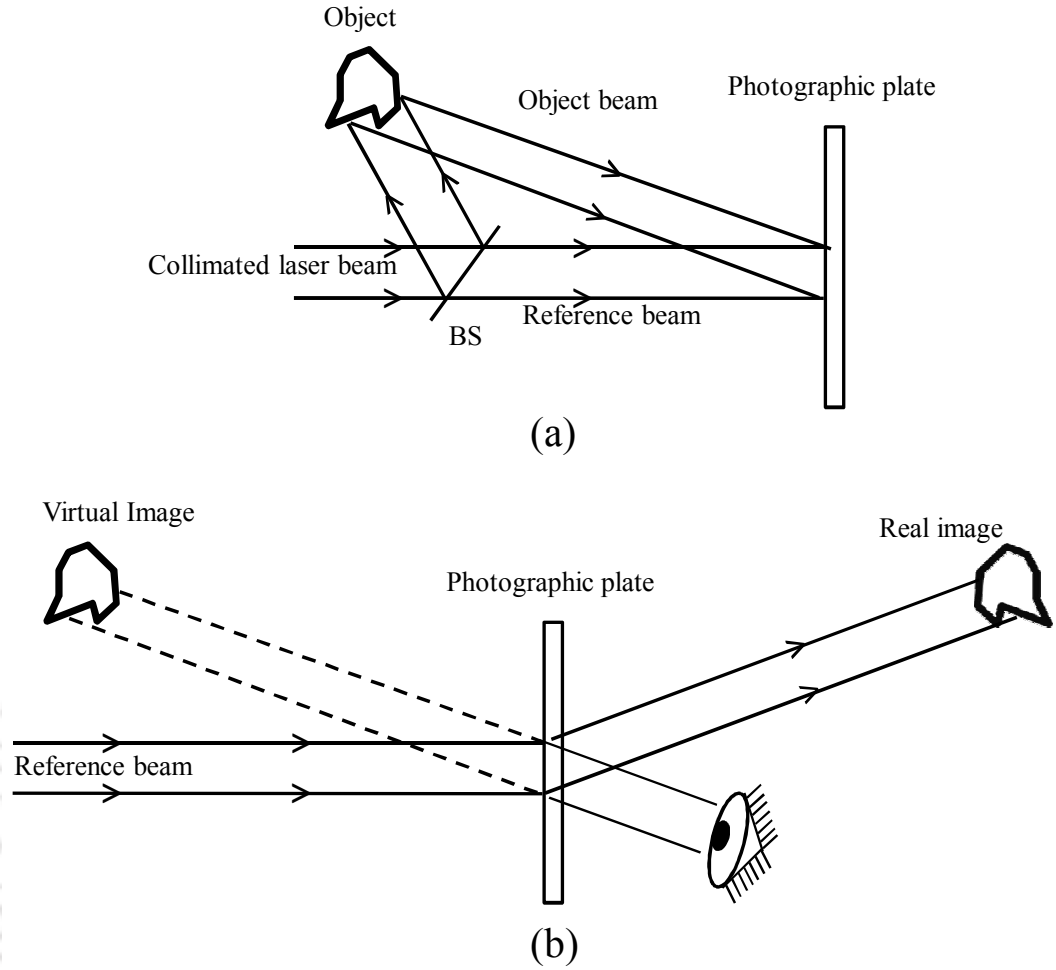

Figure 2.1: (a) Recording of a hologram, and (b) reconstruction of the object beam wavefront.

The two fields are expressed as

$$E_r = A_r \exp(i(kz - \omega t)) \tag{2.2}$$

$$E_o = A_o \exp(i(kr - \omega t)) \tag{2.3}$$

Here A_o and A_r are the complex amplitude profiles of the object beam and the reference beam, respectively. Thus, we have

$$I = |A_r|^2 + |A_o|^2 + A_o A_r^* \exp(ik(r - z)) + A_o^* A_r \exp(ik(z - r)) \tag{2.4}$$

Now for an incident beam of intensity I, the transmittance of the developed plate

can be expressed as [49]

$$T^2 = 1 - \alpha I \tag{2.5}$$

$$T \approx 1 - \frac{1}{2}\alpha I \tag{2.6}$$

where α is a constant. Thus the transmittance T of the plate is proportional to the incident intensity. Hence if the hologram is illuminated by the reference beam, the transmitted wave can be written as

$$\begin{aligned} E_t = TE_r &= (1 - \frac{1}{2}\alpha I)A_r \exp(i(kz - \omega t)) \\ &= (1 - \frac{\alpha}{2}|A_r|^2 - \frac{\alpha}{2}|A_o|^2)A_r \exp(i(kz - \omega t)) \\ &\quad -\frac{\alpha}{2}A_o|A_r|^2 \exp(i(kr - \omega t)) \\ &\quad -\frac{\alpha}{2}A_o^* A_r^2 \exp(2ikz)\exp(i(-kr - \omega t)) \end{aligned} \tag{2.7}$$

Among the terms on the R.H.S. of the above equation, the second term represents the +1 diffraction order, which has the same phase profile as the object beam. The other two terms represent the undiffracted 0 order and the -1 diffracted order. Therefore, when one looks through the hologram in the direction of the object beam, a virtual object appears at the place where the original object was located. This is the virtual image of the object having the three dimensional (3D) perspective. The -1 order beam converges to form a real image of the object.

From the above discussion it is observed that a beam with arbitrary phase profile can be reconstructed if the hologram or the interference pattern corresponding to the beam and the reference beam is available or known. If a hologram can be constructed, the corresponding object beam can be generated even without the presence of real object beam. In such cases the hologram can be obtained from an interference pattern that is computed by a technique called computer generated holography.

2.3 Computer generated holography

The computer generated holography (CGH) technique was introduced as early as in 1960s by B. R. Brown, D. P. Paris and A. W. Lohmann [50, 51, 52]. They synthesized holograms such as binary Fraunhofer holograms, binary spatial filtering mask, and binary holograms using a computer. The process of producing CGH

consists of a few steps such as representation of the complex amplitude profile of the object in the hologram plane, simulation of the interference pattern due to the superposition between the reference beam and the object beam and printing of the pattern onto a mask or film for subsequent illumination by the suitable coherent light source. Thus this technique makes it possible to reconstruct optical wavefronts from numerically specified objects. The CGH technique has got advantages compared to the conventional holography technique. As there is no physical beam in CGH, there is no constraints due to vibration, air turbulence, etc, during the recording of the hologram. Another advantage of the CGH is that instead of the sinusoidal varying fringe pattern in the hologram, a square wave fringe pattern can be written. Such binary transmittance pattern can be realized more easily and accurately compared to a sinusoidal transmittance pattern.

2.3.1 Generation of wavefront with constant amplitude

As previously described, a user defined wavefront can be generated using the principle of holography. The basic experimental arrangement for generating a wavefront with constant amplitude and phase is shown in Fig. 2.2. P_1P_2 is the plane where the wavefront of the object is described. Let the phase of the beam in the plane, barring the tilts, is represented by $\phi(x, y)$ where (x, y) are the coordinates in the plane. The amount deflection of the desired beam on the plane P_1P_2 is represented by m_x and m_y along the x and y axes, respectively. So the resultant phase of the beam on the plane P_1P_2 is represented by

$$\Phi(x, y) = \phi(x, y) + xm_x + ym_y \tag{2.8}$$

The complex amplitude of the object beam with unit amplitude can be written as $A(x, y) = e^{i\Phi(x,y)}$. The phase in the object beam on the plane P_1P_2, in a small area around the point (x, y), is described by a transmittance value of the corresponding location in the hologram plane, given by

$$t(x, y) = \begin{cases} 1 & \text{if } \cos(\Phi(x, y)) \geq 0 \\ 0 & \text{if } \cos(\Phi(x, y)) < 0 \end{cases} \tag{2.9}$$

If a collimated laser beam of unit amplitude is transmitted through the hologram, the amplitude of the beam immediately after the hologram plane is given by the

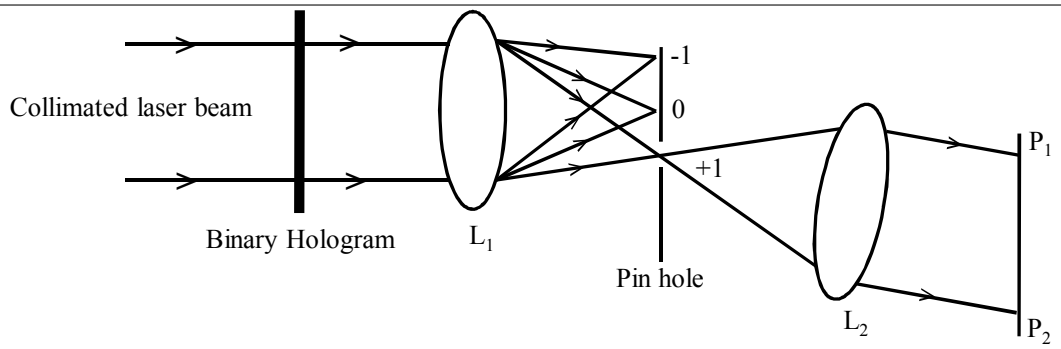

Figure 2.2: The experimental setup for generation of the desired wavefront using binary amplitude hologram. The diffraction orders higher than ±1 order are not shown in the figure.

transmittance function $t(x, y)$.

It can be seen that the plot between t and Φ is a square wave. If a collimated laser beam is incident on the hologram, the beam gets diffracted. The generation of the diffraction orders can be understood from the Fourier series expansion of the transmittance function of the grating. The Fourier expansion of $t(x, y)$ can be written as

$$t(x,y) = \frac{1}{2} + \frac{1}{\pi}\left[\{\exp(i\Phi) + \exp(-i\Phi)\} - \frac{1}{3}\{\exp(3i\Phi) + \exp(-3i\Phi)\} + \frac{1}{5}\{\exp(5i\Phi) + \exp(-5i\Phi)\} - .....\right] \quad (2.10)$$

Thus, it results in odd diffraction orders $\pm1, \pm3, \pm5$, ... along with the undiffracted zero order, which are focused by the lens L_1, kept at a distance equal to its focal length from the hologram plane.

The diffraction pattern of $t(x, y)$ at the back focal plane of the lens L_1 due to the binary hologram placed at the front focal plane of the lens can be expressed as [7]

$$F(f_x, f_y) = \int_{-\infty}^{+\infty} t(x,y) \exp\{-2i\pi(xf_x + yf_y)/f_1\lambda\} dxdy \quad (2.11)$$

where (f_x, f_y) are the coordinates at the back focal plane of the lens L_1, λ is the wavelength of the incident laser beam, and f_1 is the focal length of the lens L_1. Due to the tilt added to the function, the diffraction orders $\pm1, \pm3, \pm5$, ... are located at relative distances of $\pm1, \pm3, \pm5$, ... with respect to the undiffracted order. The diffracted orders have relative intensities $1/\pi^2$, $1/9\pi^2$, $1/25\pi^2$,... and

carry relative phases $\pm\phi, \pm 3\phi, \pm 5\phi, \ldots$. Thus among the diffraction orders the +1 order beam carries the information of the phase ϕ and its location with respect to the undiffracted order is determined by the values of m_x and m_y . In the back focal plane of L_1, the +1 order spot is isolated from the other orders using an iris diaphragm. The beam is then recollimated using another lens L_2 to get the desired wavefront on the plane P_1P_2. From the arrangement in Fig. 2.2 it can be seen that the two lenses L_1 and L_2 constitute a 4f relay system. The plane P_1P_2 and the plane of the hologram are optically conjugate. Therefore, it is possible to describe the phase profile and tilt in the beam by varying the transmittance value of the binary hologram with suitable values of m_x, m_y and ϕ.

In this thesis we often use the function $\phi(x, y)$ to represent monochromatic aberrations expressed as a linear combination of single index Zernike polynomials [53]. The table below shows a few of such Zernike polynomials corresponding to some common optical aberrations. If ϕ =0 the hologram is a square wave grating that

j	Z_j(x, y)	Name
4	$\sqrt{3}(2(x^2+y^2)-1)$	Defocus
5	$\sqrt{6}(x^2-y^2)$	Primary astigmatism at ±45°
6	$2\sqrt{6}xy$	Primary astigmatism at 0°
7	$\sqrt{8}(3(x^2+y^2)-2)x$	Primary x coma
8	$\sqrt{8}(3(x^2+y^2)-2)y$	Primary y coma
9	$\sqrt{8}(x^3-3y^2x)$	x trefoil
10	$\sqrt{8}(3x^2y-y^3)$	y trefoil
11	$\sqrt{5}(6(x^2+y^2)^2-6(x^2+y^2)+1)$	Primary spherical aberration

Table 2.1: Single index Zernike polynomials with index varying from 4 to 11.

corresponds to a plane wavefront beam traveling in a particular direction determined by the values of m_x and m_y. Such a hologram with $m_x = 7\pi$ and $m_y = 0$ is shown in Fig. 2.3 (a). A hologram with $\phi(x, y) = Z_4$, where Z_4 is the Zernike polynomial, corresponding to defocus, and with tilt $m_x = 7\pi$ and $m_y = 0$, is shown in Fig. 2.3 (b).

2.3.2 Generation of wavefront with variable intensity in the beam

The wavefront reconstructed in the previous section has a constant amplitude irrespective of the different phase profiles that may be generated. However there are

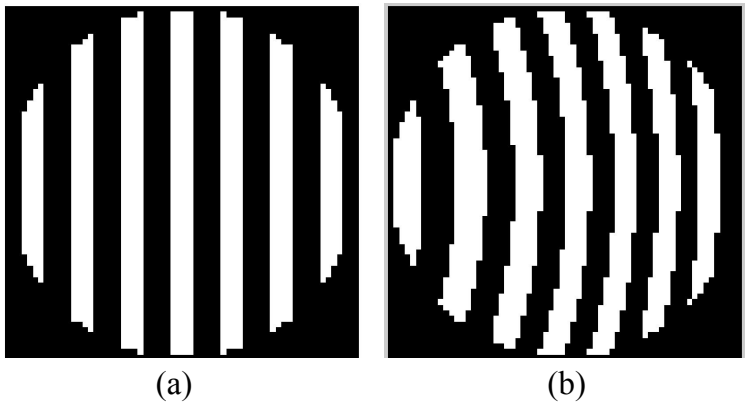

Figure 2.3: (a) A binary hologram without added phase, and (b) a binary hologram with added phase.

applications demanding beams with different phase profiles, each having a user defined amplitude (uniform over the beam cross section). The technique discussed previously can be extended for generating wavefront with such variable amplitude. The hologram written in the above discussion is a square wave i.e., the width of the transparent and opaque portions are same. In order to obtain amplitude variation in the +1 diffraction order, the transmittance plot of the hologram for each cycle of Φ need to be modified.

The transmittance values in the equation 2.9 can be plotted against the locations (say along x axis) as shown in Fig. 2.4 (a). The width of the transparent portion is represented by a while opaque portion is represented by b for a full cycle of width $a+b$. For obtaining the amplitude variation, the duty cycle (dc) has to be varied, since the efficiency of the +1 order diffraction beam depends on the duty cycle. The duty cycle of a grating is defined as the ratio of the transmittance width to the width of the full cycle or period i.e., $a/(a+b)$. It is to be noted here that the duty cycle of a grating can vary from minimum of 0 to maximum of 1. The hologram represented by equation 2.9 has the duty cycle 0.5. Considering a grating profile with duty cycle dc, the Fourier series expansion can be written as [54]

$$\begin{aligned} p(x) &= d + \frac{2}{\pi}\left[\sin(\pi\, dc) + \frac{1}{2}\sin(2\pi\, dc)\right. \\ &\quad \left. + \frac{1}{3}\sin(3\pi\, dc) + \frac{1}{4}\sin(4\pi\, dc) + ...\right] \end{aligned} \tag{2.12}$$

It can be seen that when the width of the transparent and opaque portions are equal i.e., $a = b$, the even order terms on the right hand side vanishes and becomes

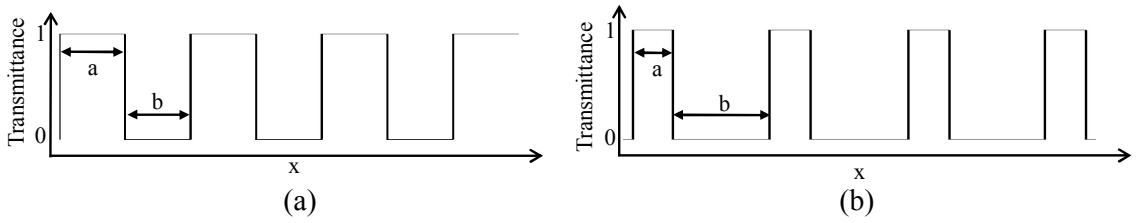

Figure 2.4: Line plots of the transmittance corresponding to (a) a binary transmittance hologram with duty cycle=0.5, and (b) a binary transmittance hologram with duty cycle < 0.5.

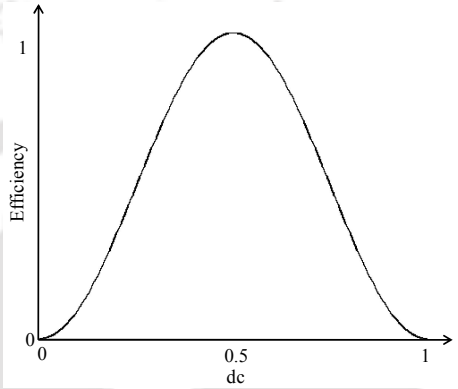

Figure 2.5: Plot of the efficiency of the +1 diffracted order as a function of duty cycle.

equivalent to equation 2.10. The diffraction efficiency of the +1 diffraction order is given by

$$\eta = \frac{1}{\pi^2}[\sin(\pi\, dc)]^2 \tag{2.13}$$

The plot between the normalized diffraction efficiency of the +1 order diffracted beam and the duty cycle is shown in Fig. 2.5. It is seen that the efficiency is maximum when $dc = 0.5$ and vanishes at $dc = 0$ and 1.

Thus to obtain the desired amplitude or intensity (say I) in the +1 order beam, the transmittance function of the hologram is expressed as

$$t(x,y) = \begin{cases} 1 & \text{if} \cos\left(\Phi(x,y)\right) \geq \cos(\sin^{-1}(I)) \\ 0 & \text{if} \cos\left(\Phi(x,y)\right) < \cos(\sin^{-1}(I)) \end{cases} \tag{2.14}$$

Hence for obtaining the +1 diffraction order with reduced intensity, the duty cycle is to be reduced accordingly. Figure 2.6 (a) shows a binary hologram with duty cycle < 0.5. The transmittance values of the hologram is plotted against the locations (say along x axis) and shown in Fig. 2.4 (b). When the duty cycle is equal to 0 or 1, hologram is either completely opaque or completely transparent and hence there

Figure 2.6: (a) A binary hologram for a plane wavefront object beam with duty cycle < 0.5, and (b) a binary hologram with added phase and having duty cycle < 0.5.

is no diffraction.

In order to obtain both user defined uniform amplitude and phase profile simultaneously, the appropriate change in the duty cycle along with the phase $\phi(x, y)$ need to be incorporated while computing the hologram. Such a hologram with user defined duty cycle < 0.5 and added phase is shown in Fig. 2.6 (b)

2.4 Liquid crystal spatial light modulators

Spatial light modulator (SLM), as the name suggests, is a device that modulates the properties of an incident light beam such as amplitude, phase or both amplitude and phase simultaneously in real time. There are several devices, for example, acousto optic SLMs, magneto-optic SLMs, deformable mirror SLM, and, liquid crystal (LC) SLMs, which can modulate the incident light. Among the SLMs the liquid crystal SLMs are one of the most popular devices and are extensively used due to their relatively fast switching mechanism and easy integrability with a computer. LCSLMs have been used extensively in laser beam shaping [55, 56], optical tweezers [57, 58] and optical micro manipulation [59].

LC molecules, discovered by Fried Rich Renitzer in 1888, has the physical properties that lie between conventional liquid and solid crystal state. Like liquid molecules they have some degrees of freedom such as rotation or translation but they are oriented with respect to one another with some orderliness like solid crystals [60]. However the molecules of LC are not rigidly bound to one another.

Primarily there are three types of LC molecules, namely, thermotropic, lyotropic

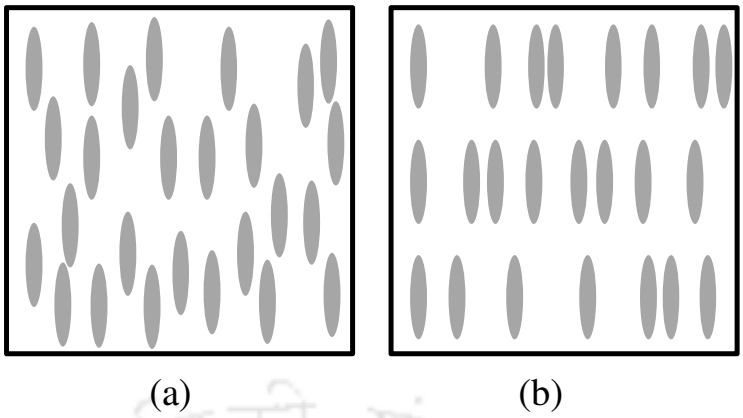

Figure 2.7: Orientation of the molecules in (a) nematic liquid crystals, and (b) smectic liquid crystals.

and polymeric. Among them, thermotropic LC has been studied extensively and has found applications in the areas such as flat display panels [61], light switches [62] and temperature sensors [63]. Thermotropic LC have temperature dependent physical properties such as refractive index, dielectric constants, elastic constants and viscosities. These LC molecule goes through a series of phase transition from solid to liquid crystal, then isotropic liquid and finally to vapour phase when the temperature is increased. Thermotropic LCs can exist in three phases, (1) nematic, (2) cholestric, and, (3) smectic. Among them nematic and smectic liquid crystal phases are mostly used for displays on spatial light modulators.

The liquid crystals are composed of molecules having ellipsoid like shapes with a major axis termed the long axis of the molecule. In nematic LC, the centers of molecules are randomly located all over the volume and the long axis of the molecules points in a certain direction known as the director axis as shown in Fig. 2.7 (a). While in smectic LC, molecules are distributed randomly but in distinct layers as shown in Fig. 2.7 (b). The director axis can be reoriented by the application of an external electric field, magnetic field or optical field, when the field strength exceeds the Free Dericksz transition threshold [64].

Due to their birefringent property, the reorientation of the director axis by the external field imparts a large phase change on the optical field traversing the LC [65]. When the electric field of the incident light is parallel to the long axis of the molecule, light interacts strongly and experiences higher refractive index than the light with electric field perpendicular to the long axis of molecules. The reorientation of the molecular axis due to application of the external electric field is exploited in LC based

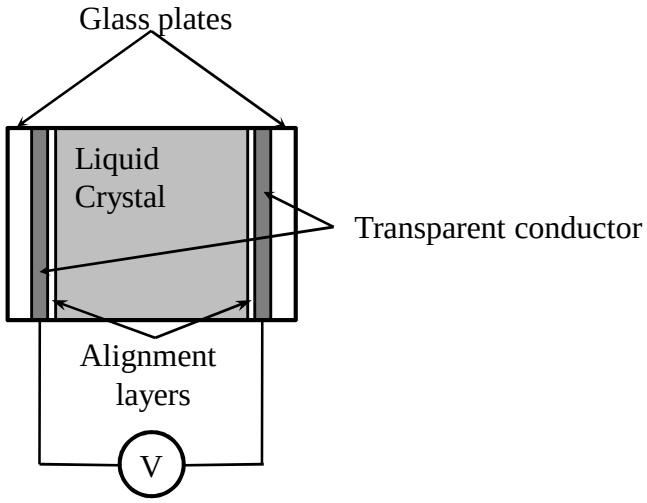

Figure 2.8: Structure of a liquid crystal cell.

SLM to achieve amplitude, phase or polarization modulation of the incident light. Such an SLM comprises a 2D array of LC cells. In the case of electrically addressed SLM, light transmittance property of each LC cell is controlled by applying an electric field across the volume. However there are SLMs where the LC cell can be optically addressed. In this thesis electrically addressed LCSLM is employed and hence more emphasis is given on electrically addressed LCSLM.

The cross section of an electrically addressed LC cell is shown in Fig. 2.8. As seen, a small volume of LC molecules is sandwiched between two transparent conductive plates such as indium tin oxide. Inside the conductive layer, another layer known as alignment layer is coated. The function of the alignment layer is to keep the molecules in a particular orientation. This is achieved by rubbing the alignment layers in a particular direction such that the long axis of the molecules in touch with the alignment layers remain parallel to the rubbed direction, which corresponds to the minimum energy configuration of the arrangement. The LCSLM working in the transmissive mode can be converted into a reflective one. To do this the transparent conductor, the layer through which light emerges, is replaced by a conducting mirror.

2.4.1 Nematic liquid crystal spatial light modulators

A nematic liquid crystal spatial light modulator comprises a 2D array of LC cells containing the molecules in the nematic phase. For using a nematic phase LC cell in

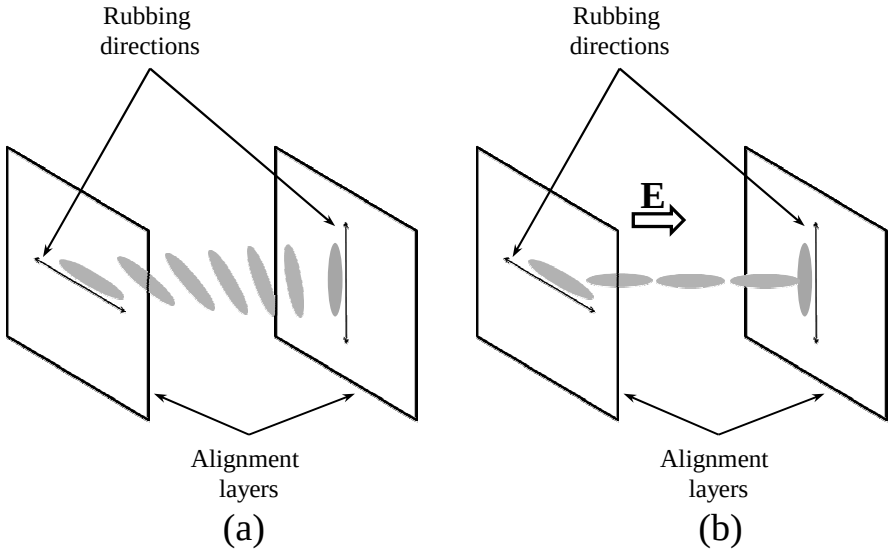

Figure 2.9: Orientation of the molecules in a twisted nematic liquid crystal cell (a) in the absence of external electric field, and (b) in the presence of external electric field $\vec{E}$.

transmitting mode, the LC molecules are sandwiched between two transparent conducting layers which are rubbed in mutually perpendicular directions. The molecules in touch with the layers keep their long axis parallel to the rubbed direction while other molecules rotate like a helix from the entrance face to the exit face as shown in Fig. 2.9 (a) to keep the energy of the configuration minimum [7]. When a beam of light is incident at the entrance face of the cell, polarized parallel to the rubbing direction, the light undergoes polarization rotation by 90^0 after passing through the cell. An analyzer placed at the exit face of the cell with its polarization axis parallel to the rubbing directions in the exit face will then transmit the light. On the other hand, when an external electric field of sufficient strength is applied across the cell, the molecules reorient in such a way that the long axis of the molecule become parallel to the direction of applied field. To avoid any damage to the LC material, AC voltages of RMS value of the order of 5 volts are applied between the two layers. In the presence of applied electric field, the polarization rotation of the incident beam does not take place, as the polarization of the incident beam is perpendicular to the director axis. In such a case light emerges with the same polarization as the incident beam and the analyzer on the exit face blocks the light. Therefore, each cell of an LCSLM can be made transparent or opaque for a collimated light when there is no external applied electric field or when there is an applied electric field.

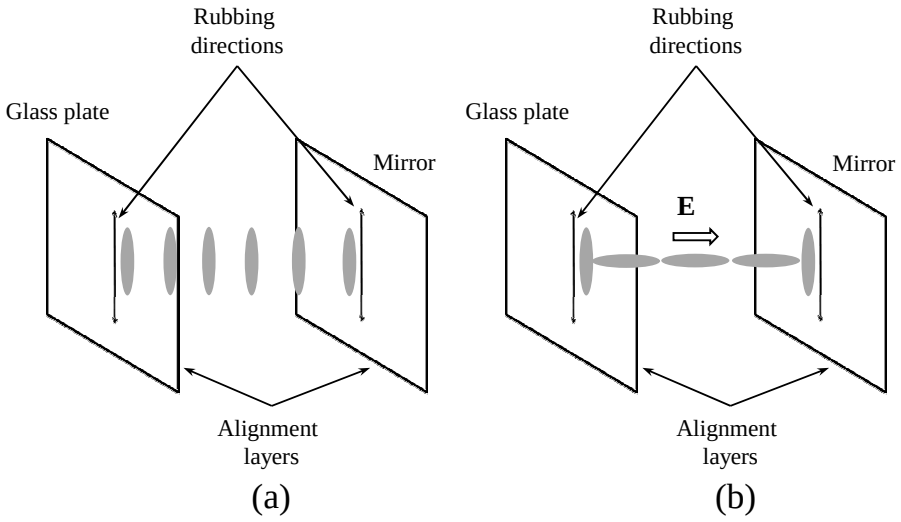

Figure 2.10: Orientation of the molecules in a reflective nematic liquid crystal cell (a) in the absence of external electric field, and (b) in the presence of external electric field $\vec{E}$.

Such an arrangement of LC cell is called twisted nematic LC cell. The orientation of the molecules in a twisted nematic LC cell in the presence of external electric field is shown in Fig. 2.9 (b).

In the case of reflective LC cell, molecules are sandwiched between a transparent layer and a reflective mirror, rubbed in the same direction and all the LC layers have the same director axis. The cross section of a reflective nematic LC cell is shown in Fig. 2.10 (a). Here, the light polarized parallel to the director axis of LC molecule experiences a greater refractive index compared to the light polarized perpendicular to the director axis. The former component can be termed as the extra-ordinary ray while the later can be termed the ordinary ray. The thickness of the cell is so decided that the phase retardation between the extraordinary ray and ordinary ray as the beam travels once through the cell is $\pi/2$ radians. As a result of this retardation of phase, for one pass of the beam the cell acts as a quarter wave plate. When the light polarized at 45^o to the x-axis is incident on the cell in the absence of any external electric field, the light becomes circularly polarized on reaching the mirror placed at other side of the cell. The circularly polarized light is then reflected back by the mirror and reverses the handedness of circular polarization state. When the reflected light comes out of the cell, light again becomes linearly polarized, however, the polarization now is orthogonal to the original polarization. So the polarizer in front of the cell blocks the beam. On the other hand in the presence of an external

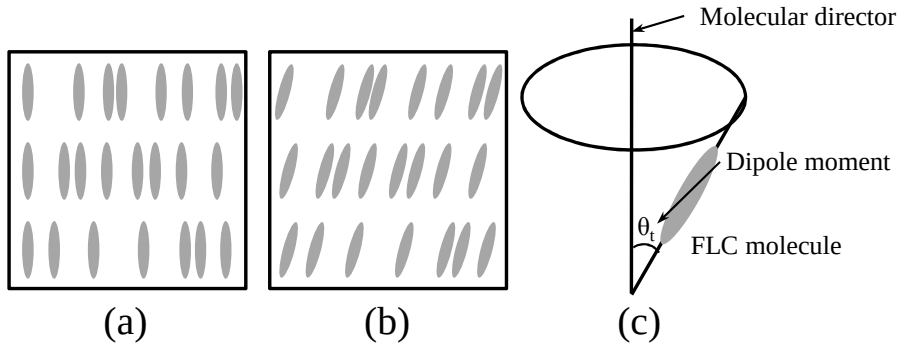

Figure 2.11: Molecular orientation in the (a) smectic A, and (b) smectic C phases. (c) Allowed molecular orientations in a cone in the smectic C* phase.

electric field of sufficient strength, the molecules orient themselves in such a way that the long axis is along the applied field as shown in Fig. 2.10 (b) coinciding with the direction of propagation of the light. Thus, the polarization of the incident light remains unchanged after passage through the cell. When the applied field is not sufficiently large, the molecules do not orient along the applied field completely, resulting in partial transmission of the reflected light.

2.4.2 Ferroelectric liquid crystal spatial light modulator

In 1975 Meyer et al. discovered a new type of LC molecules [66] which is known as Chiral smectic C or smectic C*. This phase of the liquid crystals is commonly known as ferroelectric liquid crystal (FLC). As discussed earlier, smectic liquid crystal molecules are distributed randomly but in distinct layers. In smectic A phase liquid crystal, the molecules are arranged in layers so that molecular long axis is perpendicular to the layer, as shown in Fig. 2.11 (a), while the molecules in smectic C phase are tilted with respect to the layer. As seen from Fig. 2.11 (b), for different layers the long axes of the molecules are tilted with respect to the layer normal and are parallel to one another.

There is a third phase called smectic C* phase, where, for different layers the long axes of the molecules are constrained to lie at an angle θ_t with respect to the layer normal as shown in Fig. 2.11 (c). As one goes from one layer to the adjacent layer the molecules rotate in a cone, thus forming a helical structure. In each layer of the smectic C* phase, LC molecules are ferroelectric in nature. Normally in the macroscopic scale, the smectic C* phase do not exhibit this ferroelectric property. In 1980 Clark et al. demonstrated ferroelectric property in macroscopic scale by

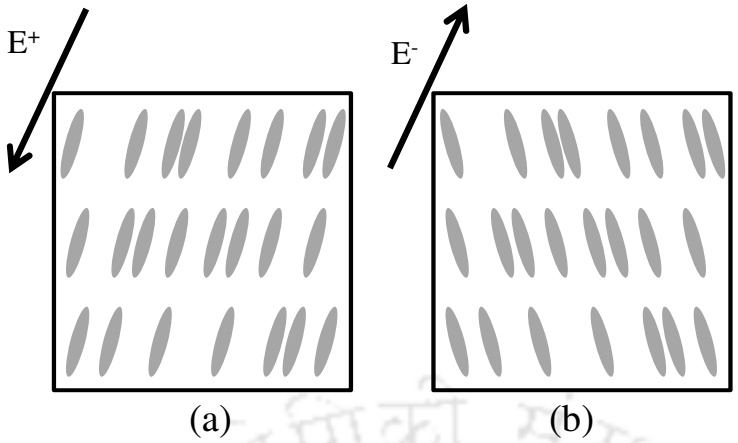

Figure 2.12: Molecular orientation in a smectic C* phases for the applied electric field (a) $\vec{E}^{+}$, and (b) $\vec{E}^{-}$.

smectic C* phase. For this the material is constrained to be in a region between two plates. The separation between the two plates is kept equal to fraction of helical pitch of the ferroelectric molecules, which is typically 1 to 5μm. Due to the presence of permanent electric dipole moment of the FLC molecules, their interaction with the applied field is enhanced. They allow only two molecular orientation with respect to the layer normal depending on the direction of the applied field, where the field is applied along the smectic surface. Figure 2.12 (a) and (b) show the molecular orientations at $+\theta_t$ and $-\theta_t$, with respect to the layer normal, for applied fields of opposite polarity. When the external field is withdrawn, the molecules remain in a particular tilt plane. Thus FLC cell is bistable in nature. This is an important feature of smectic C* phase which is not shown by the nematic phase. Due to bistability of the FLC, it can offer fast switching mechanism. The response time for ferroelectric liquid crystals is of the order of 1 μs where as for the case of nematic phase it is of the order of 1ms. This fast response of the FLC molecules is exploited in the spatial light modulator comprising a 2D array of FLC cells. Such a device is called FLCSLM.

Binary amplitude modulation

Like a nematic LCSLM, an FLCSLM can be employed in amplitude modulation of a light beam. Each cell can be made opaque or transparent for a beam using the birefringence property of the cell. A linearly polarized beam, with its polarization parallel to the long axis of molecule, travels through the cell at less speed compared

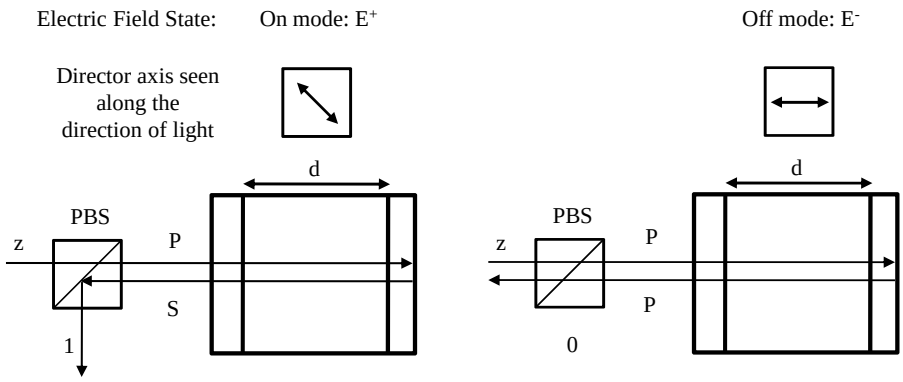

Figure 2.13: Optical arrangement for the demonstration of amplitude modulation by an FLC cell.

to a beam polarized orthogonally. Thus the two directions can be taken as the slow and fast axes, equivalent to a birefringent material. When a linearly polarized beam of light travels through the cell, the electric field decomposes into two components along these two axes. Thus the cell introduces a phase difference of $\Delta = \frac{2\pi}{\lambda} d\delta n$ where λ is the wavelength of light, d is the thickness of the cell and δn is the refractive index difference between the fast and slow axes. As a result, the emergent light is elliptically polarized and the direction of major axis is given by the direction of the long axis.

For obtaining binary amplitude modulation in an incident beam, the optical arrangement is shown in Fig. 2.13. If a randomly polarized beam passes through a polarizing beam splitter (PBS), the transmitted P polarized light is allowed to incident on a FLC cell so that the molecular director is parallel to the direction of the electric field of the incident beam. The cell is so designed that the thickness of the cell along the direction of propagation of light produces a phase difference equal to $\pi/2$ between the two components of light. Since on the other side of the cell a mirror is fitted, as a result the emergent light will have a phase difference π between the two perpendicular components and the cell works as a half wave plate. If the molecular director makes an angle of 0^0 or 45^0 with the incident field, when the electric field applied to the cell is in the negative direction (off mode) or in positive direction (on mode), respectively, the emergent beam will be S polarized or P polarized depending upon whether the cell is in 'off mode' or 'on mode'. Therefore, for 'on mode' the emergent light is reflected by the PBS where as for 'off mode' light is transmitted by the PBS.

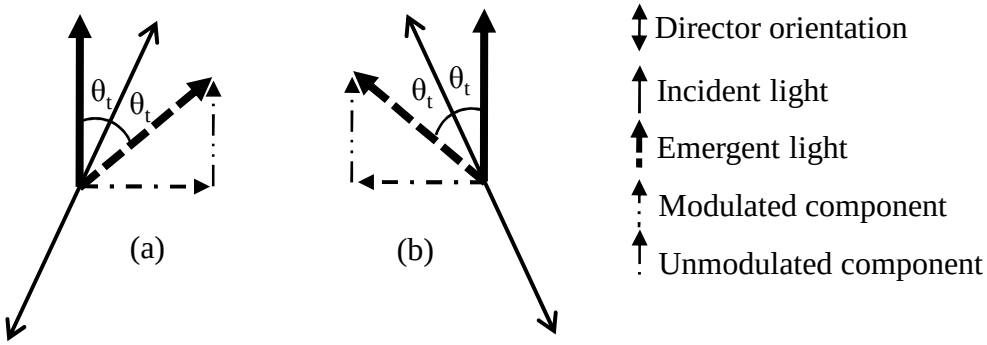

Figure 2.14: Binary phase modulation by the FLC cell.

Binary phase modulation

For getting the binary phase modulation in the emergent beam, the above arrangement is modified in such a way that the incident beam makes an angle equal to the tilt angle θ_t with the molecular director in on mode as shown in Fig. 2.14 (a). Since the cell acts like a half wave plate, the polarization of the emergent beam is rotated by $2\theta_t$ in the clockwise direction. The PBS placed will reflect a component of the emergent beam having S polarization. The amplitude of the reflected beam by the PBS is considered as 1. When the FLC is in off mode, the molecular director rotates by an angle $2\theta_t$ in the anti clock wise direction as shown in Fig. 2.14 (b) giving rise to an amplitude of -1 corresponding to the reflected beam by the PBS. Therefore, pure binary phase modulation can be achieved by changing the polarity of the external electric field, as the emergent beam at the output undergoes a phase modulation of 0^0 or π phase delay. The ideal tilt angle for phase modulation is 45^0 and for amplitude modulation it is 22.5^0. Fortunately, the FLC mixtures can be synthesized for which $\theta_t = 22.5^0$.

2.5 Implementation of binary amplitude or phase hologram using LCSLM

In principle, computer generated holograms can be fabricated using the photographic process or by taking print on a transparent sheet [67]. Photographic plate or film has non linearities which makes it difficult to write the desired hologram accurately. While the hologram printed on a transparent sheet has limitation in terms of exact representation of the hologram due to finite number dots per inch provided by the

printer. More importantly the above two methods can not be used to dynamically reconfigure the hologram.

As discussed earlier, binary amplitude or phase modulation of light can be realized using an LCSLM. Thus it is possible to implement binary amplitude or phase hologram by writing the hologram pattern on the LCSLM panel. Since the computer interface attached with the LCSLM allows the user to update the pattern at least at the video rate, it is possible to realize binary holograms that can be reconfigured in real time. This consequently gives rise to diffracted beam from the hologram with a wavefront and intensity as designed by the user which can be controlled dynamically. However, due to finite size and number of the pixels in the LCSLM, holograms upto a certain spatial frequency can only be implemented.

To describe one interference fringe with an LCSLM, there is a requirement of at least two pixels. When the total number of fringes in the hologram pattern is more than half of the pixels in the LCSLM panel, a phenomenon called the aliasing effect comes into play.

2.6 Aliasing effect in binary holograms and minimization of aliasing effect using random binarisation technique

The effect of aliasing appears when a continuous function is represented by an under sampled discrete function. In such cases the continuous function is not properly represented by the discrete function. In order to digitize the continuous function faithfully the function must be sampled at least at the Nyquist rate, that is at a rate at least twice the maximum frequency present in the function. When the digitization is under sampled, the higher frequency components present in the function appear in the discrete form as low frequency components.

Figure 2.15 (a) shows a sinusoidal function with frequency f_c. If this function is sampled at $f_s = 2f_c$ then it is sufficient to capture each wave in the function. In this case the function can be faithfully reconstructed as shown in Fig. 2.15 (b). On the other hand, if the function is sampled at a rate below the Nyquist rate, say $f_s = 1.5f_c$ (shown in Fig. 2.16 (a)), then there are not enough sample points to capture all the waves in the function. The reconstructed function is shown in

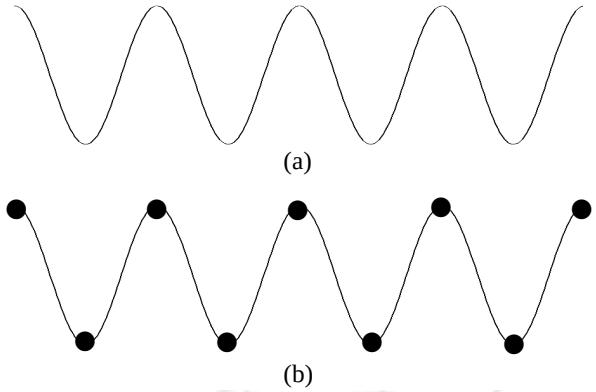

Figure 2.15: (a) A sinusoidal wave with frequency f_c. (b) Sampling of the sinusoidal wave at the rate $f_s = 2f_c$.

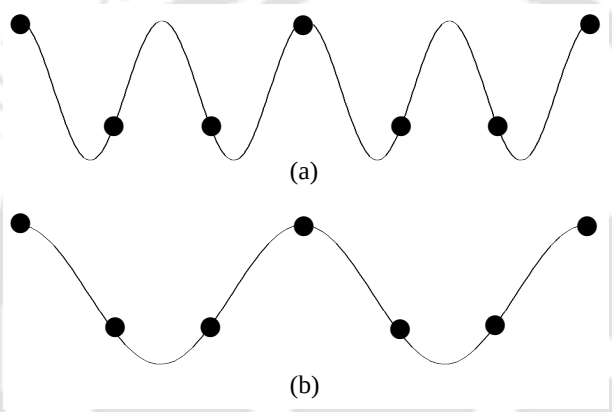

Figure 2.16: (a) A sinusoidal wave with sampling rate $1.5f_c$, and (b) Reconstructed function after sampling at the rate in (a).

Fig. 2.16 (b), which appear to have a lower frequency. Therefore, when a function is under sampled we not only loose information but also get wrong information about the function. In the case of the LCSLM, not less than two pixels should be used to describe one complete sine wave. Hence, for an arbitrary sinusoidal function, the sampling rate f_s should be at least π radian per pixel. For a sinusoidal function with spatial frequency f_m described over the discrete variable x as the pixel index, we can write

$$\sin(xf_m) = \sin(xf_m - xN\pi) = \sin(x(f_m - Nf_s)) \tag{2.15}$$

where N is an even number. From above expression it is seen that the reconstructed function contains the spatial frequency $(f_m - Nf_s)$.

The hologram implemented in this thesis is based on square wave modulation along X and Y direction of the incident wavefront. Due to the square wave modula-

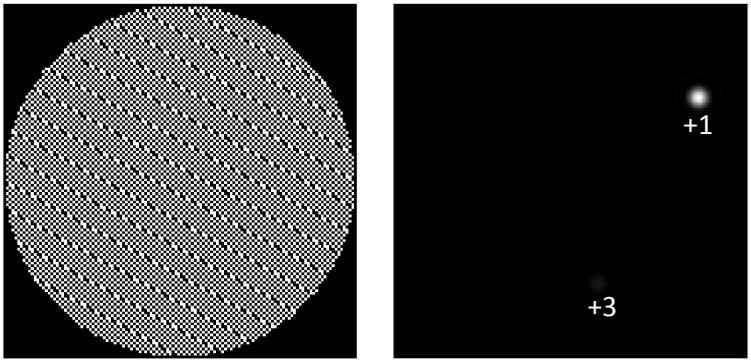

Figure 2.17: (a) A binary hologram described over 128×128 pixels with X tilt 60π and Y tilt 70π. (b) The corresponding diffraction pattern shows that the +3 order appears as the aliased order near the +1 order.

tion, the modulated wavefront contains an infinite number of spatial frequency components such as $(f_n, 3f_n, 5f_n, ...\infty)$ corresponding to the orders $(\pm1, \pm3, \pm5, ...\pm\infty)$ in the diffraction pattern. Here f_n is the frequency of the first harmonic. The orders with spatial frequency above the Nyquist frequency appear in the diffraction pattern as low spatial frequency orders. These low frequency orders are known as the aliased orders. One may find the locations of the aliased orders in the Fourier plane by using equation 2.15.

Figure 2.17 (a) shows a binary hologram described over a diameter 128 pixels with overall tilt 60π along X direction and 70π along Y direction. The values of the tilts along X and Y directions are so chosen that ±1 diffraction orders have spatial frequency below the Nyquist frequency. Therefore, they appear in the Fourier plane at locations proportional to the tilt values. While the higher orders have frequencies above the Nyquist frequency and as a result they appear in the Fourier plane as the aliased orders. The diffracted orders +1 along with the aliased order +3 appearing in the Fourier plane are shown in Fig. 2.17 (b).

From the above discussion it is seen that when a beam is modulated with square wave amplitude or phase modulation, infinite numbers of harmonics are generated in the diffraction plane as the aliased orders. In some circumstances it may happen that some of these aliased orders appear in the vicinity of the +1 order or overlap with it in the Fourier plane. Under this situation the +1 order beam may get corrupted.

Hologram implemented with a pixellated device can not produce purely sinusoidal amplitude variation in the emergent beam immediately after the LCSLM

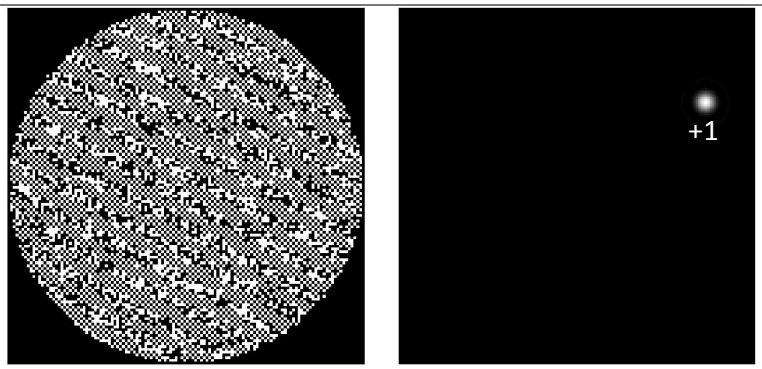

Figure 2.18: (a) A probabilistically sinusoidal binary hologram described over 128×128 pixels with X tilt 60π and Y tilt 70π. (b) The corresponding diffraction pattern shows that the aliased order has disappeared.

display panel. However using the same LCSLM it is possible to generate an amplitude variation which is probabilistically sinusoidal [68]. The equation 2.9 for the generation of the binary hologram can be modified to generate probabilistically sinusoidal amplitude variation in the emergent beam. If $p(x, y)$ is the pixel values of the LCSLM for phase $\Phi(x, y)$ in the $+1$ order beam, considering unit amplitude of the $+1$ order diffraction order, then

$$p(x,y) = \begin{cases} 1 & \text{if} \cos\left(\Phi(x,y)\right) \geq R_n(x,y) \\ 0 & \text{if} \cos\left(\Phi(x,y)\right) < R_n(x,y) \end{cases} \tag{2.16}$$

where $R_n(x, y)$ is a random number between -1 and $+1$. Fig. 2.18 (a) shows a binary hologram generated using equation 2.16 with over all tilt 60π along X direction and 70π along Y direction. The corresponding diffraction pattern in the Fourier plane is shown in Fig. 2.18 (b). From the Fourier plane it is seen that the aliased orders that was appearing in Fig. 2.17 (b) has disappeared and the $+1$ order dominates the Fourier plane. Due to the probabilistically sinusoidal amplitude hologram the aliased orders have been broken down into noise.

2.7 Conclusion

In this chapter we have described the principle of holography and reconstruction of the object beam wavefront using the principle of holography. The processes involved in the creation of digital hologram without having the real object beam have also

been discussed. We then introduce the generation of user defined wavefront using computer generated binary holograms. The chapter then discusses the properties of the LC cells and LCSLM. This is followed by a discussion on the implementation of the computer generated holograms using an LCSLM and the issue of aliasing.

In the next chapter we have implemented the binary hologram based technique to scan a laser beam in a raster fashion similar to a galvo mirror scanner in a laser scanning microscope.

Chapter 3

Beam scanning using binary diffraction holograms

3.1 Introduction

In the previous chapter we discussed the capability of binary diffraction holograms which behave like diffraction gratings, to give rise to a diffracted beam that can travel in a user defined direction. In this chapter, we implement a laser beam scanner using an LCSLM exploiting this capability and highlight some of the issues associated with such a grating. Here, a simple theoretical expression is developed that relates the binary amplitude profile of a grating, both periodic or aperiodic to the amount of beam deflection. The expression is then utilized to find the location of the experimentally generated +1 order diffracted beam. It is shown that experimentally found beam locations matches well with the theoretically predicted locations. The expression is then used to create a map of the theoretical applied slope with the beam deflection angle which can be used to deflect the beam to an exact predefined location. The beam repeatability potential of the scanning mechanism is also demonstrated.

3.2 A review of the beam scanning mechanisms

The laser beam scanner is an essential part to fulfill the scanning requirement of the laser scanning microscope. There are a number of beam scanners that are being implemented in such microscopes. Among them galvanometer based mirror

scanners, as discussed already in chapter 1, are the most commonly used to scan the laser beam. In some other cases polygon mirror, acousto-optics deflector (AOD), grating based scanner etc. are used to scan the beam in a scanning microscope.

A polygon mirror, set to rotate at a constant rate, can generate a constant and uni-directional scan and can provide high scan rate. However due to the difficulty to make the device accurate and vibration free [69], it is not suitable to use in microscopy applications. AODs can scan the beam in a broad range of speed, from a very high frame rate (∼30-120 fps) to an extremely low frame rate (∼1 fps). In addition to the above advantage, the AODs also allow zooming [70, 71]. Here, since the deflection is produced by diffraction, the amount of deflection is proportional to the wavelength of the light beam. On the other hand a grating comprises a periodic variation of the amplitude transmittance or the phase delay. When a laser beam is incident on such a grating, the beam gets diffracted and the amount of deflection of the diffracted beam with respect to the incident beam is a function of grating periodicity and the wavelength of the incident beam. As described in chapter 2, using computer generated holography techniques, gratings of user defined periodicity can be fabricated. The fabricated gratings can be used to make a laser beam to scan a line or an area [72]. The grating based scanner is shown to be a robust scanning mechanism compared to other mechanical scanners. However when such devices with wavelength dependent deflections are used in a scanning microscope, they may create an issue in detecting the signals when the microscope is working in the fluorescent mode. This is because the fluorescent light as emitted by the sample has longer wavelength than the excitation wavelength. Thus the fluorescent light will be deflected by an amount during the descanning, which is different from the corresponding angle during scanning. Therefore, the fluorescent light will not traverse the same path, followed by the incident light, and will therefore fail to pass through the pinhole. Thus, special arrangements are to be incorporated to overcome this dispersion effect.

3.3 Binary hologram based beam scanning using LCSLM

A convenient way of achieving periodic phase delay or amplitude transmittance in an incident beam, is by using a liquid crystal spatial light modulator (LCSLM) to

implement a binary hologram or diffraction grating. The implementation of such a grating or a computer generated hologram using an LCSLM has several advantages such as easy integrability with a computer and the dynamic reconfiguration capability. Using these facilities the spatial frequency of the grating or the hologram on the LCSLM can be updated at least at the video rate. Thus by updating the video signal from the computer program, the diffraction beam can be made to deflect in a desired direction. This facilitates laser beam scanning without mechanical movement of any parts. Since the signal sent to the LCSLM is invariant of time, so the deflection angle of the beam can remain unchanged even as time lapses. Therefore, the scanning mechanism can provide excellent beam repeatability. However, the finite size of the liquid crystal cell of the LCSLM puts a constraint on the accuracy of beam positioning. There have been number of efforts to improve the accuracy in positioning the beam using LCSLM [73, 74, 75].

Making use of the available technology, the hologram computed in a PC can be directly transferred to the LCSLM device. Hence, the exact amplitude transmittance of the hologram sent to the LCSLM can be known. The spatial frequency of the grating pattern is calculated from the overall desired slope (also referred to as applied slope) of the diffracted beam. However when the grating is implemented using a pixellated device having finite number of pixels like LCSLM, the slopes applied to the computed grating may not be exactly represented by the LCSLM. In such a case, for all applied slope values, the amplitude profile may not have equal period over the entire grating plane. Therefore, the grating represented by a pixellated device can have aperiodic grating profile for some applied slope values. Consequently, the relation between the beam deflection angle of the diffracted beam and the applied slope of the grating is not a linear one. In the section to be followed, we develop a theoretical expression to predict the deflection angle of the beam for a given applied slope profile.

3.4 Theoretical considerations

For the development of the expression that can be used to predict the beam deflection angles or the beam position of the diffracted beam for both the periodic and aperiodic gratings, a two dimensional array of $N \times N$ pixels is considered. Along the x-axis of the array, the pixels are represented by $x = (x_1, x_2, \ldots, x_N)$ and along the y-axis the pixels are represented by $y = (y_1, y_2, \ldots, y_N)$. It is also considered that x and y are

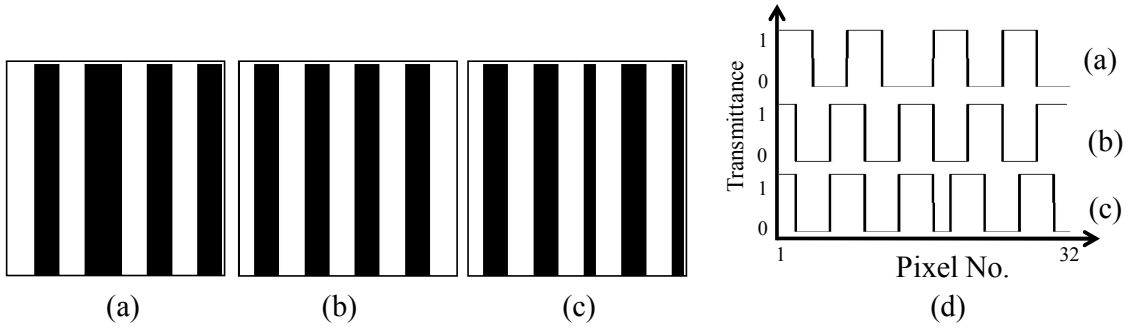

Figure 3.1: Binary amplitude holograms comprising 32×32 pixels generated using applied slopes= (a)7π, (b) 8π, and (c) 9π along x-axis of the grating and (d) line plots of the holograms along x axis.

the normalized coordinates such that their values vary between 0 and 1. Along x-axis the pixel x_1 corresponds to coordinate $x = 0$ and x_N corresponds to coordinate $x = 1$. The intermediate pixels corresponds to the normalized coordinates between 0 and 1.

Let $m(x)$ and $m(y)$ are the functions representing the slopes of the deflected beam expressed in radians along x and y axes respectively. If the wavefront of deflected beam is defined by the phase delay $\phi_d = 0$ at $x = 0$ and $\phi_d = \Phi$ at $x = 1$ then phase delay at any value of x is given by $\phi_d = x.\Phi$. The complex amplitude of the deflected beam at the grating plane is given by $A(x) = e^{im(x)}$. Similarly, along the y-axis of the array the complex amplitude of the deflected beam is written as $A(y) = e^{im(y)}$. Now, for generating a deflection beam in the +1 order beam with slope values $m(x)$ and $m(y)$ along x and y axes, the transmittance value of the gratings, using the computer generated holography technique is given as

$$T(x_n, y_n) = \begin{cases} 1 & \text{if} \cos\{m(x_n) + m(y_n)\} \geq 0 \\ 0 & \text{if} \cos\{m(x_n) + m(y_n)\} < 0 \end{cases} \tag{3.1}$$

Since, the minimum values of the x and y are taken to be 0, it ensures that the amplitude transmittance at $x = 0$ and $y = 0$ is always constant, which is 1 in this case. The angle made by the +1 order beam with the incident beam is given by $\sin^{-1}(\lambda/d)$, where λ is the wavelength of the laser illuminating the grating, provided the $T(x_n, y_n)$ represents a square wave grating profile with uniform period d over the entire grating. However when the gratings, implemented with a pixellated device such as the LCSLM, do not have definite periodicity for all values of $m(x_n)$ and $m(y_n)$, the grating profile becomes aperiodic for many such values of $m(x_n)$ and

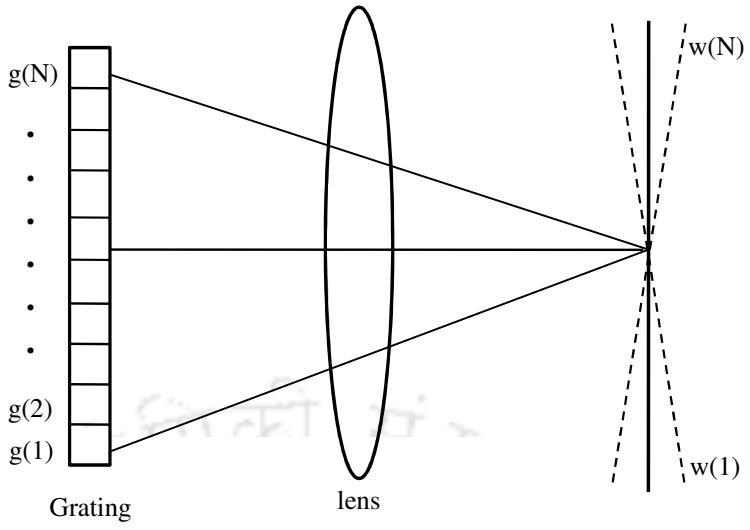

Figure 3.2: Grating comprising N elements denoted by g(1), g(2), ..., g(N) illuminated by a collimated laser beam. w(1), ..., w(N) are the wavefront at the front focal plane of the lens due to each of the corresponding grating elements g(1), g(2), ..., g(N).

$m(y_n)$. Therefore, the above relation for finding the beam deflection angle is not applicable for all values of the $m(x_n)$ and $m(y_n)$. To demonstrate the occurrence of aperiodic gratings when implemented with a pixellated device, a two dimensional array of 32×32 pixels is considered. To this array of pixels, different slope values $m(x_n) = 7\pi$, 8π, and 9π along x-axis at x=1, are applied. The gratings or the binary holograms corresponding to the slope values $m(x_n) = 7\pi$, 8π, and 9π are shown in Fig. 3.1. Line plots along x axis of the holograms is shown in Fig. 3.1 (d). From the plot it can be seen that only the hologram in Fig. 3.1 (b) corresponding to $m(x_n) = 8\pi$ is periodic while the rest are aperiodic.

We consider a one dimensional grating array comprising the grating elements g(1), g(2), ..., g(N) as shown in Fig. 3.2. A lens is placed at a distance equal to its focal length from the grating. It is assumed that the separation between the centers of two adjacent grating elements to be one spatial unit (SU). For the sake of simplified calculation, the locations of the elements along the x-axis are described by the parameter $x'_n = \frac{(2x_n-1)(N-1)}{2}$. The origin of the x'_n coincides with the center of the grating and optic axis of the lens. When the grating is illuminated by a collimated laser beam, each of the grating elements can be considered as coherent point source. The amplitude of each such point source is defined by the function $T(x)$ with x as the locations of the elements. Using the property of Dirac delta function and considering width of each grating element to be infinitely small, the

nth grating element can be written as

$$g(n) = T(x_n)\delta\Big(x'_n + \frac{N-2n+1}{2}\Big) \tag{3.2}$$

The intensity distribution in the focal plane of the lens due to the grating elements can be found by taking the Fourier transform of $g(n)$. Using the property of the Dirac delta function the field in the Fourier plane, having the coordinates f_x, can be written as

$$F(n) = T(x_n)e^{if_x(N-2n+1)\pi} \tag{3.3}$$

Here, it should be noted that the coordinates of f_x varies from $-0.5\frac{1}{SU}$ to $+0.5\frac{1}{SU}$.

Thus, each grating element gives rise to a plane wavefront in the focal plane whose amplitude is given by $T(x_n)$ and the orientation of the wavefront is determined by the location of the grating element. The overall effect of all the grating elements is given by the superposition of all such plane wavefronts. Therefore, the field at the focal plane of the lens is given by $A(f_x) = \sum_n F(n)$. In our case, the location of the diffracted beam is confined to one half of the Fourier plane, which is taken to be the positive half. To describe the amplitude at the Fourier plane another normalized coordinate X, varying between 0 and 1, corresponding to $f_x = 0$ and 1, is considered. Therefore, the intensity distribution in the positive half of the Fourier plane can be written as [76]

$$I(X) = \sum_n T(x_n)e^{iX\frac{(N-2n+1)\pi}{2}} \sum_n T(x_n)e^{-iX\frac{(N-2n+1)\pi}{2}} \tag{3.4}$$

It is to be noted that the above equation appears somewhat similar to discrete Fourier transform (DFT) operations . However there exists a major difference between the proposed scheme and the DFT, that is, the variable X in the proposed expression represents an array extending over the entire plane, while in the case of DFT the similar variable represents a single location. Therefore, in the propose scheme the field over the entire Fourier plane is obtained for each individual grating element. On the other hand, the field at a single coordinate point in the Fourier plane due to all the grating elements is evaluated in the case of DFT. Therefore, if the resultant field due to one grating profile is known, the resultant field due to a similar grating profile with majority of pixel values same as the previous one, can be predicted using the proposed scheme faster than the DFT scheme, just by updating only the changed pixel values in the grating profile. Therefore, when the

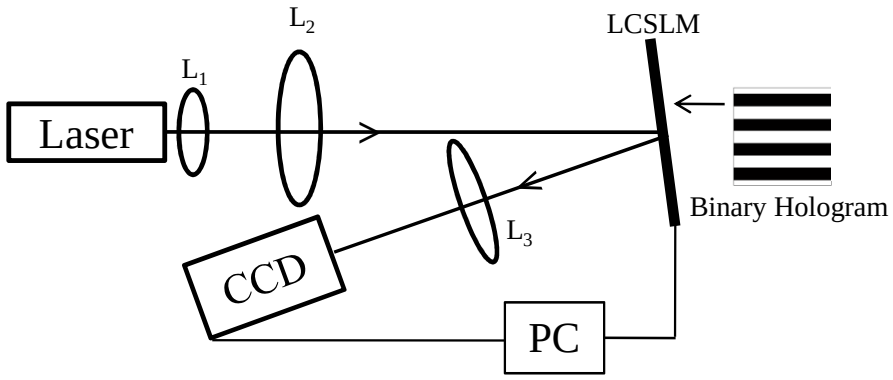

Figure 3.3: The schematic diagram of the experimental arrangement for the measurement of the beam location of the deflected beam.

grating scanner is used for a line scanning or area scanning application, the proposed scheme can perform faster than the DFT based scheme. The proposed scheme is thus computationally less intensive when a large number of grating profiles are considered, with two grating profiles differing from one another over a small number of pixels only. Moreover commonly available numerical tools used for the computation of Fourier transform, such as the fast Fourier transform (FFT), compute the entire Fourier plane. On the other hand, for the proposed scheme it is only over half of the plane.

In the Fourier plane, the first order diffracted beam has the maximum peak intensity and hence its location in the plane can be found by using the following equation

$$X = \arg\max\left(I(X)\right) \tag{3.5}$$

such that $Z_d < X \leq 1$, where Z_d is the half width of the zero order undiffracted beam. Here arg max () is a function that returns the location of the maximum of the argument. From the location of the +1 diffraction order, the slope of the diffracted beam can be found using the relation

$$\nabla_{calc} = X(N-1)\pi \tag{3.6}$$

3.5 Experimental arrangement

The theoretical expressions developed in the previous section are verified using an experimental arrangement shown in Fig. 3.3. The laser beam from a source is

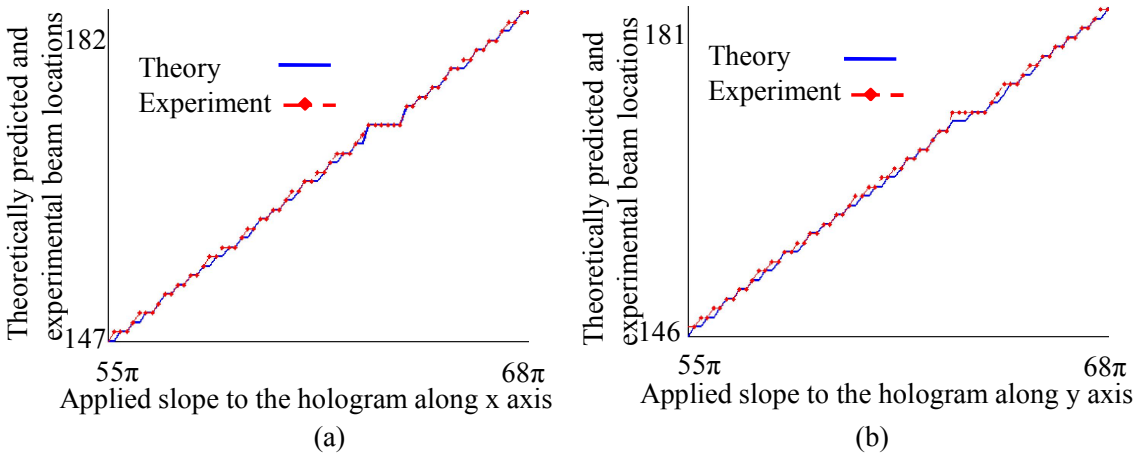

Figure 3.4: The plots of the applied slope to the hologram and the theoretically predicted and experimental beam locations. (a) Slope applied along the x axis, and (b) slope applied along the y axis of the hologram.

expanded and collimated using two lenses L_1 and L_2. The collimated laser beam illuminates the display panel of an LCSLM. Two dimensional binary amplitude transmittance profiles are generated over an array of 128×128 pixels (i.e., N=128) using equation 3.1 for various theoretical or applied slope values (designated as $\nabla_{applied}$). The grating patterns are fed to the LCSLM panel as a video signal through a program running in a computer. The grating is displayed on the LCSLM in such a way that it is uniformly illuminated by the laser beam. The diffracted light by the grating profile is focused by a lens L_3 onto the CCD camera placed at the focal plane of the lens. From the CCD data, accessed by the same computer, the beam location of the +1 diffracted beam is found. The corresponding slope of the deflected beam can be calculated using the equation 3.6.

3.6 Experimental results

The locations of the +1 and the -1 order beams are observed on the CCD camera that correspond to the maximum possible applied slope along x direction (it is 127π in this case) of the hologram in order to find the number of pixels (N_f) comprising the Fourier plane. The Fourier transform of the hologram is then computed over $N_f \times N_f$ pixels for a set of hologram with different slopes. Thus, the theoretically obtained beam locations can be directly compared with the experimental beam locations.

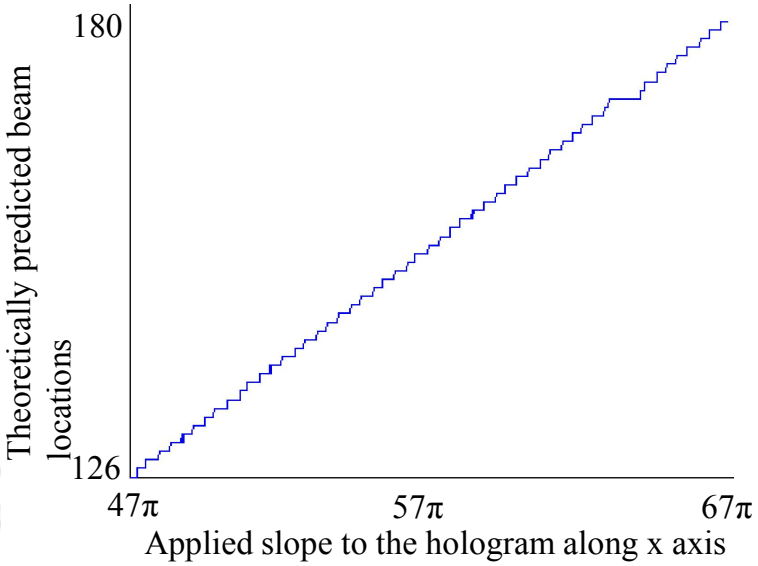

Figure 3.5: The plot of the theoretical beam locations for the applied slope values along the x axis, between 47π and 58.1π in 555 equal steps.

3.6.1 Theoretical and experimental beam locations

To find the beam locations for different applied slopes, we generated 400 holograms with slope along the x-axis of hologram varying from 47π to 127π at regular intervals. For each hologram, the locations of the +1 order beam is found using equation 3.5 and the corresponding location in the CCD camera is recorded. These beam locations for the various applied slopes are plotted and is shown in Fig. 3.4 (a). From the plot, it is seen that the experimentally found beam locations agree well with the theoretically predicted locations. The experimental location is estimated by taking the mean of 10 measurements for each position of the beam. The same experiment is also performed for similar applied slope values along the y-axis of the hologram. The corresponding theoretical and experimental beam locations are shown in Fig. 3.4 (b). It is noticed in the above plots that at some regions the experimental data has deviated from the theoretically predicted data. This deviation from the theoretical data is attributed to the mechanical vibration of the table on which the experiment is performed.

3.6.2 Generation of a regular grid of beam locations

As mentioned earlier, due to the finite number of pixels in the LCSLM as well as in the camera, the relation between the applied slope and the location of the +1 order

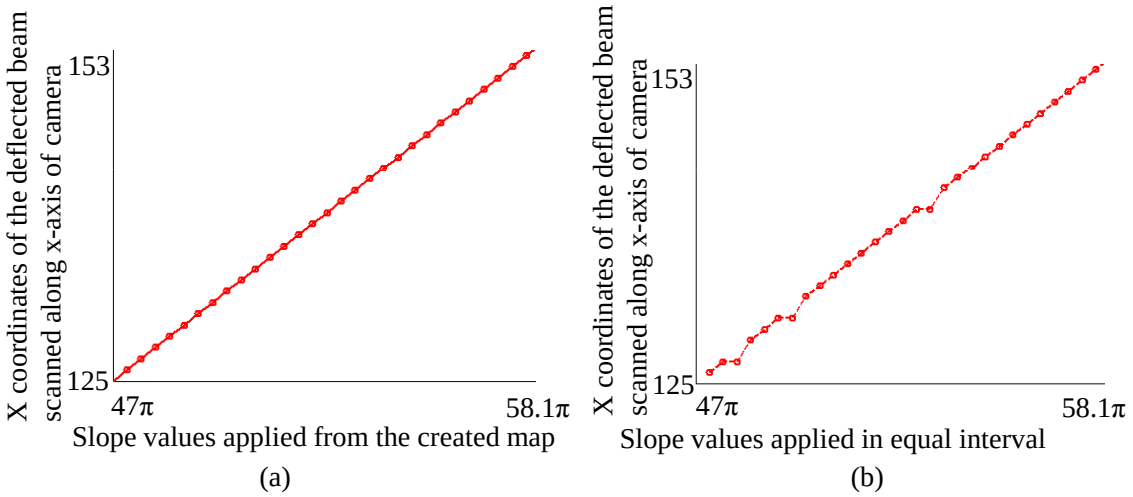

Figure 3.6: The plots of the experimental beam locations deflected along the x axis, when (a) the slope values are applied using the map, and (b) equally spaced slope values are applied.

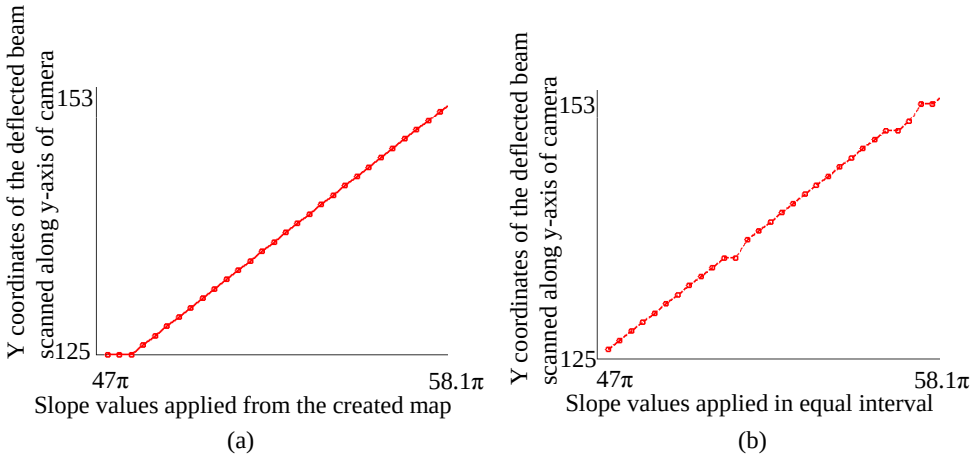

Figure 3.7: The plots of the experimental beam locations deflected along the y axis, when (a) the slope values are applied using the map, and (b) equally spaced slope values are applied.

beam is not linear. Thus even if we apply slopes of equal step size, the resulting beam locations may not be equally spaced. To obtain beam scanning with equal step size, one has to create a map between the applied slope and the corresponding theoretical beam locations. For creating the map we have changed the applied slope along x from 47π to 58.1π in 555 regular intervals, so that for each beam position we have sufficient number of applied slopes. The corresponding theoretical location of the beam is found by computing the Fourier transform over 680×680 pixels. The theoretical beam locations corresponding to these applied slopes are shown in Fig. 3.5. From the recorded data it is seen that the beam moves a distance equal to 29 pixels of the CCD camera. Now for generating beam scanning in equal steps, in this case over 29+1=30 steps, only those applied slopes are chosen which resulted in a regular grid of theoretical beam locations. These chosen slopes are then applied to the hologram on the LCSLM and the corresponding beam locations (mean of 10 measurements) are recorded using the CCD. Fig. 3.6 (a) shows the plot of the experimental beam locations for equal step size beam scanning. The linear plot confirms that scanning with equal step size is achieved. We then applied slopes with uniform step size, in 30 steps between 47π to 58.1π, to the hologram and the corresponding beam locations are recorded. As seen in the Fig. 3.6 (b), for equally spaced applied slopes, equal step size beam scanning is not achieved. To obtain equal step size beam scanning along the y direction, similar map as described above is created. The experimental data for the equal step size beam scanning and equally spaced applied slopes are shown in Fig. 3.7 (a) and (b).

Further to obtain the equal step size beam scanning diagonally, slope values along both the x and y axes are applied simultaneously to the hologram. To create the map, the applied slope values are changed from 47π to 58.1π in 555 steps both along x and y simultaneously. The theoretical locations of the +1 order beam corresponding to these applied slopes are computed and a map between the beam position and the applied slope is created. We then use the map to select 30 applied slope values along x and y axes that will move the beam diagonally in equal steps. These slopes are then applied to compute holograms to be sent to the LCSLM. The experimental beam location in terms of the coordinates along x and y axes of the camera are recorded and are shown in Fig. 3.8 (a) and (b) respectively. The plots describe that the beam moves in equal steps barring a few exceptions. We then applied equally spaced slope values from 47π to 58.1π along both x and y axis of the hologram simultaneously in 30 equal steps and the coordinates of the beam locations

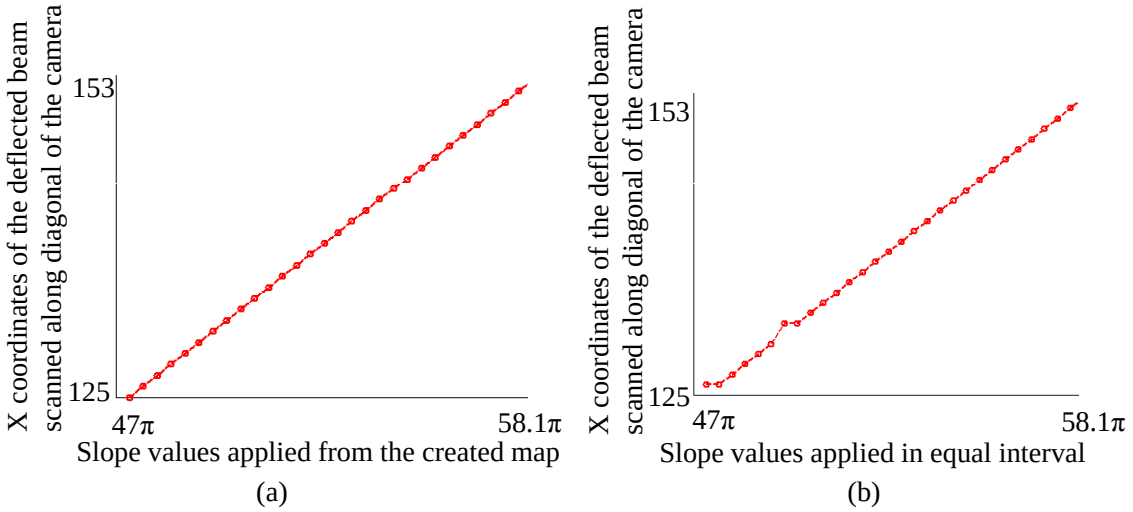

Figure 3.8: The plots of the X coordinates of the experimental beam locations deflected along the diagonal direction, when (a) the slope values are applied using the map, and (b) equally spaced slope values are applied.

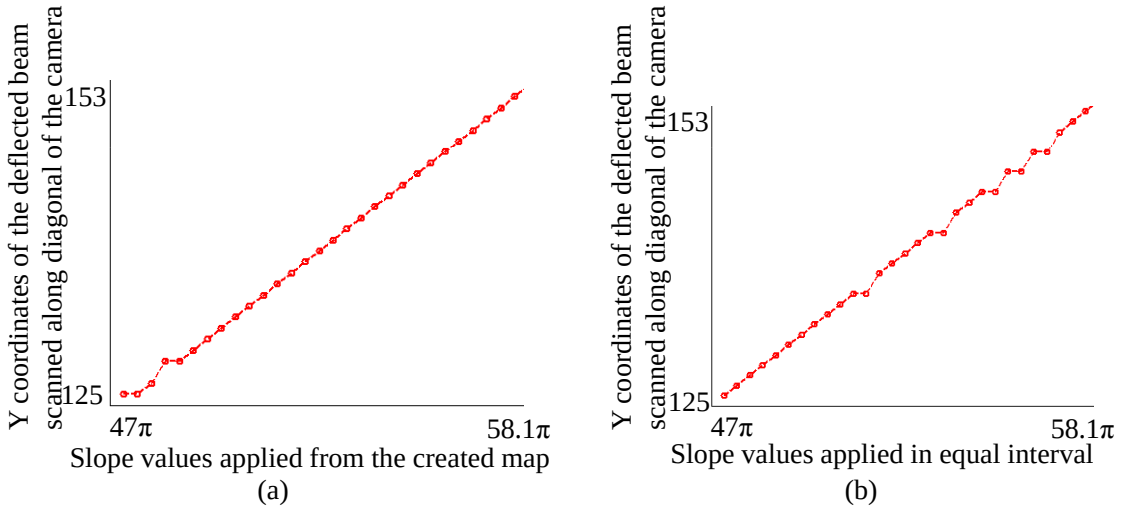

Figure 3.9: The plots of the Y coordinates of the experimental beam locations deflected along the diagonal direction, when (a) the slope values are applied using the map, and (b) equally spaced slope values are applied.

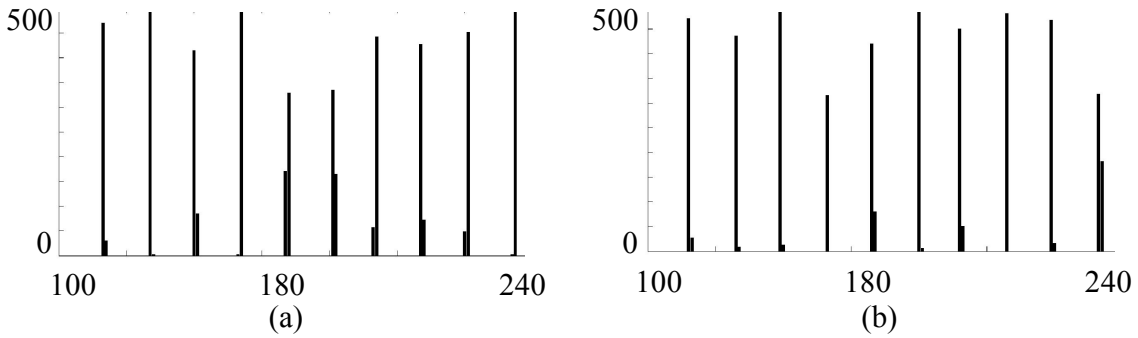

Figure 3.10: The bar diagrams show the number of times the peak intensity of the deflected beam is found at a particular camera pixel (represented by the horizontal axis), when (a) the beam is scanned along the x axis, and (b) the beam is scanned along the y axis.

on the camera are recorded. As seen in Figs. 3.9 (a) and (b) when the applied slopes are changed in equal steps the deflected beam does not move in equal steps.

3.6.3 Test for beam repeatability

As already mentioned, the scanning with a grating provides superior beam repeatability. This is because a particular grating profile corresponds to a specific beam location provided there are no other disturbances.

To test the repeatability of the binary hologram based scanning technique, we choose 10 slope values along x-axis varying from 40π, to 85π, in a step of 5π and applied them to holograms written on the LCSLM. With these applied slope values, the beam is allowed to scan along the x-axis for 500 times. After each scanning, the beam locations are recorded. The number of times the peak of the deflected beam is located at a given CCD pixel, is plotted as a bar diagram and is shown in Fig. 3.10 (a). From the bar diagram it is observed that the beam repeatability for various beam locations varies between 65.8% to 99.6%. For most of the beam locations the beam repeatability is found to be $\sim 80\%$. Only in a few cases the locations of the beam have been shifted by ± 1 pixel. This is again attributed to the vibration of the table over which the experiment is performed. The beam repeatability is also tested for beam deflection along the y axis. The corresponding bar diagram is shown in Fig. 3.10 (b). The beam repeatability in this case is found to vary between 63.6% to 97.6%. The superior beam repeatability by the scanning mechanism is also tested by scanning the beam along the diagonal direction.

3.7 Conclusion

In this chapter we have investigated laser beam scanning with a binary amplitude hologram implemented using an LCSLM. We have developed a theoretical expression to predict the deflection angle for a given binary hologram written on the LCSLM. It is demonstrated that the experimentally found beam locations agree well with the theoretically predicted beam locations. The theoretical expression is used to create a map between the applied slope values and the corresponding beam locations. The map can be used to realize equal step beam scanning along horizontal, vertical and diagonal directions. The experimental results demonstrate the utility of the proposed map. We also performed experiments to demonstrate superior beam repeatability by the binary hologram based beam scanning mechanism.

Chapter 4

Optical sectioning microscope with a binary hologram based beam scanning

4.1 Introduction

As discussed in the previous chapter, when a laser beam is incident on a binary hologram it can result in a diffracted beam traveling in a desired direction. In this chapter development of an optical sectioning microscope is described where the beam scanning is performed with the help of binary diffraction holograms. The binary holograms are displayed on a liquid crystal spatial light modulator. For the incident laser beam the binary holograms act as diffraction gratings. We have implemented optical sectioning microscopes using two types of liquid crystal spatial light modulators, namely, the nematic liquid crystal spatial light modulator and the the ferroelectric liquid crystal spatial light modulator.This chapter also presents some preliminary experimental results using the two types of optical sectioning microscopes.

4.2 Advantages of the binary hologram based beam scanning microscopes

The laser scanning confocal microscope (LSCM) is a popular optical sectioning microscope that finds applications in various fields of science. In an LSCM the scanning

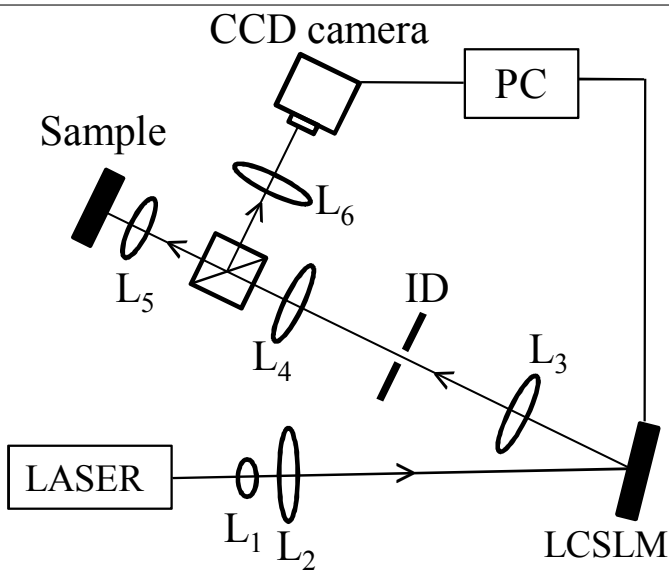

Figure 4.1: The experimental arrangement for the optical sectioning microscope with a nematic LCSLM.

of the illumination beam is usually performed by a galvanometer mirror scanner. As mentioned previously in this thesis, the beam scanning based on dynamic binary hologram has several advantages over the conventional scanning mechanism such as galvanometer mirror scanner. The hologram displayed on a pixellated device such as an LCSLM is invariant of time, i.e. the exact hologram can be displayed at different instants of time. Thus, such a beam scanner can provide superior beam repeatability compared to mechanical scanners. The laser beam steering with a grating on liquid crystal display is found to be extremely accurate, provided other mechanical disturbances are removed [77].

For better imaging performance, the galvo scanner unit used to scan the illumination beam in a scanning optical microscope should have a 4f relay system in between the two mirrors. These additional lenses make the system bulky and moreover alignment of the lenses is a tedious job. The proposed scanning mechanism, based on binary diffraction holograms, does not require such 4f relay system, thereby not compromising on the imaging performance. In the proposed scheme the illumination beam can be scanned over a rectangular area by displaying a sequence of appropriate binary holograms on the LCSLM. The technique employed here not only scans the illumination beam but also can describe the wavefront of the illumination beam. This facilitates describing the wavefront of the illumination beam on a pixel to pixel basis, a facility not available in conventional confocal microscopes.

4.3 Optical sectioning microscope using a nematic LCSLM

4.3.1 Experimental arrangement

The arrangement of the optical sectioning microscope [78] is shown in Fig. 4.1. A laser beam (λ = 633 nm) from a He-Ne laser source is expanded and collimated using the two lenses L_1 and L_2. The collimated beam is then incident on a reflective liquid crystal spatial light modulator comprising nematic liquid crystal cells. The LCSLM has a pixel pitch equal to 20 μm×20 μm. Binary holograms computed using a LABVIEW program running in a computer are sent to the display panel of the LCSLM as standard video signals. A snapshot of the front panel of the program is shown in Fig. 4.2. The light diffracted by the LCSLM due to the hologram displayed is focused by a lens L_3. At the focal plane of the lens L_3 an iris diaphragm (ID) is placed so that it only transmits the +1 diffraction order and other orders are blocked. The transmitted beam is then collimated using another lens L_4 and allowed to pass through a non-polarizing beam splitter (BS). The beam after passing through the beam splitter is focused by the lens L_5 on the sample plane. Thus the lens L_5 serves as the objective lens for the proposed microscope setup. The scattered or reflected light from the sample is again collected by the objective lens and a part of the light is reflected by the beam splitter perpendicular to the original path. The reflected part is focused by another lens L_6 on a CCD camera. The focal length of the lens L_6 is chosen in such a way that the corresponding Airy disc in the camera plane contains sufficient number of pixels, so that in comparison to the size of the Airy disc, the pixel of the camera can be approximated to be a point. This is worth mentioning here that the two pairs of lenses L_3, L_4 and L_5, L_6 form two 4f relay systems. The LCSLM plane is conjugate to the entrance pupil of the objective lens due to the pair L_3, L_4 and the sample plane is conjugate to the plane of the detector due to the pair L_5, L_6. We have chosen focal lengths of L_1 = 0.75 cm, L_2 = 12 cm, L_3 = 30 cm, L_4 = 10 cm, L_5 = 10 cm and L_6 = 15 cm. The diameter of the illumination beam at the entrance pupil of the lens L_5 is 3mm. The CCD camera has a pixel resolution of 1024×768 pixels and each pixel has a size equal to 4.65 μm×4.65 μm. When a sequence of appropriate holograms are displayed on the LCSLM the illumination spot on the sample plane describes a rectangular area. As the sample plane is imaged

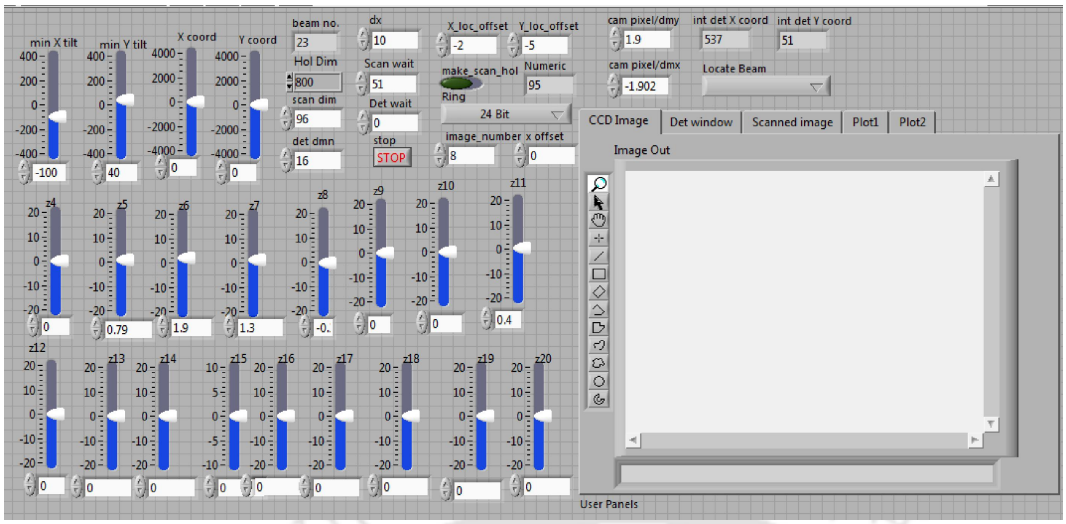

Figure 4.2: A snapshot of the front panel of the LABVIEW program.

onto the detector plane, the image of the illumination spot describes a rectangular area in the detector plane as well. However, the size of the rectangle on the detector plane will depend on the magnification of the lens system. It is useful to have an optical system such that the rectangle in image plane covers the maximum area of the CCD plane. Binary holograms are computed over a circular area of diameter consisting of 400 LCSLM pixels (diameter of the hologram=8mm), which are then written onto the LCSLM panel.

4.3.2 Detection mechanism in the microscope

In a conventional confocal microscope, as the illumination spot scans the sample plane, the light from the sample plane is collected by the same objective lens and is then descanned by the scanner unit. Thus, due to the optical arrangement there is no lateral movement of the beam in the detector plane. The de scanned light is then focused on the detector. The ray diagram for such a scanning microscope in shown in Fig. 4.3. In contrast to this mechanism, in the proposed microscope the reflected light from the sample plane is not de scanned by the scanner unit. Thus the focal spot on the sample plane and its image on the detector plane describes a rectangular area. Different positions of the illumination beam on the sample plane correspond to different positions on the detector plane as shown in Fig. 4.4. Here a CCD camera comprising a two dimensional array of sensor pixels is used as the detector. To collect the signal for each position of the beam on the sample plane

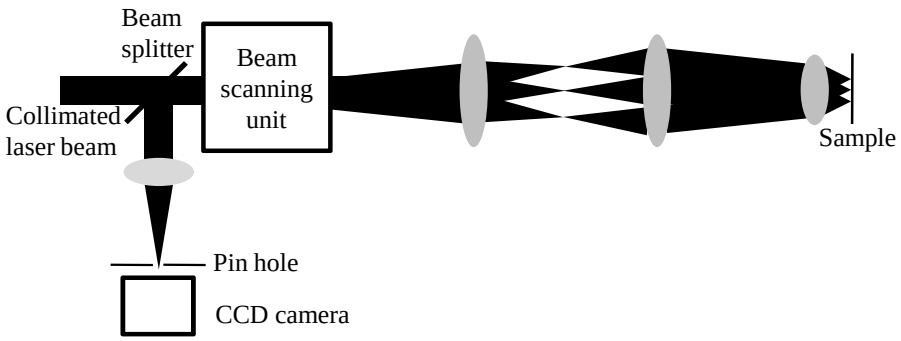

Figure 4.3: The ray diagram of detection mechanism in a conventional scanning microscope.

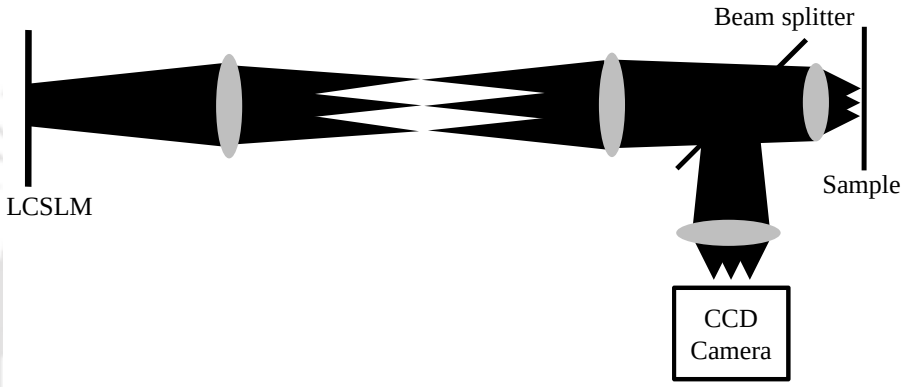

Figure 4.4: The ray diagram of detection mechanism in the proposed microscope. Only the deflection of the illumination beam by the LCSLM is shown.

when beam scans the sample plane, a rectangular area around the image of the illumination spot is created. For each position of the beam, the detector can receive only the signal that are within the rectangular area. This rectangular area is termed the as detector area and its size, referred to as detector dimension, can be controlled in real time with the help of the LABVIEW program. As the illumination spot scans the sample plane, the same LABVIEW program moves the detector area to the expected location of the image of the illumination spot, as shown in Fig. 4.5. The detector dimension which is equal to the length of each side of the detector area, are taken as 8, 16, 32 and 64 CCD pixels. It is worth mentioning here that the minimum detector dimension is kept as 8 pixels, since upto this size of the detector, the present arrangement can give reasonable signal to noise ratio.

The arrangment to implement of a confocal pinhole with a CCD camera as described above can also be called synthetic pinhole. Similar scheme has already been used in a number of confocal systems as available in standard literature [79, 80].

(a) (b)

Figure 4.5: Synchronized movement of the detector area in the camera plane. (a) The first position of the beam on the camera surrounded by the detector area, and (b) another position of the beam on the camera again surrounded by the detector area.

4.3.3 Resolution of the microscope

The resolution of the microscope depends on the NA of the lens L_5. If the light reflected from the sample plane is considered to be incoherent, the lateral intensity PSF as described in the chapter 1 has the form

$$I(v) = \left(\frac{2J_1(v)}{v}\right)^4 \tag{4.1}$$

where J_1 is the Bessel function of the first kind and first order and v is the normalized optical coordinate on the sample plane, given by $v = kr\sin\alpha$. Here $\sin\alpha$ is the NA of the lens L_5 and r is the radial coordinate in the sample plane. The lateral resolution of the microscope is given by the full width at half maximum (FWHM) of the $I(v)$ versus v plot which is found to be v_{FWHM}=2.34. The value of r_{FWHM} corresponding to v_{FWHM} value is found by making the substitution of k and $\sin\alpha$ in the expression of v. For our experimental arrangement, $k = 9.93 \times 10^6 m^{-1}$ and $\sin\alpha = 0.015$ giving r_{FWHM}=15.72μm. We now consider a hologram of dimension equal to N pixels described on the LCSLM plane. If f is the focal length of the lens L_5, M is the lateral magnification between the LCSLM plane and the pupil of L_5, and d is the LCSLM pixel pitch, then with the assumption that the displacement of the illumination spot is a linear function of x and y tilts in the hologram (i.e., m_x and m_y) and the aliasing effect is minimum, the minimum separation (PX_{min}) between the two positions of the illumination spot in the sample plane is given as

$$PX_{min} = \frac{f\lambda}{2MNd}, \tag{4.2}$$

In order to achieve the resolution limit r_{FWHM} with the proposed microscope, PX_{min} has to be at least half of the resolution limit.

The axial intensity PSF of the microscope as described in chapter 1 is given by [6]

$$I(u) = \left(\frac{\sin(u/4)}{u/4}\right)^4 \tag{4.3}$$

where u is the normalized optical coordinate along the optic axis and is expressed as $u = 4kz\sin^2(\alpha/2)$ with z as the axial coordinate in the sample volume. Likewise the lateral resolution, the axial resolution of the microscope is calculated from the FWHM of the $I(u)$ versus u plot. For the proposed setup the resolution is found to be u_{FWHM}=8.02. Corresponding to this value of u, the value of z is z_{FWHM}=3.6 mm.

4.4 Experimental results and discussion

4.4.1 Active aberration correction

As discussed in section 4.2, the computer generated holography technique employed here can be used to correct the illumination beam from aberrations. In our experimental setup the illumination beam was found to be aberrated primarily due to the LCSLM itself and partly due to other optics in the beam path. To measure and hence correct the illumination beam for aberrations present prior to placing the sample, the CCD camera is placed in the focal plane of L_5. The PSF is recorded and its image is shown in Fig. 4.6 (a). It is evident from the figure that the PSF is aberrated. To correct this beam a helical phase profile is added to the illumination beam holographically and the amount of aberration is measured using the sensitivity of singular light beams [81]. The aberration present in the illumination beam in terms of single index Zernike mode [53] is found to be $1.6Z_4 - 2.9Z_5 - 0.4Z_6 - 0.4Z_7 - 0.4Z_8 + 0.4Z_{14}$. The PSF after incorporating the corrections is recorded and is shown in Fig. 4.6 (b) which seems to be close to an Airy pattern

4.4.2 Optical sectioning performance

The optical sectioning capability of the microscope can be demonstrated by moving a plane mirror axially near the focus of the lens L_5 and observing the total intensity of the focal spot on the CCD camera within a given detector area. The total detector signal is recorded for detector dimensions equal to 8, 16, 32, and 64 pixels

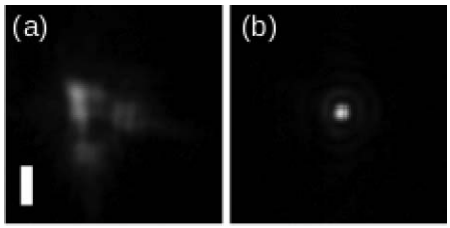

Figure 4.6: The illumination beam PSF (a) before aberration correction, and (b) after aberration correction. The scale bar in Fig. (a) has length equal to 97μm.

for different positions of the mirror on the both the sides of the focal point of L_5. The detector signal as a function of the position of the mirror is also simulated considering a point detector for the same optical configuration. Figure 4.7 shows the plot of the simulated detector signal for a point detector and experimental detector signals as a function of the mirror position relative to the focus of L_5 and in a direction away form L_5 (since the plot is symmetric on both sides of the focus, behaviour only in one half is shown in the plot). From the plot it is observed that as the size of the detector dimension gets smaller, the system rejects more out of focus light compared to the larger detector dimension. The plot also shows that the FWHM of the plot corresponding to the detector dimension equal to 8 pixels is found to be approximately 4.4mm. This value is approximately equal to the axial resolution of the microscope as suggested by the theory discussed in Sec. 4.3 which also corresponds to the simulated plot for a point detector. However the small difference between the theoretical and experimental value can be attributed to the fact that the detector dimension used here is equal to 8 pixels and is still not a perfect detector as demanded by theory for optimum resolution performance by the microscope. Further it is noticed in Fig. 4.7 that the experimental plot appears to be decaying and does not have a flat top near the focus unlike the simulated curve. This is due to the limited number of experimental data points used to construct the experimental plot.

4.4.3 Imaging performance using reflected light

For testing the imaging performance of the proposed setup, a Fresnel lens is used as the sample. A white paper is placed at the back of the Fresnel lens, at a distance of about 2 mm behind its front surface, to increase the amount of background light. A set of appropriately computed holograms are then displayed on the LCSLM

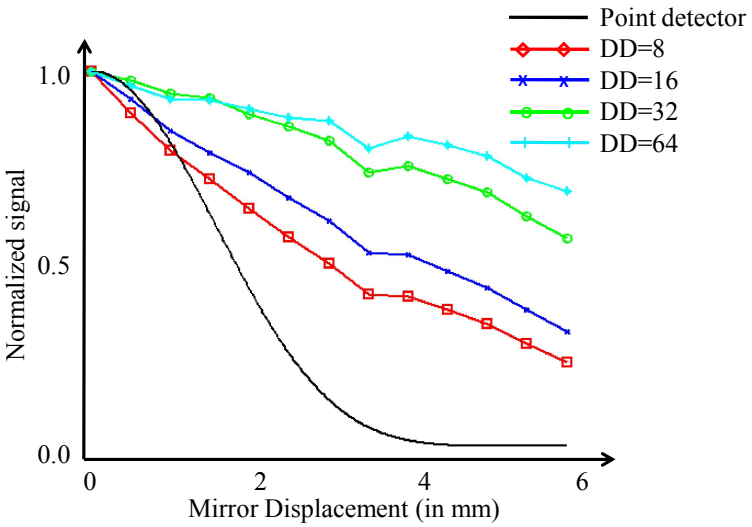

Figure 4.7: Plots of normalized detector signals versus mirror displacement measured relative to the focal plane in a direction away from L_5 for a point detector (theoretical) and for detector dimensions DD= 8, 16, 32, and 64 pixels (experimental).

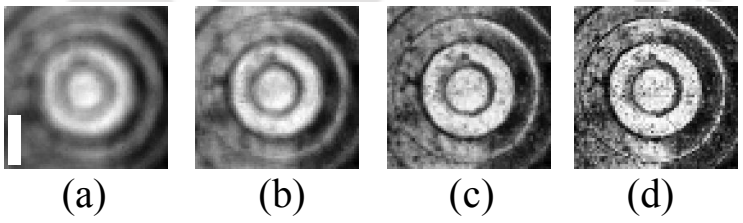

Figure 4.8: Images using the scattered light from a Fresnel lens using detector dimensions equal to (a) 64, (b) 32, (c) 16, and (d) 8 pixels. The length scale bar in figure (a) has length equal to 566 μm.

panel. As a result the illumination spot goes to 64×64 locations of the sample plane describing an area 1.7 mm×1.7 mm around the center of the Fresnel lens. Images of the sample are taken by collecting the scattered light using detector dimensions equal to 8, 16, 32 and 64 pixels and are shown in Fig. 4.8. As seen from the recorded images of the lens, the amount of background light reaching the detector gets reduced decrease in detector dimension. This gives rise to optically sectioned images of the sample relative to images recorded with larger detector dimensions. It is noticed in Fig. 4.8 that as the detector dimension gets smaller there is significant enhancement in image resolution and the enhancement appears more significant than that of the sectioning strength as depicted by Fig. 4.7. This is attributed to the fact that enhancement in the image resolution as the detector dimension gets smaller is due to both optical sectioning and enhancement in lateral resolution.

4.5 Optical sectioning microscope with an FLCSLM

In the previous section we describe the implementation of an optical sectioning microscope that uses a nematic LCSLM (NLCSLM) to write binary holograms in order to scan the illumination beam. An NLCSLM can display up to three binary holograms per colored image. Thus considering a 60 Hz refresh rate video signal, the NLCSLM can display upto 180 binary holograms in one second. Consequently the proposed microscope using the NLCSLM has a slow frame rate. In this section we employ an FLCSLM to implement binary hologram based beam scanning. In comparison to an NLCSLM, an FLCSLM cells have a quick response time [65] and it can display up to 24 binary holograms per colored image. This leads to an increase in the scanning speed at least by 8 times compared to an NLCSLM based beam scanner. Here a commercially available FLCSLM (SXGA-R3, ForthDD) device that contains 1280×1024 liquid crystal (LC) cell in its display panel is used. Such an SLM can display up to 85 RGB images per second using a time dithering technique. For each incoming colored image the device displays the constituent 24 single bit images in a sequential manner. Thus the device can display 24×85=2040 number of single bit images in one second. Each of the single bit images is used to describe a binary phase hologram to deflect the illumination beam in a user defined direction. This scanner is then employed to construct an optical sectioning microscope in a similar fashion as described earlier in this chapter.

4.5.1 Synchronization of the detector and the FLCSLM display

Each RGB image received by the FLCSLM contains 24 single bit frames among which the first 8 frames represent red color, the second 8 frames represent green color and the third 8 frames represent blue color. Fig. 4.9 shows such frames, R_0, R_1, R_2, ..., R_7 , G_0, G_1, G_2, ..., G_7, and B_0, B_1, B_2, ..., B_7 representing the red, green and blue color frames respectively. Unlike the NLCSLM, DC field is applied across the LC cells of the FLCSLM. One of the requirement of the FLCSLM is that display of each single bit image has to be followed by the display of its negative counter part to prevent any potential damage to the LC molecules. The FLCSLM

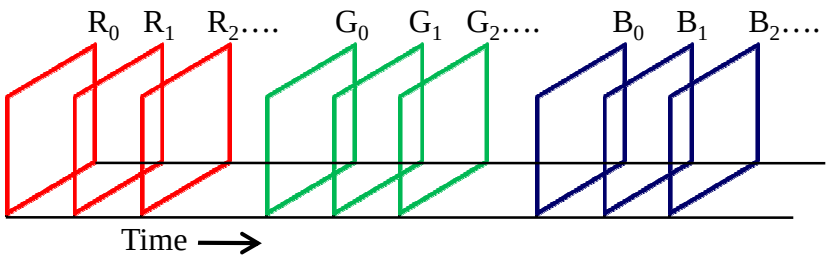

Figure 4.9: Sequential display of the 24 bit planes in an FLCSLM display panel.

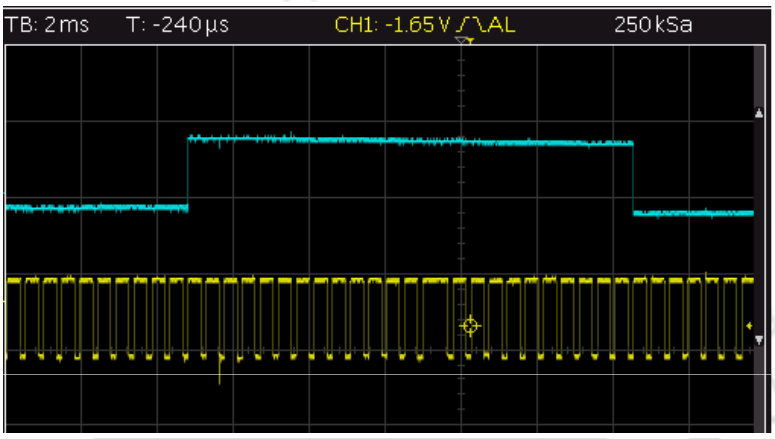

Figure 4.10: Snapshot of the oscilloscope panel showing the plot of synchronization signal from the FLCSLM (below) and the plot of camera trigger signal (above).

control box provides an electrical signal that goes high when a hologram is in display and goes low when its negative counter part is displayed. The electrical signal from the FLCSLM control box becomes high or low in synchronization with the display of each of the positive or negative single bit images. Such a signal (the bottom plot) is shown in Fig. 4.10 which is the snapshot of a digital oscilloscope that receives the synchronization signal form the FLCSLM in channel 1. The plot shows that the positive frame is displayed for a duration of ~ 360 μs and its negative counter part is displayed for a duration of ~ 140 μs on an average. A PIC18F2550 microchip based board receives the synchronization signal from the FLCSLM and generates a camera trigger signal as shown in the top plot of Fig. 4.10. This trigger signal, received in channel 2, remains high during the display of all the 24 frames of a given RGB image. This signal is then used to trigger the CCD camera so that the CCD receives light only when a given RGB image is being displayed in the FLCSLM panel.

We again employ the same computer generated holography technique to generate

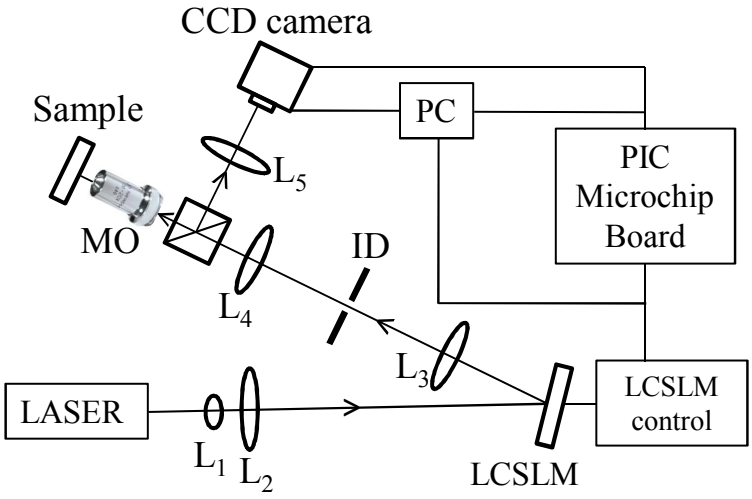

Figure 4.11: Experimental arrangement for the microscope with an FLCSLM based beam scanning.

binary holograms which are written on the FLCSLM display panel. The panel acts as a diffraction grating when it is illuminated by a collimated laser beam. The display panel introduces a phase modulation of 0 or π to the incoming beam depending on the binary value of the DC field applied across the corresponding LC cell.

4.5.2 The experimental arrangement

The schematic of the FLCSLM based beam scanning microscope [82] is shown in Fig. 4.11. The laser beam from a DPSS laser of wavelength 532 nm is expanded and collimated by the two lenses L_1 and L_2. The collimated beam is then allowed to fall on the display panel of the FLCSLM. A LABVIEW program running on a PC computes sets of 24 single bit holograms in the form of RGB images. Such an RGB image consisting of 24 binary hologram is shown in Fig. 4.12. These images are then sent to the display panel of the FLCSLM as video signal from the PC. The beam diffracted by the FLCSLM is focused by the lens L_3. An iris diaphragm (ID) is kept in the focal plane of L_3 so that it transmits only the +1 order and other orders are blocked. Another lens L_4 recollimates the +1 order followed by focusing of the beam by a microscope objective MO on the sample plane to be imaged. The light reflected by the sample is received by the same MO and is reflected by a 50-50 beam splitter towards the lens L_5. The lens then focus the beam on a CCD camera plane. The microchip based control board sends a trigger signal (similar to the one shown in Fig. 4.10) to the CCD camera having 20 pulses per second. Each pulse

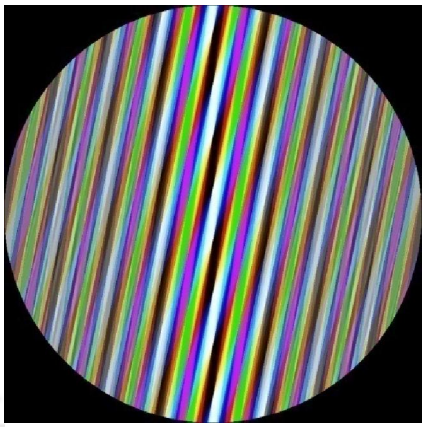

Figure 4.12: An RGB image (800 pixel×800 pixel) comprising 24 binary holograms sending the diffracted beams to equal number of equally spaced locations.

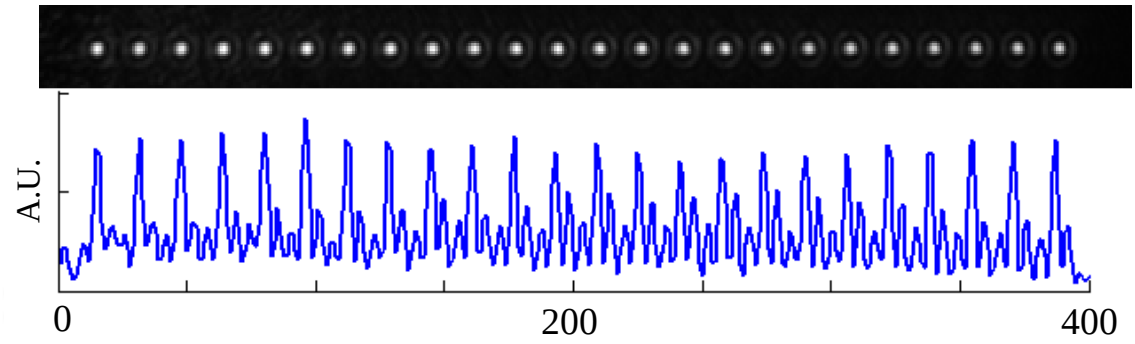

Figure 4.13: CCD image of 24 focal spots due to the display of a single RGB image in the display panel (top) and a line plot joining centres of the focal spots (bottom). The light intensity is expressed in arbitrary unit (A.U.).

exposes the camera to the light coming from the sample plane for the duration of 24 holograms are being displayed on the FLCSLM panel.

Before placing the sample in the focal plane of the MO, a plane mirror is placed to record the +1 order focal spot by the CCD camera for each of the 24 single bit images. The RGB image displayed deflects the +1 order beam to 24 number of uniformly spaced locations. Fig. 4.13 (top) shows the 24 focal spots recorded in a single image frame of the CCD camera. The line plot joining the central points of the focal spot is shown in the bottom of Fig. 4.13. The plot suggests that the focal spots are equally spaced. To record a rectangular area of a sample with such focal spots, a sequence of RGB images are sent to the FLCSLM panel. The RGB images are so constructed such that after displaying a given number of RGB images, the +1 order focal spots describe a rectangular grid in the focal plane of the MO. In

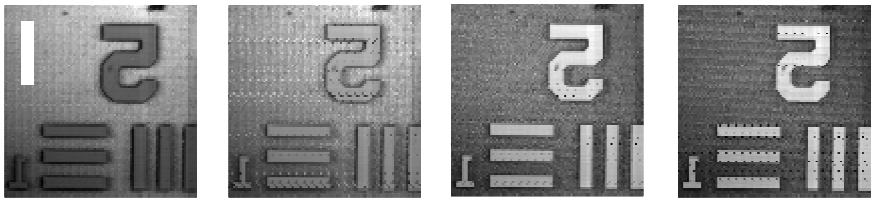

Figure 4.14: Beam scanning microscope images (size=96 pixel×96 pixels, MO is a 10× Olympus lens of NA=0.3) of a USAF resolution test target, using detector window of dimension equal to (a) 16 pixels, (b) 12 pixels, (c) 8 pixels, and (d) 6 pixels. The dimension of the scale bar at the top left corner in (a) is 78 μm.

order to avoid any overlap between two consecutive focal spots captured in a single CCD image, each RGB image is made to generate a sparse array of +1 order spots. The signal for each position of the beam is detected as described in Sec. 4.4.3.

4.5.3 Results and discussion

To test the imaging capability of the microscope, a USAF 1951 resolution test target is used as the sample. To enhance the background light a plane mirror is placed behind the sample plane. With this arrangement, images of the test target is recorded with detector dimension equal to 16 pixels, 12 pixels, 8 pixels and 6 pixels. The recorded images are shown in Fig. 4.14 which indicates that as the detector window dimension is reduced the capability of the microscope to reject background light is enhanced. However, due to the presence of the mirror behind, there appears a contrast reversal in the images when the detector dimension becomes large.

4.6 Conclusion

An optical sectioning microscope with a binary hologram based beam scanning mechanism is developed. The binary hologram is implemented on the display panel of an NLCSLM as well as on an FLCSLM. The beam scanning mechanism implemented here does not require any scanner involving mechanical movement. Further it removes the requirement of a 4f relay system that needs to be placed between the two scan mirrors in the case of a galvo mirror scanner. The scanning mechanism can provide superior beam positioning compared to the conventional scanner. Moreover since the beam scanning is based on binary hologram written on a LC cell, the

scanning provides better beam repeatability.

We have described detailed experimental arrangement for the two versions of the microscope and presented preliminary experimental results. The experimental results clearly demonstrate the optical sectioning capability of the two proposed systems. The proposed microscope setup works in the reflection mode; however, the same can be modified, such as by replacement of the camera with another one having sensitivity in the longer wavelength region and the replacemnt of the cube beam splitter, with a dichroic beam splitter to work in the fluorescence mode.

Chapter 5

Scanning optical microscope with dynamic illumination beam intensity

5.1 Introduction

As discussed in chapter 1, one of the limitations of an optical sectioning microscope is the illumination beam intensity that remains constant over the entire image frame. It becomes an issue when imaging samples having both low and high regions of reflectivity or transmissivity (denoted as R/T) in the case of microscopes working in the reflection or transmission mode, respectively. There are a number of biological as well as non biological samples where the R/T profile is not uniform [9]. Since the amount of signal collected from each position of the sample plane depends on the reflectivity or transmissivity at that location, the signal collected by the detector from the region of low R/T is weak compared to that from the high R/T region. As a result of this, the recorded image will have poor signal to noise ratio (SNR) in the less R/T region compared to the higher R/T region, which may lead to loss of information in the image in the respective regions [32]. One has the option of enhancing the signal level from the region of low R/T by increasing the intensity of the illumination beam. However, this will also enhance the signal received by the detector from the region with high R/T of the sample. Thus one can not increase the intensity of the illumination beam arbitrarily since the signals from the region of high R/T may saturate the detector. Therefore, to make the signal to noise ratio

more uniform there is a need to vary the intensity of the illumination beam , within an image frame, unlike the dynamic illumination using laser spackle [83] , so that it has low intensity in the region of high R/T and high intensity in the region of low R/T.

This chapter describes the design and development of a laser scanning confocal microscope that incorporates variable intensity in the illumination beam to record images with uniform SNR of samples having both low and high R/T regions. The chapter begins with the description of achieving the variation in the illumination beam intensity using the property of binary diffraction holograms. We then describe a simple scheme to implement uniform signal to noise ratio for samples with non uniform R/T profile and show numerical simulation results using the same scheme. This is followed by experimental implementation of the proposed scheme to achieve uniform SNR in the image.

5.2 Control over the intensity of the illumination beam using LCSLM

As discussed in chapter 2, the light efficiency in the beams diffracted by a binary grating depends on the ratio of the width of the transparent portion to the width of the full cycle of the grating. This ratio is known as the duty cycle of the grating. Since in the present work the +1 order beam is taken as the illumination beam of the proposed microscope, it is possible to vary its intensity on a pixel to pixel basis by varying the duty cycle in the binary hologram. We use a LABVIEW program to write binary holograms on the LCSLM that facilitates the user to have dynamic control over the duty cycle of the binary hologram.

Let I $(0 \leq I \leq 1)$ be the desired intensity of the illumination beam for a particular location of the beam on the sample plane. To generate the beam intensity I we describe the pixel value of the LCSLM as

$$p(x,y) = \begin{cases} 1 & \text{if } \cos\Phi(x,y) \geq \cos(\sin^{-1}(I)) \\ 0 & \text{if } \cos\Phi(x,y) < \cos(\sin^{-1}(I)) \end{cases} \tag{5.1}$$

Now, we consider a sample to be imaged that has non uniform R/T. To vary the intensity of the illumination beam on a pixel to pixel basis, first an image of the sample is recorded with an illumination beam intensity kept constant throughout

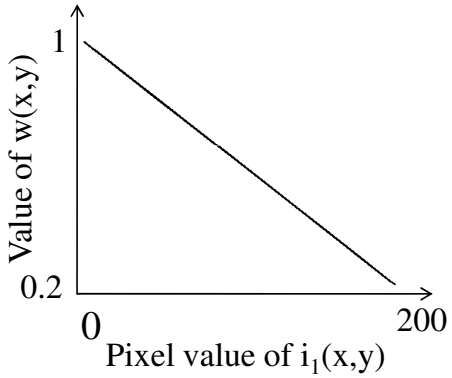

Figure 5.1: Plot of $w(x, y)$ against $i_1(x, y)$

the image plane. This image is used to get the information about the reflectivity or transmissivity profile of the sample. The same LABVIEW program running in the PC reads the recorded image and identifies the region of weak reflectivity or transmissivity. Let $i_1(x, y)$ represents the pixel values in the recorded image of the sample using the constant intensity illumination beam. We then introduce a weight function $w(x, y)$, that will decide the position dependent intensity of the illumination beam described by the R/T value at the corresponding location, as

$$w(x,y) = w_M \left[\frac{\frac{M-i_1(x,y)}{M-m} + \frac{w_m}{w_M - w_m}}{1 + \frac{w_m}{w_M - w_m}} \right] \tag{5.2}$$

where M and are m are maximum and minimum pixel values of the image $i_1(x, y)$. Further w_M and w_m are the weighted intensities for the pixels with the minimum R/T and the maximum R/T, respectively. The plot of $w(x, y)$ against the corresponding pixel value of i_1 is shown in Fig. 5.1 which shows that $w(x, y)$ varies linearly with i_1. The program then computes a sequence of holograms using the weight function $w(x, y)$ and displays them on the LCSLM. Thus a second image of the same sample is taken with $w(x, y)$ describing the weighted intensity on a pixel to pixel basis. The values of w_M and w_m are taken as 1 and 0.25 respectively. The minimum intensity value of the beam is assigned a non zero value so that during aquisition of the second image there is light received from the most reflective/transmittive region of the sample. The value of w_m can be altered depending upon the sample's transmittance/reflectance profile. Let the second image be $i_2(x, y)$, which is recorded with the modified set of holograms i.e., with variable or position dependent illumination beam intensity. The final image [84] of the sample with enhanced SNR is

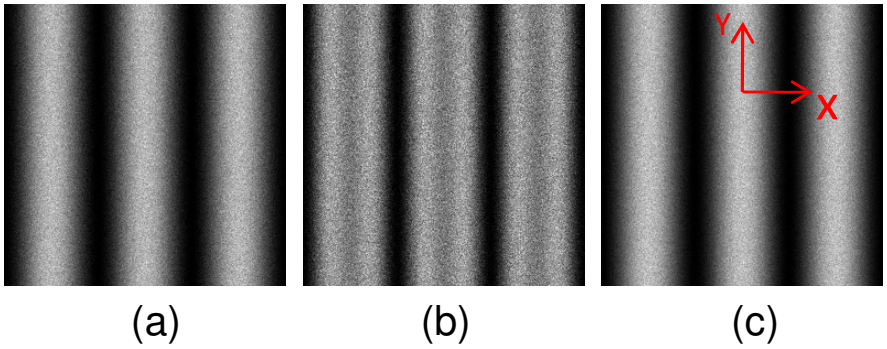

Figure 5.2: (a) Image with constant illumination beam intensity, (b) Image with variable illumination beam intensity, and (c) final image of the sample. Horizontal and vertical directions in the image are denoted as X and Y.

digitally constructed from the two recorded images using the relation

$$i_3 = \frac{i_1 + i_2}{1 + w} \tag{5.3}$$

Assuming an ideal imaging system with a target represented by $o(x, y)$ we can write $i_1(x, y) = o(x, y) \pm \delta_p(i_1(x, y))$, considering unit magnification. Here $\pm\delta_p()$ represents Poisson noise. Similarly $i_2(x, y) = o(x, y) * w(x, y) \pm \delta_p(i_2(x, y))$, so that

$$i_3(x, y) = o(x, y) \pm \frac{\delta_p(i_1(x, y)) + \delta_p(i_2(x, y))}{1 + w(x, y)} \tag{5.4}$$

It can be seen that $\frac{\delta_p(i_1(x,y))+\delta_p(i_2(x,y))}{1+w(x,y)} \leq \delta_p(i_1(x, y))$ in the regions with low R/T, contributing to superior SNR in the respective regions.

5.3 Numerical simulation results

The scheme described in the previous section has been implemented in a numerical simulation using MATLAB. The simulation work has been performed on a digitally constructed pattern having both high and low pixel values. It is well known that pixel values in an image recorded with any imaging device also contain noise that satisfy Poisson distribution [85]. Thus in order to be close to a real situation we have added Poisson noise to the image. This image with Poisson noise added (refered to as i_1) is shown in the Fig. 5.2 (a). From the image the weight function $w(x, y)$ is calculated as described in equation 5.2. The intensity of the illumination beam is then varied for different positions (x, y) in accordance with $w(x, y)$ so that the beam

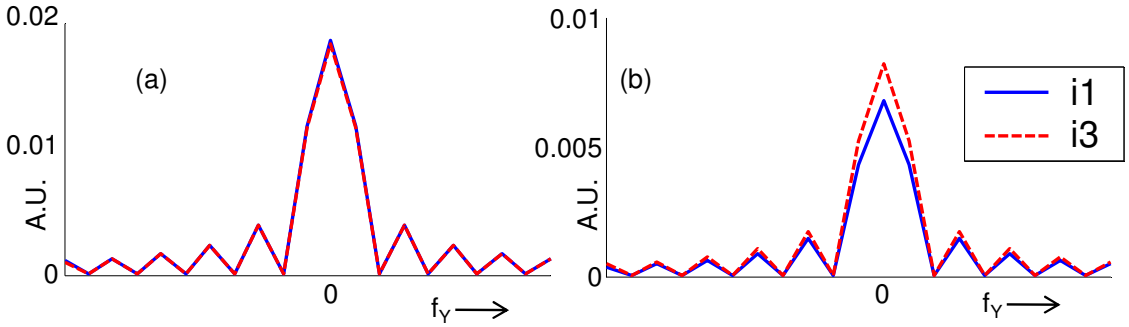

Figure 5.3: Line plots representing Fourier transforms along Y for the images in Fig. 5.2 (a) and Fig. 5.2 (c), considering only (a) high R/T regions, and (b) only low R/T regions. The horizontal axis corresponds to spatial frequency along Y and the vertical axis corresponds to strengths of the spatial frequency components, in arbitrary unit (A.U.), extracted from a normalized Fourier plane.

has the highest intensity in the region of low R/T (low pixel value of the target) and vice versa . Again, Poisson noise is added numerically to the second image and the image formed is named as i_2. This image is shown in Fig. 5.2 (b). The final image of the pattern is digitally constructed using the relation 5.3 and is shown in Fig. 5.2 (c).

In order to quantify the relative enhancement in the SNR in the image i_3 for low R/T regions of the target, we computed the spatial frequency spectrums of the high R/T regions or low R/T regions only for the images i_1 and i_3, by performing Fourier transform along Y (since the target does not have any spatial variation along Y). As seen in Fig. 5.3 (b), in the case of i_3 there is a significant enhnacement in zero spatial frequency component relative to i_1 for regions with low R/T. However, in the regions of high R/T the zero spatial frequency components in i_1 and i_3 have comparable strength. An increase in the strength of the zero spatial frequency component indicates a reduction in the noise level.

5.4 The experimental implementation

The experimental setup for the laser scanning microscope with programmable illumination beam intensity is shown in Fig. 5.4. Here, for the sake of easy implementation we have developed the scanning microscope in the transmission mode. The beam from a He-Ne laser (λ=633 nm) is expanded and collimated using two lenses L_1 and L_2. The beam is then allowed to incident on the LCSLM. A LABVIEW program

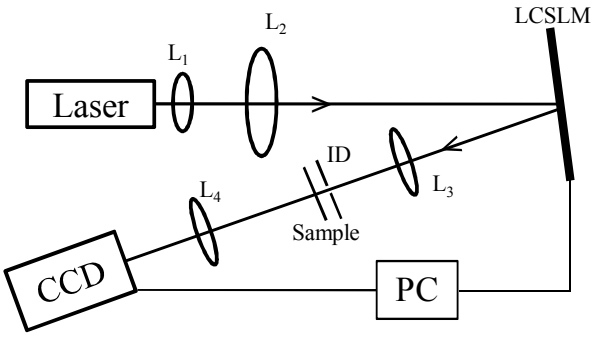

Figure 5.4: The experimental setup for the proposed scanning microscope in transmission mode.

running in a personal computer (PC) computes a binary hologram over a circular area of diameter equal to 14 mm over 700×700 pixels and is displayed on the LC-SLM display panel. As a result the beam gets diffracted by the hologram. The lens L_3 is placed at a distance equal to the focal length of the lens from the LCSLM display panel to collect the diffracted beams and focus them on the other side of the lens. The sample to be imaged is placed in the back focal plane of the lens L_3 and an iris diaphragm (ID) is placed just in front of the sample plane to allow only the +1 order beam to fall on the sample plane. The light transmitted through the sample is collected by a lens L_4 and is finally focused onto a CCD camera. A sequence of binary amplitude holograms is displayed on the LCSLM display panel such that illumination spot and its image on the detector plane describe two rectangular areas. To detect the signal for each position of the beam on the sample plane, again a rectangular area, defined already as the detector area, around the image of the illumination spot on the CCD plane is generated using the program. The LABVIEW program synchronizes movement of the rectangular area with the movement of the image of the illumination spot during the scanning of the beam over the sample plane. The signal collected within the area of the rectangle for each position of the beam on the sample plane is stored by the program. At the end of the scanning, the collected signals from each position of the sample is used to construct an electronic image of the scanned area.

5.5 Experimental results and discussion

The sample whose image is to be recorded is to be placed in the focal plane of the lens L_3. However, the quality of the illumination beam, before placing the sample,

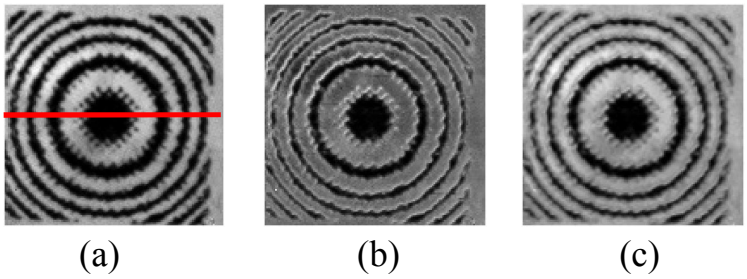

Figure 5.5: Experimentally obtained images (a) i_1, (b) i_2, and (c) the final image of the sample, i_3.

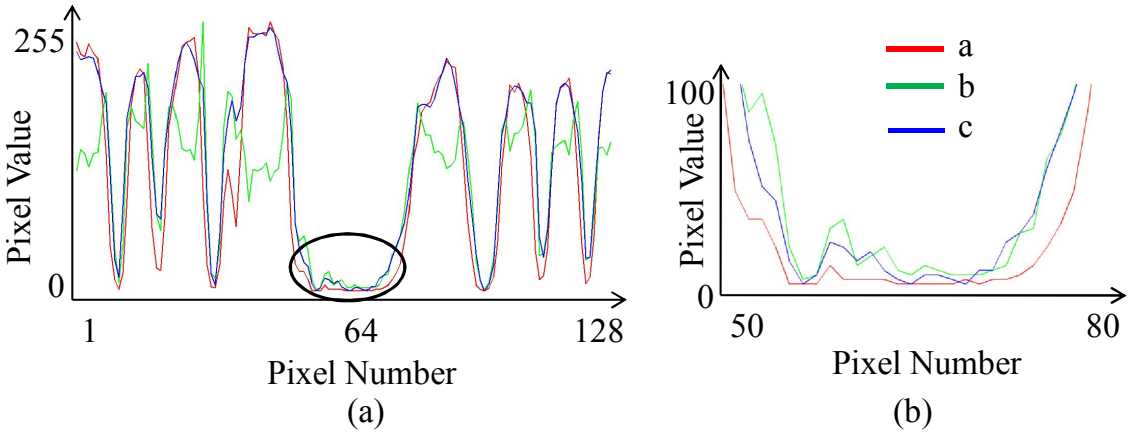

Figure 5.6: Line plots of the images (a) i_1, i_2 and i_3 along the line shown in Fig. 5.5 (a), and (b) zoomed line plots corresponding to the encircled area in (a).

is checked and accordingly aberration correction is performed, as described in the chapter 4. The amount of aberrations in this case in terms of the single index Zernike mode [53] is estimated and found to be $3.4Z_5$+$0.6Z_6$+$0.5Z_7$+ $0.4Z_8$-$0.2Z_9$+$0.3Z_{10}$-$0.7Z_{11}$. As stated above it is necessary to synchronize the movement of the detector with the image of the illumination on the CCD. For this, the movement of the beam on the CCD is calibrated with respect to the tilt values (m_x and m_y) of the hologram. The illumination spot moves over 128×128 discrete positions describing an area equal to $1cm \times 1cm$ on the sample plane. The detector dimension is kept equal to 16 pixels to optimize the amount of signal collected by the detector. An image $i_1(x, y)$ of the sample is recorded with a moderate illumination beam intensity that remains constant over the entire image frame. The image of the scanned area of the sample is shown in Fig. 5.5 (a). From this image the weight function $w(x, y)$ is calculated using the equation 5.2. This weight funcition is then utilized to compute appropriate binary holograms which are displayed on the LCSLM to achieve position dependent

illumination beam intensity over the sample plane. During the second scanning the beam will repeat the same beam locations as in the case of image $i_1(x, y)$ since the scanning mechanism provides excellent beam repeatability as described in chapter 3. With the modified set of the holograms, another image $i_2(x, y)$ of the same sample is recoded without disturbing the setup. The image recorded with the variable intensity illumination beam is shown in Fig. 5.5 (b). The final image is constructed digitally using the relation 5.3 and is shown in Fig. 5.5 (c).

In order to investigate the relative enhancement of signal level in i_3 for low R/T regions of the target, we plotted the intensities along the lines shown for the images in Fig. 5.5 (a), (b) and (c) and are shown in Fig. 5.6 (a). It is noticed in a zoomed portion of the plot shown in Fig. 5.6 (b) that the signal level in the low R/T region is enhanced in the image i_3 relative to the image i_1. It is to be noted that the target is a pattern printed on a transparent sheet, thus the central portion of the target is not uniformly dark and contains a few scattered dark dots. In fact a few such dark dots are more clearly noticed in the image i_3 than in i_1 as evident from the line plot shown in Fig. 5.6 (b).

5.6 Conclusion

In this chapter the implementation of a scanning microscope with a variable illumination beam intensity is described. Both the scanning and the programmable control over the illumination beam intensity are achieved using binary holograms written over a computer controlled LCSLM. The microscope described here is in the transmission mode; however, the same can work in the reflection or fluorescence mode as well. Unlike the conventional scanning microscope the proposed microscope can have relatively high illumination beam intensity in the regions of the sample plane with weak reflectivity or transmissivity. The proposed system can thus increase the overall SNR especially in the region from where the signals received are weak. The experimental as well as the simulated results show enhancement of the signal to noise ratio in the weakly transmissive regions.

Chapter 6

Scanning optical microscope with dynamic control over the illumination beam phase profile

6.1 Introduction

As described in chapter 1, in a conventional laser scanning confocal microscope the phase profile of the illumination beam remains constant over an image frame. This may become an issue when imaging a sample that introduces spatially varying aberrations into the illumination beam. The image recorded with a conventional laser scanning microscope for such samples may not give correct information of the sample. To faithfully record the image of a sample introducing variable aberration into the illumination beam there is a need to have a position dependant phase profile of the illumination beam that can compensate for the amount of aberrations at each position of the beam on the sample plane, which is introduced by the sample.

In this chapter we describe the design and development of an optical sectioning microscope that has the facility to vary the illumination beam phase profile on a pixel to pixel basis, to compensate for the aberrations introduced by the sample itself. The first section of the chapter describes theoretical considerations in correcting the illumination beam containing certain aberrations. This is followed by a description of the dynamic aberration correction mechanism using the property of binary diffraction holograms. It then describes the experimental arrangement for the proposed microscope and the experimental results obtained using the microscope.

6.2 Theoretical considerations

In principle, one may predict the presence or absence of aberration in the illumination beam by looking at the intensity distribution at the focus. When there is no aberration present in the beam the focal spot intensity is described by an Airy pattern, in the low NA regime. Any deviation of the focal spot from an ideal Airy pattern indicates presence of aberration in the beam. Aberrations in the illumination beam due to imperfect optics and other components in the beam path are constant in nature and the same set of aberrations applies to all the positions of the illumination beam as it scans the sample plane. One can easily estimate such aberrations by placing a wavefront sensor [86, 87] near the entrance pupil of the focusing lens, if aberrations introduced by the objective lens is ignored.

One of the major issues in the case of microscopy is to estimate the aberrations present in the illumination beam, as it is incident at a certain location in the sample plane, since it is not possible to get direct information about the shape of the focal spot in the sample plane. Also it is not possible to place a wavefront sensor in the focal volume for direct measurement of aberrations. However, there are indirect ways to measure the aberrations present in the illumination beam. One such concept relies on the fact that when a beam is focused by a lens, the focal spot has the highest peak intensity when the beam is aberration free, compared to the beam with aberrations. Fig. 6.1 shows the arrangement for the measurement and compensation of the phase aberrations in the wavefront incident on the entrance pupil of a lens. The lens focuses the wavefront on a point photodetector placed on the focal plane of the lens. The phase of the incident wavefront at the entrance pupil of the lens is described by the function $\Phi_1(r,\theta)$, where r and θ are the polar coordinates of the entrance pupil. To compensate for the phase aberrations of the wavefront, an adaptive element (to be played by the LCSLM assembly in the present work) is placed in the entrance pupil of the lens which subtracts the phase aberrations present in the beam.

Let $\Phi_2(r,\theta)$ is the phase function to be subtracted by the adaptive element from the input wavefront. According to the Fourier diffraction theory the signal measured by the point photodetector is given by [6]

$$I = I_0 \left|\frac{1}{\pi}\int_0^{2\pi}\int_0^1 \exp\left\{i\big(\Phi_1(r,\theta)-\Phi_2(r,\theta)\big)\right\} r\,dr\,d\theta\right|^2 \tag{6.1}$$

where I_0 is proportional to the incident light power. It is assumed that the two

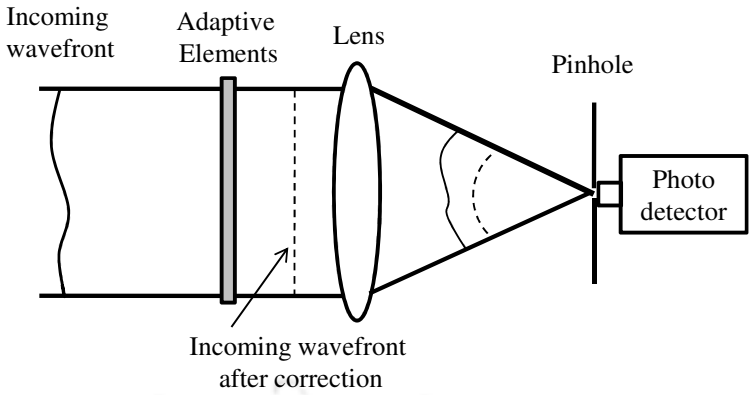

Figure 6.1: Schematic diagram of the adaptive optics system without a wavefront sensor. The incoming wave front is indicated by solid lines while the wavefront after correction using the adaptive elements is indicated by the dotted lines.

phase functions can be expressed in terms of a series of N Zernike polynomials [8, 53] and each Zernike polynomial is expressed as $Z_n(r,\theta)$ such that

$$\Phi_1(r,\theta) = \sum_{1}^{n} a_n Z_n(r,\theta) \tag{6.2}$$

$$\Phi_2(r,\theta) = \sum_{1}^{n} b_n Z_n(r,\theta) \tag{6.3}$$

Thus the phase of the input wavefront $\Phi_1(r,\theta)$ can be expressed in terms of N elements denoted by the vector $\mathbf{a}$. The elements of the vector $\mathbf{a}$ are the coefficients of the Zernike mode a_n. Similarly the correction phase is also expressed by the N elements denoted vector $\mathbf{b}$ comprising the coefficients b_n of the N Zernike polynomials. The signal at the photodetector can be written as

$$I(c) = I_0 f(c) \tag{6.4}$$

where $\mathbf{c}= \mathbf{a}-\mathbf{b}$, and $f(c)$ is a function of c expressed as

$$f(c) = |\frac{1}{\pi}\int_0^{2\pi}\int_0^1 e^{i\left(\sum_1^n c_n Z_n(r,\theta)\right)} r dr d\theta|^2 \tag{6.5}$$

where c_n is the coefficient of the nth Zernike mode corresponding to the corrected wavefront. Owing to the orthogonality of the Zernike modes, and for small $|c|$, $f(c)$ can be expressed as

$$f(c) \approx 1 - |c|^2 \tag{6.6}$$

Where $|c|^2$ represents the variance in the corrected wavefront. From the equation it is seen that $f(c)$ is isotropic and as c increases in magnitude $f(c)$ becomes smaller [88]. Its maximum occurs at $|c| = 0$ and is larger compared to the surrounding local maxima. When $|c| = 0$, the aberration in the input wavefront is well corrected by the adaptive element. In our optical sectioning microscope setup it is not possible to get $f(c)$ directly, however, we may get the value of $f'(c)$ which is the net signal in the detector area corresponding to a given location of the illumination beam on the sample plane. Since $f'(c)$ is due to primarily the light reflected from a small region around the centre of the illumination beam in the sample plane, it can be approximated to be proportional to $f(c)$. In this chapter we use the property of $f'(c)$ to estimate the coefficients of certain Zernike modes present in the input wavefront to get an aberration corrected wavefront. However the equation 6.6 is not going to be valid for very large c.

6.3 Estimation of aberrations in the illumination beam

In order to find the amount of aberrations, introduced into the illumination beam for each location of the beam on the sample plane, we considered the input aberrations in terms of a chosen number of Zernike modes. For each position of the beam, central intensities in the focal spot on the camera plane are recorded for all possible combination of co-efficients corresponding to the given Zernike modes [89]. The range over which each co-efficient is varied depends upon the expected magnitude of aberrations in the illumination beam. Thus for each beam position the LABVIEW program generates a series of binary holograms that will introduce aberrations into the illumination beam taking all possible combination of Zernike modes within the given range. The central intensity for each combination is stored in the PC. This data is then accessed by the same program and the combination of Zernike modes giving the maximum central intensity at each location is found. Thus a combination of Zernike co-efficients giving maximum $f'(c)$ is obtained which is then utilized to compute an appropriate hologram for each location of the beam. With this modified set of holograms an illumination beam is realised that is corrected for aberrations for each location of the sample plane. However this procedure cannot be applied for some regions of the sample plane where the transmittance or reflectivity is very poor.

Since in such regions even if the hologram is modified the intensity is not going to change significantly. In these cases a hologram comprising the default combination of Zernike modes is employed.

As mentioned previously the binary hologram based mechanism allows to move the beam simultaneously correcting it from aberrations. Fig. 6.2 (a) shows the experimentally obtained +1 order focal spot intensity which is close to an Airy disk for a given set of m_x and m_y of the hologram. The beam is then moved horizontally on the plane by changing m_x value of the hologram and at the same time a phase profile equal to 2 rms of primary y coma is incorporated to the hologram. As a result the beam gets aberrated and the shifted spot is shown in Fig. 6.2 (b). This demonstrates the capability of our LCSLM based system to deflect a beam, simultaneously performing an aberration correction operation.

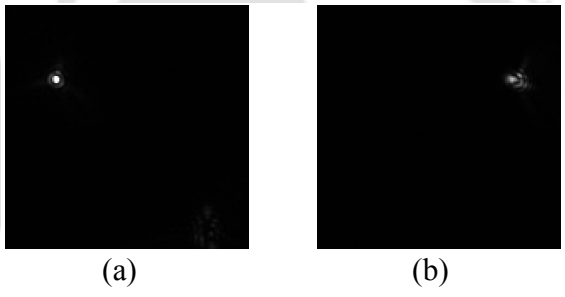

Figure 6.2: (a) Aberration corrected PSF of the illumination beam for a given value of m_x and m_y, and (b) aberrated PSF of the illumination beam and shifted horizontally in the camera plane.

6.4 The experimental arrangement

The experimental arrangement used, as shown in Fig. 6.3, is very similar to the setup described in chapter 4. The beam from a DPSS laser ($\lambda = 532$nm) is expanded and collimated using the beam expander BX which is then incident on the LCSLM plane. Binary holograms computed by a LABVIEW program in the PC are written onto the LCSLM. The diffracted beams from the LCSLM are focused by the lens L_1 and an iris diaphragm ID is kept in the focal plane to isolate the +1 order from the rest. The +1 order is then recollimated by the lens L_2 and is focused on the sample plane using the microscope objective MO. Light scattered or reflected by the sample is again reflected by the beam splitter BS and is focused onto the CCD using the lens L_3. A sequence of binary hologram, described over 800×800 pixels, is displayed on

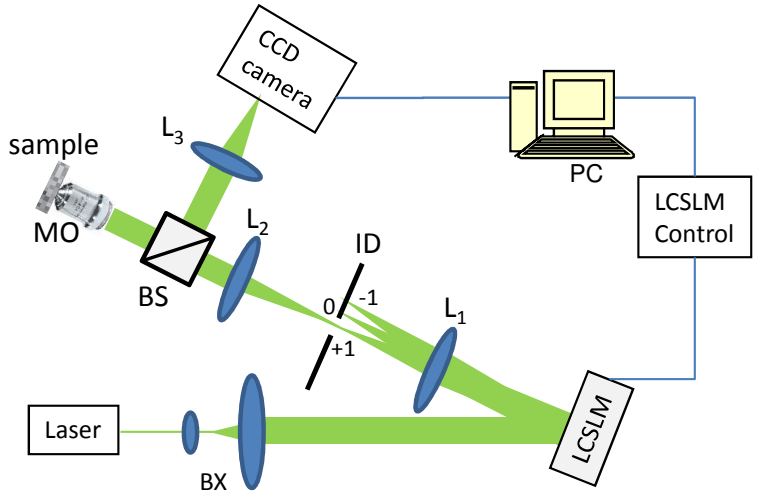

Figure 6.3: The experimental set up of the microscope with pixel to pixel variation in the illumination beam phase profile.

the LCSLM panel such that the illumination beam on the sample plane as well as its image on the camera plane describes rectangular areas. For detecting the signal for each position of the beam on the sample a small square area (detector area) enclosing the image of the beam on the camera is generated using the program. The detector area is synchronized to move with the image of the beam on the camera plane as the beam is scanned. For each position of the beam, the program collects the total signal which is within the detector area. At the end of the scanning process, the collected signal is converted into a digital image as described in chapter 4.

6.5 Experimental results and discussion

We use an USAF test target as the sample. We first record an image, over 32×32 pixels of the sample, using the fixed default phase profile of the illumination beam and the same is shown in Fig. 6.4 (a). In order to introduce position dependent aberrations into the illumination beam we make use of the computer generated holography technique. Here we use the zernike mode Z_5 and call a random number (say $rn(x_P, y_P)$ varying between 0 and 2) for each beam position (x_P, y_P). We then aberrate the illumination beam holographically with an aberration profile $\phi(x, y) = rn(x_P, y_P)\, Z_5$. The same is repeated for all beam positions. Thus the illumination beam has a phase profile that may vary from pixel to pixel. We then record another image of the same sample with this modified illumination beam. The image taken

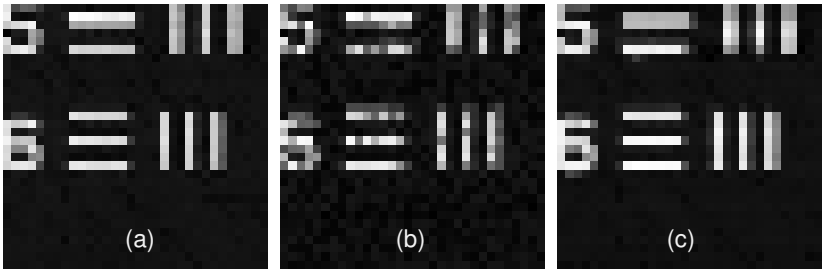

Figure 6.4: Recorded images of the USAF test target, (a) using the default constant phase profile of the illumination beam, (b) with an illumination beam having different aberration profiles for different locations, and (c) after incorporating position dependent corrections to the aberrated illumination beam.

with the spatially varying aberrations in the illumination beam is shown in Fig. 6.4 (b). Degradation in the image as compared to the image in Fig. 6.4 (a) is clearly noticed. We then employ the scheme described in section 6.2 to estimate the position dependent aberrations in terms of the co-efficient of Z_5. To correct the aberration in the illumination beam for each of the 32×32 discrete positions, the hologram is modified only for the Zernike mode Z_5 and coefficients are varied between the values 0 to -2 in 5 steps. At each position of the beam on the sample plane, the program records the central intensity for each strength of the Zernike mode. The program then looks at the recorded data and searches for the coefficient of the Zernike polynomial for which the illumination beam has the highest central intensity at each location. Using the set of Zernike coefficients, another set of hologram is computed. With this modified set of holograms, corrected illumination beam is generated and another image of the sample is recorded. The image recorded with this position dependent correction profile of the illumination beam is shown in Fig. 6.4 (c). Here, in comparison with the image in Fig. 6.4 (b), a significant improvement in the image quality is clearly observed.

6.6 Position dependent aberration correction with a variable intensity illumination beam

In chapter 5, we have discussed about the capability of our optical sectioning microscope to vary the intensity of the illumination beam so as to improve the SNR ratio in the low signal regions. Making use of the property of binary holograms, the position dependent aberration correction capability discussed in the previous

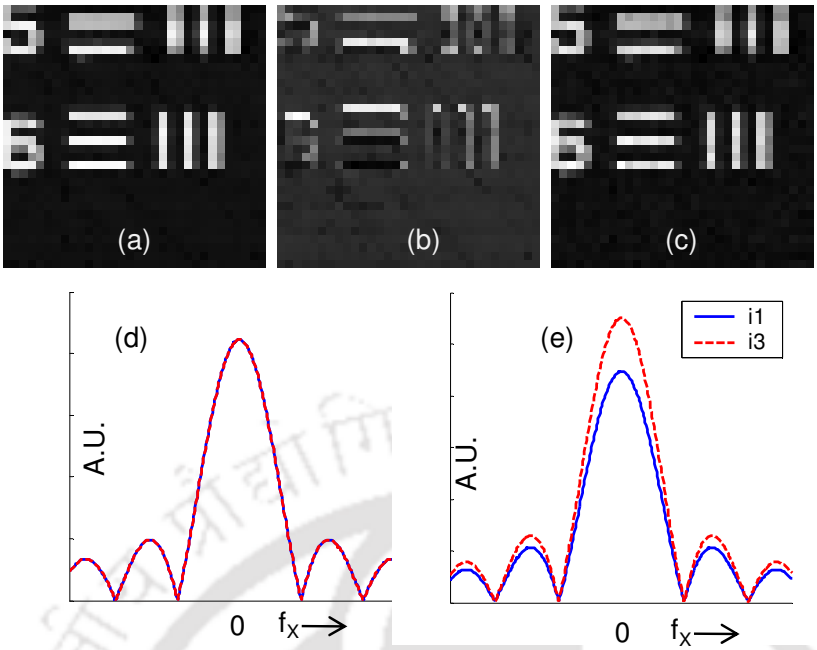

Figure 6.5: (a) The corrected image i_1, (b) the image i_2 recorder with the weighted intensity illumination beam, and (c) the final image i_3. Spatial frequency plots along X for the images i_1 and i_3 extracted from the normalised Fourier planes corresponding to the (d) high reflectivity region, and (e) low reflectivity region. The target in the chosen region does not have any spatial variation along X.

section, can be with a beam that also has position dependent illumination intensity.

In order to implement this, we consider the corrected image, shown in Fig. 6.4 (c), as the image i_1 and compute the weight function $w(x, y)$. To facilitate easy comparison, the image i_1 is shown again in Fig. 6.5 (a). Here we have taken w_M and w_m as 1 and 0, respectively. The weight function is then used to compute another set of binary holograms by incorporating the position dependent aberration correction and weighted illumination beam intensity, simultaneously. The corresponding recorded image i_2 is shown in Fig. 6.5 (b). We then digitally combine i_1 and i_2 to get the final image i_3, which is shown in Fig. 6.5 (c).

In order to demonstrate the relative improvement in signal level in low reflectivity regions of the target, we consider first the high reflective regions of the images i_1 and i_3. We then generate the normalized spatial frequency spectrum and the same along the Y axis is shown in Fig. 6.5 (d). It is observed that in the regions with high reflectivity the signal levels in i_1 and i_3 are comparable. We then employ the same procedure for the regions with low reflectivity and the spatial frequency spectrum along X which is shown in Fig. 6.5 (e). The increase in the strength corresponding to

the zero spatial frequency indicate the enhancement of signal levels in the image i_3 in the regions with low reflectivity. It is to be noted that spatial frequency spectrum is computed for a region in which the original target does not have any spatial variation along X.

6.7 Conclusion

A scanning optical microscope is described that has a binary hologram based beam scanning mechanism implemented with an LCSLM. The proposed microscope has dynamic control over the phase profile of the illumination beam at each position of the sample. This facilitates position dependent aberration correction of the illumination beam, while imaging samples introducing spatially varying aberration to the illumination beam. As a proof of principle experiment we holographically introduce position dependent aberrations into the illumination beam. Our results show that there is an enhancement in the contrast of the image after incorporating spatially varying correction phase profiles into the illumination beam. Here only one Zernike mode has been incorporated into the illumination beam. The principle can be easily extended for more number of Zernike modes. We also demonstrated position dependent aberration correction and variable illumination intensity simultaneously employed to image the same target.

Chapter 7

Conclusion and future prospects

7.1 Conclusion

The laser scanning confocal microscope (LSCM) is a very important imaging tool for providing optically sectioned images of a given sample. One crucial advantage of this microscope over several other high resolution microscopes is its non-invasive nature of imaging. This advantage becomes particularly useful in imaging biological specimens. Owing to its unique capabilities, the LSCM has become essential in diverse areas of research.

There have been continuous efforts to develop newer versions of the microscope in order to come up with improved imaging performance. Nevertheless commercially available LSCMs still suffer from a number of limitations.

One such limitation is the use of the galvo scanner mirror unit to scan the illumination beam. Galvo scanners have limited beam repeatability and suffer from long term thermal drift. Moreover there is a need to use a 4f relay system in between the two scanner mirrors, in order to ensure superior imaging performance. However, aligning such a relay system is a tedious task. Moreover, the extra optics adds more sources of aberrations into the illumination beam. Another issue with the LSCM is the illumination beam intensity that remains constant through out an image frame. If the sample to be imaged has regions of both high and low reflectivity/transmissivity/emissivity in the case of an LSCM working in the reflection/transmission/fluorescence mode, respectively, the resulting image will not have uniform signal to noise ratio (SNR) over the entire image plane. The third important issue in an LSCM is the phase profile of the illumination beam that remains

static over an entire image frame. It may be possible to correct the illumination beam for static aberrations, however, it cannot correct the illumination beam if it is aberrated with different amount of aberrations on a pixel to pixel basis. Such situations may arise especially when imaging inside a liquid or semi-liquid volume.

There are also other issues associated with the LSCM; however, in this thesis we addressed the above mentioned three issues only. Here we develop an optical sectioning microscope that works based on the principle of the confocal microscope. We use a liquid crystal spatial light modulator (LCSLM) assembly to implement dynamic binary diffraction holograms. We then realised a laser beam scanner based on the properties of binary holograms. In our proposed microscope, we replaced the galvo scanner with this binary hologram based beam scanner. We also exploit the properties of binary diffraction holograms to realise pixel to pixel variation in the illumination beam intensity and in the illumination beam phase profile. We performed experiments using our proposed optical sectioning microscope and the results obtained demonstrate the working of the microscope where the above mentioned three issues are addressed. Below we provide chapter-wise conclusion of this thesis work.

In chapter 1, we discussed about two basic types of optical microscopes, namely, the widefield and the point scanning microscopes. We focused our discussion on an important point scanning microscope called confocal microscope and discussed its working principles, various parameters and image formation theory. We then described the essential components of a confocal system. This is followed by a discussion on the issues with a laser scanning confocal microscope which are not yet adequately addressed. The chapter ended with the objective of the thesis.

In chapter 2, we described the principle of holography with an emphasis on reconstruction of the object beam wavefront using the principle of holography. The processes involved in the creation of digital hologram without having the real object beam were also discussed. We then introduced the generation of user defined wavefront using a computer generated holography technique. The chapter then discussed the properties of the liquid crystal cells and LCSLMs. This was followed by a discussion on the implementation of the computer generated holograms using an LCSLM. We also discussed the issue of aliasing and the way to remove it, that becomes relevant in the adopted computer generated holography technique.

In chapter 3 we investigated laser beam scanning with a binary amplitude hologram implemented using an LCSLM. We developed a mathematical expression to

theoretically predict the deflection angle of the +1 order diffracted beam corresponding to a given binary hologram written on the LCSLM. It was demonstrated that the experimentally found beam locations agreed well with the theoretically predicted beam locations. The theoretical expression can be used to create a map between the applied slope values and the corresponding beam locations, to realise equal step beam scanning along horizontal, vertical and diagonal directions. The experimental results demonstrated the utility of the map. We also performed experiments to demonstrate superior beam repeatability by the binary hologram based beam scanning mechanism.

In chapter 4, we implemented an optical sectioning microscope that uses a binary hologram based beam scanning mechanism. The binary hologram was first implemented on the display panel of a nematic LCSLM and later on the display panel of a ferroelectric LCSLM. The beam scanning mechanism implemented here does not require any scanner involving mechanical movement. It also removes the requirement of a 4f relay system that needs to be placed between the two scan mirrors, in the case of a galvo mirror scanner. The scanning mechanism can provide superior beam positioning compared to the conventional scanner. Moreover since the beam scanning is based on binary hologram written on a LC cell, the scanning provides better beam repeatability.

In the same chapter, we described detail experimental arrangement for the two versions of the microscope and presented preliminary experimental results. The experimental results clearly demonstrate the optical sectioning capability of the two proposed systems. The microscope implemented works in the reflection mode, however, the same can be reconfigured to work in the transmission or the fluorescence mode.

In chapter 5, we implemented a scanning optical sectioning microscope that has dynamic illumination beam intensity. Both the scanning and the programmable control over the illumination beam intensity were achieved using binary holograms written on an LCSLM. The microscope described here works in the transmission mode however the same can also work in the reflection or fluorescence mode. Unlike the conventional scanning microscope, the proposed microscope can have relatively high illumination beam intensity in the regions of the sample plane with weak reflectivity or transmissivity. The proposed system can thus increase the overall SNR especially in the region from where less signal is received. Both numerical simulation and experimental results showed enhancement of the signal to noise ratio in the

weakly transmissive regions.

In chapter 6, we described a scanning optical microscope that has dynamic control over the phase profile of the illumination beam at each position of the sample. This facilitates position dependent aberration correction of the illumination beam, while imaging samples introducing spatially varying aberration to the illumination beam. As a proof of principle experiment, we holographically aberrated the illumination beam with position dependent phase profiles. We then estimated the aberrations corresponding to each beam location and employed position dependent correction profiles into the illumination beam. Our results showed that there was an enhancement in the contrast of the image after incorporating spatially varying correction phase profiles into the illumination beam. We also demonstrated position dependent aberration correction and variable illumination intensity simultaneously employed to image the same target.

7.2 Future prospects

An important limitation of our proposed optical sectioning microscope is the imaging speed or frame rate. We were able to make the frame rate faster by utilising 24 bit display capability of FLCSLM.

However various relevant factors of the system, such as, camera trigger, integration of RGB images into the video signal, etc., are yet to be optimized to achieve the maximum possible frame rate. In order to exploit maximum possible refresh rate of the FLCSLM, a sequence of holograms need to be displayed on the panel without any break. This will require enhanced frame rate of the camera so that each camera frame can record the array of 24 focal spots corresponding to one color image. Thus the camera needs to be triggered at the same rate as the refresh rate of the panel.

We have used only one Zernike mode aberration to demonstrate the capability of the system to detect and correct aberrations on a pixel to pixel basis. Incorporating more number of Zernike modes is a routine; however, the search of the optimised aberration co-efficients will take a major share of time. There is a possibility to reduce the search time by making use of multiplex binary holograms. Multiplex binary hologram will facilitate generation of multiple illumination beams from each binary hologram in such a way that each illumination beam carries a certain amount of user defined aberration. However the multiplex hologram needs to be optimized to reduce the presence of unwanted diffraction orders in the vicinity of the illumination

beam.

So far we have implemented pixel to pixel variation in the phase profile of the illumination beam. It is worth extending the system to realize pixel to pixel variation in the polarization of the illumination spot. For this the display panel needs to be divided into two parts so that one part generates the x-polarized illumination beam while the other part generates the y-polarized illumination beam. The tilts associated with the two holograms can be manipulated to overlap the two beams so that the effective pupil plane is arbitrarily polarized. Imaging system with such a arrangement can be useful to study the orientation or re-orientation of the excited molecules when the microscope works in the fluorescence mode.

So far we have mentioned that the proposed microscope will work in the reflection/transmission or fluorescence mode. However there exists possibility to modify the system to implement other type of microscope such as multiphoton microscope second harmonic generation microscope and super resolution microscope provided the image frame rate achievable with the the spatial light modulator device is sufficient enough for the applications.

References

[1] Douglas B Murphy and Michael W Davidson. *Fundamentals of light microscopy and electronic imaging*. John Wiley & Sons, 2012. 28

[2] James B Pawley. *Handbook of biological confocal microscopy*. Springer, 1995. 30, 32, 42, 43, 44

[3] Tony Wilson. Confocal microscopy. *Academic Press: London, etc*, 426:1–64, 1990. 30, 31, 32, 37

[4] GJ Brakenhoff. Imaging modes in confocal scanning light microscopy (cslm). *Journal of microscopy*, 117(2):233–242, 1979. 32

[5] CJR Sheppard and T Wilson. Multiple traversing of the object in the scanning microscope. *Journal of Modern Optics*, 27(5):611–624, 1980. 34

[6] Tony Wilson and Colin Sheppard. Theory and practice of scanning optical microscopy. *London: Academic Press,— c1984*, 1, 1984. 35, 36, 91, 110

[7] Joseph W Goodman. *Introduction to Fourier optics*. Roberts and Company Publishers, 2005. 35, 52, 59

[8] Max Born et al. E. wolf principles of optics. *Pergamon Press*, 6:188, 1980. 36, 111

[9] Gordon S Kino and Timothy R Corle. *Confocal scanning optical microscopy and related imaging systems*. Access Online via Elsevier, 1996. 37, 39, 43, 101

[10] CJR Sheppard and T Wilson. Depth of field in the scanning microscope. *Optics Letters*, 3(3):115–117, 1978. 37, 38

[11] Ruikang K Wang and Valery V Tuchin. *Advanced Biophotonics: Tissue Optical Sectioning*. CRC Press, 2013. 37

[12] Michael Bass. *Handbook of optics. Vol. 2, Devices, measurements, and properties*. McGraw-Hill, 1995. 37

[13] S Hell, S Witting, M von Schickfus, RW Resandt, S Hunklinger, E Smolka, and M Neiger. A confocal beam scanning white-light microscope. *Journal of Microscopy*, 163(2):179–187, 1991. 40

[14] Hans J Tiziani and H-M Uhde. Three-dimensional image sensing by chromatic confocal microscopy. *Applied Optics*, 33(10):1838–1843, 1994. 40

[15] CJR Sheppard and T Wilson. Effect of spherical aberration on the imaging properties of scanning optical microscopes. *Applied optics*, 18(7):1058–1063, 1979. 40

[16] Johan S Ploem. Laser scanning fluorescence microscopy. *Applied optics*, 26(16): 3226–3231, 1987. 41

[17] Tetsurou Takamatsu and Setsuya Fujita. Microscopic tomography by laser scanning microscopy and its three-dimensional reconstruction. *Journal of microscopy*, 149(3):167–174, 1988. 41

[18] Seth R Goldstein, Thomas Hubin, Scott Rosenthal, and Clayton Washburn. A confocal video-rate laser-beam scanning reflected-light microscope with no moving parts. *Journal of microscopy*, 157(1):29–38, 1990. 41

[19] Ki Hean Kim, Christof Buehler, and Peter TC So. High-speed, two-photon scanning microscope. *Applied optics*, 38(28):6004–6009, 1999. 41

[20] A Draaijer and PM Houpt. High scan-rate confocal laser scanning microscopy, 1993. 41

[21] A Draaijer and PM Houpt. A standard video-rate confocal laser-scanning reflection and fluorescence microscope. *Scanning*, 10(4):139–145, 1988. 41

[22] Tony Wilson and AR Carlini. Size of the detector in confocal imaging systems. *Optics letters*, 12(4):227–229, 1987. 42

[23] William B Amos. Achromatic scanning system, March 5 1991. US Patent 4,997,242. 43

[24] Matthias Seel. Beam deflection device, August 13 2002. US Patent 6,433,908. 43

[25] Rosa Brouri, Alexios Beveratos, Jean-Philippe Poizat, and Philippe Grangier. Photon antibunching in the fluorescence of individual color centers in diamond. *Optics Letters*, 25(17):1294–1296, 2000. 43

[26] Flavie Sarrazin, Jean-Baptiste Salmon, David Talaga, and Laurent Servant. Chemical reaction imaging within microfluidic devices using confocal raman spectroscopy: the case of water and deuterium oxide as a model system. *Analytical chemistry*, 80(5):1689–1695, 2008. 43

[27] Mridula Vishwanath, Akiko Nishibu, Sem Saeland, Brant R Ward, Norikatsu Mizumoto, Hidde L Ploegh, Marianne Boes, and Akira Takashima. Development of intravital intermittent confocal imaging system for studying langerhans cell turnover. *Journal of investigative dermatology*, 126(11):2452–2457, 2006. 43

[28] Bruno G De Geest, Niek N Sanders, Gleb B Sukhorukov, Joseph Demeester, and Stefaan C De Smedt. Release mechanisms for polyelectrolyte capsules. *Chemical Society Reviews*, 36(4):636–649, 2007. 43

[29] Robert H Webb and Fran Rogomentich. Confocal microscope with large field and working distance. *Applied optics*, 38(22):4870–4875, 1999. 43

[30] Steffen Lindek, Rainer Pick, and Ernst HK Stelzer. Confocal theta microscope with three objective lenses. *Review of scientific instruments*, 65(11):3367–3372, 1994. 43

[31] DongKyun Kang, JungWoo Seo, and DaeGab Gweon. Improvement of detected intensity in confocal microscopy by using reflecting optical system. *Review of scientific instruments*, 75(2):550–552, 2004. 44

[32] W Tvarusko, M Bentele, T Misteli, R Rudolf, C Kaether, DL Spector, HH Gerdes, and R Eils. Time-resolved analysis and visualization of dynamic processes in living cells. *Proceedings of the National Academy of Sciences*, 96 (14):7950–7955, 1999. 44, 101

[33] Tom D Milster and Edwin P Walker. Mechanism for improving the signal-to-noise ratio in scanning optical microscopes. *Optics letters*, 21(16):1304–1306, 1996. 44

[34] Colin JR Sheppard, Wei Gong, and Ke Si. Polarization effects in 4pi microscopy. *Micron*, 42(4):353–359, 2011. 44

[35] Stefan W Hell, S Lindek, Christoph Cremer, and Ernst HK Stelzer. Measurement of the 4pi-confocal point spread function proves 75 nm axial resolution. *Applied Physics Letters*, 64(11):1335–1337, 1994. 44

[36] PE Hanninen, SW Hell, J Salo, E Soini, and C Cremer. Two-photon excitation 4pi confocal microscope: Enhanced axial resolution microscope for biological research. *Applied physics letters*, 66(13):1698–1700, 1995. 44

[37] Martin J Booth. Adaptive optics in microscopy. *Philosophical Transactions of the Royal Society A: Mathematical, Physical and Engineering Sciences*, 365 (1861):2829–2843, 2007. 45

[38] Martin J Booth, MAA Neil, and T Wilson. Aberration correction for confocal imaging in refractive-index-mismatched media. *Journal of microscopy*, 192(2): 90–98, 1998. 45

[39] Colin JR Sheppard and Min Gu. Aberration compensation in confocal microscopy. *Applied optics*, 30(25):3563–3568, 1991. 45

[40] P Török, SJ Hewlett, and P Varga. The role of specimen-induced spherical aberration in confocal microscopy. *Journal of microscopy*, 188(2):158–172, 1997. 45

[41] Y Ruan, P Bon, E Mudry, G Maire, PC Chaumet, H Giovannini, K Belkebir, A Talneau, B Wattellier, S Monneret, et al. Tomographic diffractive microscopy with a wavefront sensor. *Optics Letters*, 37(10):1631–1633, 2012. 45

[42] Tobias Haist, Jan Hafner, Michael Warber, and Wolfgang Osten. Scene-based wavefront correction with spatial light modulators. In *Optical Engineering+ Applications*, pages 70640M–70640M. International Society for Optics and Photonics, 2008. 45

[43] Markus Rueckel, Julia A Mack-Bucher, and Winfried Denk. Adaptive wavefront correction in two-photon microscopy using coherence-gated wavefront sensing. *Proceedings of the National Academy of Sciences*, 103(46):17137–17142, 2006. 45

[44] Simon Tuohy and Adrian Gh Podoleanu. Depth-resolved wavefront aberrations using a coherence-gated shack-hartmann wavefront sensor. *Optics Express*, 18 (4):3458–3476, 2010. 45

[45] H Song, R Fraanje, G Schitter, H Kroese, G Vdovin, and M Verhaegen. Model-based aberration correction in a closed-loop wavefront-sensor-less adaptive optics system. *Opt. Express*, 18(23):24070–24084, 2010. 45

[46] MAA Neil, MJ Booth, and T Wilson. Dynamic wave-front generation for the characterization and testing of optical systems. *Optics letters*, 23(23):1849–1851, 1998. 45

[47] BR Boruah. Dynamic manipulation of a laser beam using a liquid crystal spatial light modulator. *American Journal of Physics*, 77:331, 2009. 45

[48] Parameswaran Hariharan. *Basics of holography*. Cambridge University Press, 2002. 48

[49] Belkrishna B Laud. Lasers and nonlinear optics. 1986. 50

[50] Bryon R Brown and Adolf W Lohmann. Complex spatial filtering with binary masks. *Applied Optics*, 5(6):967–969, 1966. 50

[51] Adoph W Lohmann and DP Paris. Binary fraunhofer holograms generated by computer. *Applied Optics*, 6(10):1739–1748, 1967. 50

[52] BR Brown and AW Lohmann. Computer-generated binary holograms. *IBM Journal of research and Development*, 13(2):160–168, 1969. 50

[53] Virendra N Mahajan. Zernike circle polynomials and optical aberrations of systems with circular pupils. *Applied optics*, 33(34):8121–8121, 1994. 53, 91, 107, 111

[54] Steven W Smith. *Digital signal processing: a practical guide for engineers and scientists*. Newnes, 2003. 54

[55] Jinyang Liang, Rudolph N Kohn Jr, Michael F Becker, Daniel J Heinzen, et al. High-precision laser beam shaping using a binary-amplitude spatial light modulator. *Applied optics*, 49(8):1323–1330, 2010. 56

[56] AM Weiner. Femtosecond pulse shaping using spatial light modulators. *Review of scientific instruments*, 71(5):1929–1960, 2000. 56

[57] René L Eriksen, Paul C Mogensen, and Jesper Glückstad. Multiple-beam optical tweezers generated by the generalized phase-contrast method. *Optics letters*, 27(4):267–269, 2002. 56

[58] Jennifer E Curtis, Brian A Koss, and David G Grier. Dynamic holographic optical tweezers. *Optics Communications*, 207(1):169–175, 2002. 56

[59] Fumihito Arai, Keiichi Yoshikawa, Toshihiro Sakami, and Toshio Fukuda. Synchronized laser micromanipulation of multiple targets along each trajectory by single laser. *Applied Physics Letters*, 85(19):4301–4303, 2004. 56

[60] Pierre-Gilles de Gennes, Jacques Prost, and Robert Pelcovits. The physics of liquid crystals. *Physics Today*, 48:70, 1995. 56

[61] Eiji Kaneko. *Liquid crystal TV displays: principles and applications of liquid crystal displays*, volume 3. KTK Scientific Publishers, 1987. 57

[62] Lev Mikhaĭlovich Blinov. *Electro-optical and magneto-optical properties of liquid crystals*. Wiley New York, 1983. 57

[63] CW Smith, DG Gisser, M Young, and SR Powers Jr. Liquid-crystal optical activity for temperature sensing. *Applied Physics Letters*, 24:453, 1974. 57

[64] V Freedericksz and V Zolina. Forces causing the orientation of an anisotropic liquid. *Transactions of the Faraday Society*, 29(140):919–930, 1933. 57

[65] Uzi Efron. *Spatial Ligth Modulator Technology: Materials, Devices and Applications*, volume 47. CRC Press, 1995. 57, 94

[66] Robert B Meyer, L Liebert, L Strzelecki, and Patrick Keller. Ferroelectric liquid crystals. *Journal de Physique Lettres*, 36(3):69–71, 1975. 61

[67] Dhirendra Kumar, Abhijit Das, and Bosanta R Boruah. Note: A simple experimental arrangement to generate optical vortex beams. *Review of Scientific Instruments*, 84(2):026103, 2013. 64

[68] Bosanta R Boruah, Gordon D Love, and Mark AA Neil. Interferometry using binary holograms without high order diffraction effects. *Optics letters*, 36(12): 2357–2359, 2011. 68

[69] MG Kim, GH Jang, CJ Lee, and DO Lim. Experimental identification of abnormal noise and vibration in a high-speed polygon mirror scanner motor due to mechanical contact of plain journal bearing. *Microsystem technologies*, 16(1-2):3–8, 2010. 72

[70] James D Lechleiter, Da-Ting Lin, and Ilse Sieneart. Multi-photon laser scanning microscopy using an acoustic optical deflector. *Biophysical journal*, 83(4):2292–2299, 2002. 72

[71] Harry W Presley, Lee M Burberry, and Anthony F Abbenante. Acousto-optic deflector for free-space laser communications. In *Optical Engineering and Photonics in Aerospace Sensing*, pages 105–114. International Society for Optics and Photonics, 1993. 72

[72] Olof Bryngdahl and Wai-Hon Lee. Laser beam scanning using computer-generated holograms. *Applied Optics*, 15(1):183–194, 1976. 72

[73] David Engström, Jörgen Bengtsson, Emma Eriksson, and Mattias Goksör. Improved beam steering accuracy of a single beam with a 1d phase-only spatial light modulator. *Optics express*, 16(22):18275–18287, 2008. 73

[74] Christian HJ Schmitz, Joachim P Spatz, Jennifer E Curtis, et al. High-precision steering of multiple holographic optical traps. *Opt. Express*, 13(21):8678–8685, 2005. 73

[75] Lingjiang Kong, Ying Zhu, Yan Song, and Jianyu Yang. Beam steering approach for high-precision spatial light modulators. *Chinese Optics Letters*, 8 (11):1085–1089, 2010. 73

[76] Abhijit Das and Bosanta R Boruah. Beam deflection by an aperiodic binary diffraction grating. *Journal of Optics*, 15(2):025709, 2013. 76

[77] Xu Wang, Daniel Wilson, Richard Muller, Paul Maker, and Demetri Psaltis. Liquid-crystal blazed-grating beam deflector. *Applied Optics*, 39(35):6545–6555, 2000. 86

[78] Abhijit Das and BR Boruah. Optical sectioning microscope with a binary hologram based beam scanning. *Review of Scientific Instruments*, 82(4):043702, 2011. 87

[79] Claus B Müller and Jörg Enderlein. Image scanning microscopy. *Physical review letters*, 104(19):198101, 2010. 89

[80] Emilio Sánchez-Ortiga, Colin JR Sheppard, Genaro Saavedra, Manuel Martínez-Corral, Ana Doblas, and Arnau Calatayud. Subtractive imaging in confocal scanning microscopy using a ccd camera as a detector. *Optics letters*, 37(7):1280–1282, 2012. 89

[81] Bosanta R Boruah and Mark A Neil. Susceptibility to and correction of azimuthal aberrations in singular light beams. *Optics express*, 14(22):10377–10385, 2006. 91

[82] Abhijit Das and Bosanta R Boruah. Note: Laser beam scanning using a ferroelectric liquid crystal spatial light modulator. *Review of Scientific Instruments*, 85(4):046103, 2014. 96

[83] Cathie Ventalon and Jerome Mertz. Dynamic speckle illumination microscopy with translated versus randomized speckle patterns. *Optics express*, 14(16): 7198–7209, 2006. 102

[84] Abhijit Das and BR Boruah. Point scanning microscope with adaptive illumination beam intensity. In *OPTICS: PHENOMENA, MATERIALS, DEVICES, AND CHARACTERIZATION: OPTICS 2011: International Conference on Light*, volume 1391, pages 324–326. AIP Publishing, 2011. 103

[85] Triet Le, Rick Chartrand, and Thomas J Asaki. A variational approach to reconstructing images corrupted by poisson noise. *Journal of Mathematical Imaging and Vision*, 27(3):257–263, 2007. 104

[86] Roland V Shack and BC Platt. Production and use of a lenticular hartmann screen. In *Journal of the Optical Society of America*, volume 61, page 656.

AMER INST PHYSICS CIRCULATION FULFILLMENT DIV, 500 SUNNYSIDE BLVD, WOODBURY, NY 11797-2999, 1971. 110

[87] BR Boruah. Zonal wavefront sensing using an array of gratings. *Optics letters*, 35(2):202–204, 2010. 110

[88] Martin Booth. Wave front sensor-less adaptive optics: a model-based approach using sphere packings. *Optics Express*, 14(4):1339–1352, 2006. 112

[89] Abhijit Das and Bosanta R Boruah. Dynamic control of illumination beam phase profile in a scanning optical microscope. In *European Conferences on Biomedical Optics*, pages 87970K–87970K. International Society for Optics and Photonics, 2013. 112

Publications

(a) Journals and Proceedings

1. **Abhijit Das**, and Bosanta R. Boruah, "Note: Laser beam scanning using a ferroelectric liquid crystal spatial light modulator," Review of Scientific Instruments: 85 046103 (2014).

2. **Abhijit Das**, and Bosanta R. Boruah, "Dynamic control of illumination beam phase profile in a scanning optical microscope," Proceedings of SPIE : 8797 87970K, 2013.

3. **Abhijit Das** and B. R. Boruah, "Beam deflection by an aperiodic binary diffraction grating," Journal of Optics (IOP), 15(025709) (2013).

4. **Abhijit Das** and B. R. Boruah, "Point Scanning Microscope with Adaptive Illumination Beam Intensity," AIP Conf. Proc. 1391, 324-326, 2011.

5. **Abhijit Das** and B. R. Boruah, "Optical sectioning microscope with a binary hologram based beam scanning," Review of Scientific Instruments, 82 043702 (2011).

(b) Other relevant Publications (Not directly related to the thesis work)

1. Dhirendra Kumar, **Abhijit Das** and B. R. Boruah, "Note: A simple experimental arrangement to generate optical vortex beams," Review of Scientific Instruments: 84 026103 (2013).

2. B. R. Boruah and **Abhijit Das**, "A zonal wavefront sensor with reduced number of rows in the detector array," Applied Optics : 50(20) 3598-3603 (2011).

(c) Conference Presentation:

1. European conferences on Biomedical Optics, Munich, Germany, May 12-16, 2013, **Abhijit Das** and B. R. Boruah, "Dynamic Control of Illumination Beam Phase Profile in a Scanning Optical Microscope".

2. Focus on Microscopy, Singapore, April 1-4, 2012, **Abhijit Das** and B. R. Boruah, "Scanning optical microscope with programmable illumination beam intensity".

3. XXXVI OSI SYMPOSIUM on Frontiers in Optics and Photonics (FOP11), IIT Deihi, New Delhi, India, December 3-5, 2011, **Abhijit Das** and B. R. Boruah, "Binary Hologram based beam scanning with equal step beam size".

4. XXXVI OSI SYMPOSIUM on Frontiers in Optics and Photonics (FOP11), IIT Deihi, New Delhi, India, December 3-5, 2011, **Abhijit Das** and B. R. Boruah, "Scanning optical microscope with enhanced signal to noise ratio performance".

5. OPTICS11: NIT Calicut, Kerala, India, May 23-25, 2011, **Abhijit Das** and B. R. Boruah "Point Scanning Microscope with Adaptive Illumination Beam Intensity".

6. DAE-BRNS National Laser Symposium (NLS-19), RRCAT Indore, India, December 1-4, 2010, **Abhijit Das** and B. R. Boruah, "Laser Scanning Reflected Light Microscope using Holographic Scanning".

(d) School/Seminar/Workshop attended:

1. IEEE Workshop on Compressed sensing & Technical Writing, IIT Guwahati, 6-7 April 2013.

2. Computational Technique in Physics, IIT Guwahati, 1-6 Augast, 2011.

3. Introductory workshop on optical microscopy, IIT Guwahati, 16-17 June, 2011.

4. SERC Preparatory School on Modern Optics, IIT Guwahati, 10-23 November 10-23, 2010.

***